Contents

Introduction

One of the primary goals of observational cosmology is to trace star formation and nuclear activity along with the mass assembly history of galaxies as a function of redshift and environment. Theoretical arguments suggest that there is a fundamental link between the assembly of Black Holes and the formation of spheroids in galaxy halos. The tight relation observed in local galaxies between the black holes mass and the velocity dispersion (the M_{BH}-σ relation) and the fact that the locally inferred black hole mass density appears to be broadly consistent with the mass accreted during the quasar phase further support the idea that the nuclear activity, the growth of the black holes and spheroid formation are all closely linked. Thus, it is clear that a detailed investigation of the formation and evolution of Active Galactic Nuclei (AGN) over a wide range of redshifts, and the comparison with galaxy evolution, could provide information about the link between nuclear activity, star formation and the galaxy assembly that seem to co-exist in the early Universe. In this framework, the hard X–ray band is by far the cleanest one where to study the history of accretion in the Universe, being the only band in which accretion processes dominate the cosmic background.

The X–ray background

The cosmic X–ray background (XRB) was discovered at the dawn of the X–ray astronomy: during the first successful rocket flight launched to study the X–ray emission from the Moon, the presence of a residual diffuse emission was also "serendipitously" revealed (Giacconi et al. 1962). The lack of any correlation with the galactic latitude, and a dipole anisotropy consistent with that of the dipole component of the Cosmic Microwave Background (CMB; Shafer & Fabian 1983) strongly argued from the beginning in favour of a cosmological origin of this extragalactic background radiation.

The first broad–band measurements of the XRB spectrum was obtained at the end of the 70's with the HEAO–1 satellite. Marshall et al. (1980) showed that the HEAO–1 data were very well fitted by a 40 keV thin thermal bremsstrahlung model, approximated below 15 keV with a simple power–law spectral function ($F(E) \propto E^{-\Gamma}$) with photon index $\Gamma \sim 1.4$. It was therefore quite natural to hypothesize the presence of a truly diffuse hot Inter Galactic Medium (IGM) with a characteristic temperature of kT=40(1+z) keV, as

originally proposed by Field and Perrenod (1977).
However, a reasonable extrapolation of the X–ray properties and optical counts of extragalactic sources led to the conclusion that discrete sources could contribute significantly to the XRB (Schmidt & Green 1986). Moreover, Giacconi & Zamorani (1987) have subsequently shown that, once the contribution estimated from known AGN is removed, the residual background spectrum is too flat to be interpreted in terms of an optically thin bremsstrahlung from a diffuse IGM.
This hypothesis has been then entirely discarded with the results from the COBE satellite (Mather et al. 1990). A diffuse, hot ($T \gtrsim 10^8$ K) IGM should give rise to evident high-frequency distortions in the CMB spectrum through inverse-Compton scattering, which have not been observed by COBE; this implies that the contribution of hot gas to the XRB is lower than 0.01% (Wright et al. 1994).

As a consequence, the only viable alternative for the XRB origin remained the superposition of discrete sources, and the most likely candidates appeared immediately to be AGN.
The most serious problem with the discrete-source origin for the XRB remained the so-called "spectral paradox" (Boldt 1987): at that time there were already stringent evidences that the AGN X–ray continuum in the 2–10 keV band is well described by a power–law with index $\Gamma \simeq 1.7$–1.9 (Mushotzky et al. 1984; Turner & Pounds 1989), too soft to fit the value observed for the hard XRB in the same energy band ($\Gamma \sim 1.4$).
Setti & Woltjer (1989) showed that, on the basis of Unification Schemes of AGN, strong X–ray absorption is naturally predicted for the sources optically classified as narrow line, Type 2 objects*, and that the amount of obscuring matter along the line of sight, measured in equivalent neutral hydrogen column (N_H), can be even in excess than 10^{24} cm^{-2}. As a consequence, the resulting X–ray spectra will peak at high energies (from a few keV up to $\gtrsim 10$ keV, depending from the N_H) and the net result is a flatter power–law spectral index. The "spectral paradox" could be therefore theoretically solved by assuming that the XRB is due to the superposition of absorbed and unabsorbed objects, with the same intrinsic steep ($\Gamma \sim 1.8$) power–law continuum.
Following these indications, several authors have refined and developed population–synthesis models able to reproduce the XRB spectral shape and intensity (e.g. Madau, Ghisellini & Fabian 1994; Comastri et al. 1995,2001; Gilli, Salvati & Hasinger 2001), assuming a wide range of redshifts (i.e. evolution) and column densities† of the absorbing matter in the range

*In the zero–th order Unification Schemes, there is a correspondence between X–ray and optical absorption: Type 2 narrow–lined objects are X–ray obscured, and Type 1 broad–lined objects are not. The underlying continuum is intrinsically the same, and the differences in the optical and X–ray spectra are only due to orientation effects (e.g. Antonucci 1993).

†If the X–ray obscuring matter has a column density which is equal or larger than the inverse of the Thomson cross–section ($N_H \geq \sigma_T^{-1} \simeq 1.5 \times 10^{24}$ cm^{-2}) the source is called, by definition, "Compton Thick".

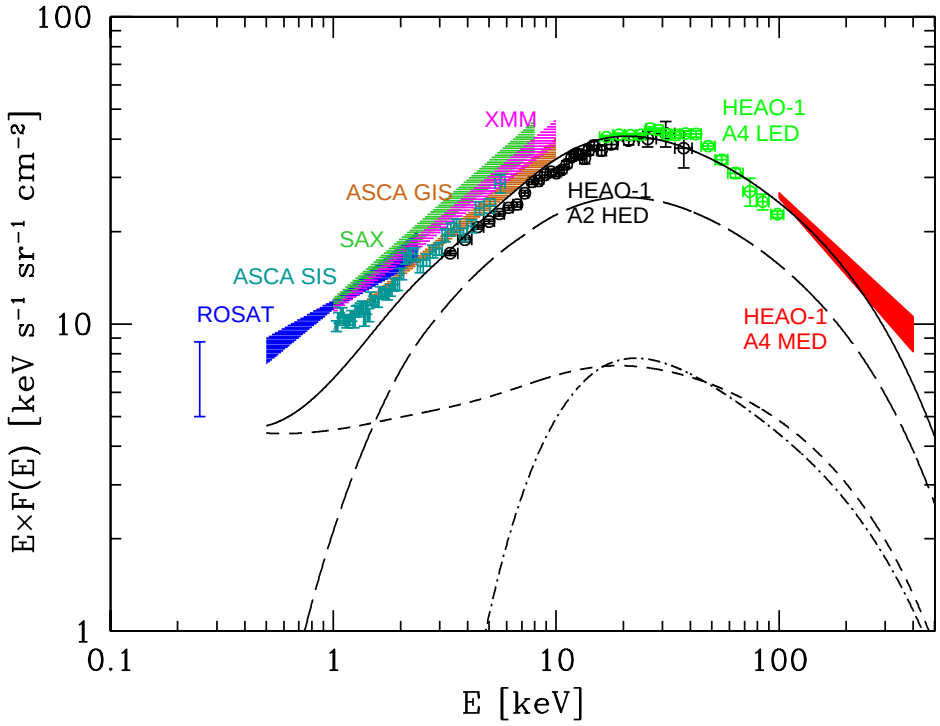

Figure 1.1 The AGN contribution (solid line) to the XRB spectral energy density as measured by different instruments (labeled). The contribution of unobscured ($N_H < 10^{21}$ cm^{-2}, dashed line), Compton thin ($N_H = 10^{21} - 10^{24}$ cm^{-2}, long–dashed line) and Compton thick (N_H) $> 10^{24}$ cm^{-2}, dot–dashed line) AGN is also shown. [From Comastri (2004)].

$N_H = 10^{21} - 10^{25}$ cm^{-2}. In Fig. 1.1 a compilation of XRB measurements in different energy bands is shown along with the best–fit model from Comastri et al. (2001). The contribution of unobscured (dashed line), mildly obscured ($N_H = 10^{21} - 10^{24}$ cm^{-2}, Compton Thin) and heavily obscured ($N_H > 10^{24}$ cm^{-2}, Compton Thick) sources is also reported.
The combined fit of other observational constraints in addition to the XRB spectral shape (in primis the number counts, and the redshift and absorption distributions in different energy ranges) is needed to build a self–consistent model and discriminate among the assumptions adopted for the cosmological evolution of the discrete sources. In particular, the key parameter turned out to be the evolution of obscured (Type 2) sources. As an example, the baseline AGN synthesis model adopt a simple Pure Luminosity Evolution (PLE) and is based on the zero–th order AGN Unification Schemes (Antonucci

1993); this implies that 1) the evolution of obscured AGN is *assumed* to follow that of unobscured AGN, and 2) the existence of a population of high–luminosity, highly obscured quasars (the so–called QSO2) is *naturally* postulated (Comastri et al. 1995). Indeed, it has been subsequently shown that QSO2 are *necessary* in reproducing the 2–10 keV source counts at relatively bright fluxes ($\simeq 10^{-13}$ erg cm^{-2} s^{-1}; Gilli et al. 2001; Comastri et al. 2001); however, despite intensive optical searches, these narrow–line high–redshift objects appear to be elusive, suggesting a space density and evolution different from that expected from unified schemes and calling for substantial revisions of the main assumptions of XRB baseline models.

Hard X–ray surveys and "new" observational constraints

A large number of multiwavelength projects have been specifically designed in the last years to investigate the evolutionary properties of AGN.
The results from hard X–ray surveys carried out at the end of the 90's with ASCA (e.g. the ASCA GIS survey, Cagnoni et al. 1998; the ASCA MSS and LSS Surveys, Ueda et al. 1999; Akiyama et al. 2002) and BeppoSAX (the *Beppo*SAX HELLAS survey, Fiore et al. 2001; Vignali 2001) constituted the first piece of evidence that AGN synthesis models do indeed work. However, the resolved fraction of the XRB was still too low ($\sim 25-30\%$) to quantitatively constrain all the models parameters; in particular, sampling the bright X–ray fluxes ($> 10^{-13}$ erg cm^{-2} s^{-1}) previous X–ray surveys were strongly biased towards luminous, high–redshift sources.
The superb capabilities of the detectors on-board the *Chandra* and XMM–*Newton* X–ray satellites have opened up new frontiers in testing these predictions down to limiting fluxes where the entire spectral energy density in the 2–10 keV band is expected to be resolved. Thanks to the deep X–ray surveys carried out in the *Chandra* Deep Field North (CDFN, Brandt et al. 2001a, Alexander et al. 2003), *Chandra* Deep Field South (CDFS, Giacconi et al. 2001) and the Lockman Hole (Hasinger et al. 2001) the X–ray sky is now probed down to a 2–10 keV flux limit of about 2×10^{-16} erg cm^{-2} s^{-1} and a fraction as large as 80-90% of the diffuse XRB is resolved into discrete sources (Mushotzky et al. 2000; Hasinger et al. 2001; Rosati et al. 2002; Alexander et al. 2003), the bigger uncertainty being the XRB normalization (Barcons, Mateos, & Ceballos 2000).
Moreover, hard X–ray surveys have proven to be very efficient to uncover obscured accreting black holes, confirming, at least qualitatively, the predictions of standard models, in which the 2-10 keV XRB is mostly made by the superposition of obscured and unobscured AGN. In particular, the recent findings are in very good agreement with the main predictions of XRB synthesis models for the source counts in different X–ray bands (see Moretti et al. 2003 for a comprehensive compilation of recent data); moreover, the observed average spectrum of the sources detected down to 10^{-16} erg cm^{-2} s^{-1} now exactly matches that of the XRB ($< \Gamma > \sim 1.4$, Tozzi et

al. 2001a,b).
Deep, pencil beam surveys, albeit extremely important, explore only a limited region of the luminosity–redshift plane, being strongly biased against the brightest (and rare) objects. Sizable samples of objects detected at the bright X–ray fluxes ($\gtrsim 10^{-14}$ erg cm^{-2} s^{-1}) over an area of the order of a few square degrees are needed to homogeneously cover the Hubble diagram and to obtain a well–constrained luminosity function with a similar number of sources per luminosity decade and per redshift bin. The detailed study of the nature of the hard X–ray source population, is indeed pursued complementing deep pencil beam observations with shallower, larger area surveys. In the last few years several projects with both *Chandra* and XMM–*Newton* have already started, with the aim of surveying from few to several tens degrees of the hard X–ray sky at different limiting fluxes (i.e. HELLAS2XMM – Baldi et al. 2002; Champ – Green et al. 2004; SEXSI – Harrison et al. 2003; XMM HBS – Caccianiga et al. 2004). The main goal of these projects is to collect a statistically significant number (~ 200) of X–ray, absorbed sources (including the "rare" QSO2) that will be used to derive the luminosity function of obscured objects that is nowadays basically unconstrained.

Redshift and absorption distributions

Although quite successful in reproducing the XRB spectral shape, intensity and X–ray number counts, AGN synthesis models, at least in their simplest version (where the evolution of the obscured population is assumed to be the same as that of unobscured quasars), do not reproduce other observational constraints, as the observed redshift and absorption distributions.
There are increasing evidences (Hasinger 2003; Barger et al. 2003) that the bulk of the XRB appears to be produced at relatively low redshift (z < 1) and dominated by relatively low luminosity Seyfert galaxies ($L_X = 10^{42} - 10^{44}$ erg s^{-1}) rather than mainly due to luminous quasars at higher redshift (z=1.5-2), as observed by previous shallower ROSAT and ASCA surveys and predicted by XRB synthesis models.
In the left panel of Fig. 1.2 (from Hasinger 2003) the predictions from the Gilli et al. (2001) model are compared with the redshift distribution of AGN selected from the CDFN and CDFS samples. At redshift below z=1.5, predicted and observed distributions differ drastically, definitively indicating that the evolution of obscured sources is not as simple as postulated.
Another important observational constraint that can be used to test the assumptions of the XRB models is the number of obscured (e.g. $N_H > 10^{22}$ cm^{-2}) sources as a function of the X–ray flux. While standard model predictions are able to *qualitatively* explain the hardening of the average spectrum of X–ray sources with decreasing flux, the rather steep hardening observed in both the CDFN and CDFS observations (Tozzi et al. 2001; Piconcelli et al. 2003) is a further indication that the evolution cannot be as simple as initially postulated. Moreover, preliminary results from X–ray spectral analysis on the fraction of obscured ($N_H > 10^{22}$ cm^{-2}) sources indicate that observations fall short by a factor of ~ 2 with respect to current

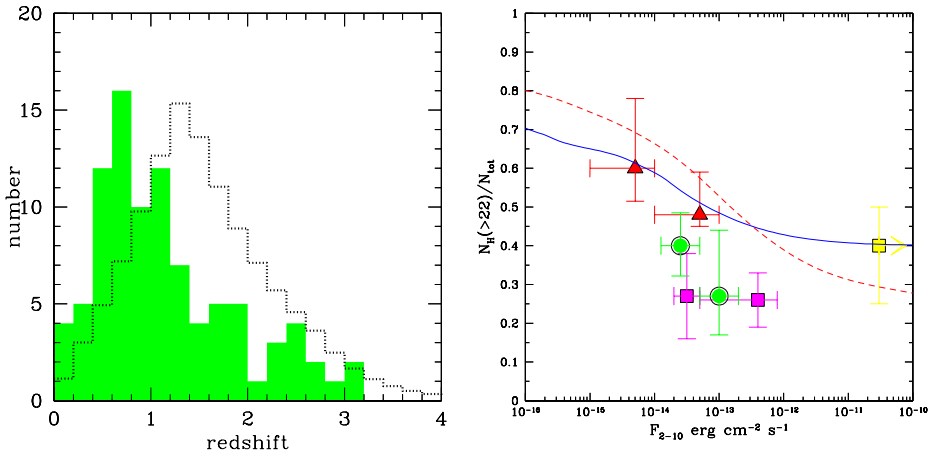

Figure 1.2 *Left*: Redshift distribution for a selected sample of 93 X–ray sources with $f_{2-10} > 5 \times 10^{-15}$ erg cm^{-2} s^{-1} in the central regions of the CDFS, CDFN, Lockman Hole, Lynx field, and SSA13 field (see Gilli 2003 for details). The data (shaded area) are compared with the predictions of Gilli et al. (2001) at the same limiting flux (dotted line). [From Hasinger (2003)].
Right: The expected fraction of objects with absorption column densities larger than 10^{22} cm^{-2} as a function of the 2–10 keV for the Comastri et al. 1995 model (solid line) and the Gilli et al. 2001 model (dashed line). The Comastri et al. 1995 model has been normalized to the observed fraction of absorbed sources in the HEAO1–A2 AGN sample of Piccinotti et al. 1982 (*filled square* at bright fluxes). The other points and associated error bars correspond to the the values found by Piconcelli et al. (2003, *filled squares*) and those obtained by Perola et al. (2004, *filled circles*), both derived from proper X–ray spectral analysis. The *filled triangles* at the faintest fluxes refer to the CDFN data (Brandt et al. 2001a; Barger et al. 2002) and have been derived from the observed hardness ratio assuming $\Gamma = 1.7$, and the redshift proper of the source if it is available, or $z = 1$ otherwise.

model predictions at relatively bright X–ray fluxes ($\gtrsim 10^{-14}$, Piconcelli et al. 2003; Perola et al. 2004), while a much better agreement between data and predictions seems to occur at fainter fluxes, using the hardness–ratio technique (Fig. 1.2, right panel). Finally, there are also evidences that the obscuration could be dependent from the source luminosity and redshift (Ueda et al. 2003).

All the findings discussed above constitute robust evidences for a luminosity dependence in the number density evolution of X–ray selected AGN, already pointed out by previous soft (ROSAT, Miyaji et al. 2000) and hard (*Beppo*SAX, La Franca et al. 2002) X–ray surveys. Cowie et al. (2003) and Hasinger (2003) calculated preliminary luminosity functions (LF) on the basis of the results from the deep surveys. The shape of the LFs in different redshift shells is significantly different so that the cosmological evolution can be described neither by pure luminosity nor pure density evolution. The

most surprising result is, however, that lower luminosity AGN show much less or even negative density evolution with respect to the strong positive evolution observed for relatively luminous QSO. The observed evolution for the low–luminosity population (a very rapid increase of volume emissivity at low redshift) can explain the sharp peak observed at z$\sim 0.7-0.8$ in the deep fields (Hasinger 2003).
Interestingly enough, the late evolution of the low–luminosity AGN is very similar to that required to explain the steep slope of the observed 15 micron number counts (Franceschini et al. 2001). Given the rather strong indications that the 15 micron emission is mainly due to dust enshrouded stellar activity (rather than AGN), a similar evolution of hard X–ray and MIR selected sources adds further strength to a close connection between the onset and fueling of AGN activity and star formation. On this basis, Franceschini et al. (2002) and Gandhi & Fabian (2003) elaborated XRB synthesis models able to reproduce the observed peak at z~ 0.7 in the redshift distribution, assuming that Type 1 AGN are distributed according to the well–determined soft X–ray luminosity function (Miyaji, Hasinger & Schmidt 2000), and that the evolution of Type 2 AGN follows the MIR one. However, as convincingly demonstrated by Gilli (2003), both these models are in disagreement with another observational constraint, the ratio of Type2/Type1 object as a function of redshift.

Although converging to the same bottom line (a luminosity-dependent cosmological evolution), the results on the space density and evolution suffer from substantial spectroscopic incompleteness and therefore have still to be taken with a grain of salt. Indeed, at the faintest fluxes explored by the CDFN and CDFS optical counterparts are sometimes so faint to prevent redshift measurements (even photometric) with the largest ground–based facilities; as a result, the spectroscopic completeness is only $\sim 50-60\%$ (Barger et al. 2003; Szokoly et al. 2004). This limitation mainly affects the study of the evolution of high–redshift objects.

The f_X/f_{opt} diagnostic

It is well known (Maccacaro et al. 1988) that various classes of X–ray emitters are characterized by different values of their X–ray–to–optical flux ratios (hereinafter X/O) and the observed X/O can yield important information on the nature of X–ray sources.
For a given X–ray energy range and R–band magnitude the following relation holds:

$$log\mathrm{X/O} = log\mathrm{f_X} + \mathrm{R}/2.5 + const \qquad (1.1)$$

where $\mathrm{f_X}$ is the X–ray flux, R is the optical magnitude and $const$ depends only on the R–band filter used in the optical observations[‡]. A value of

[‡]For the most popular R–band filters, $\Delta const <= 0.2$; an indicative, average value is

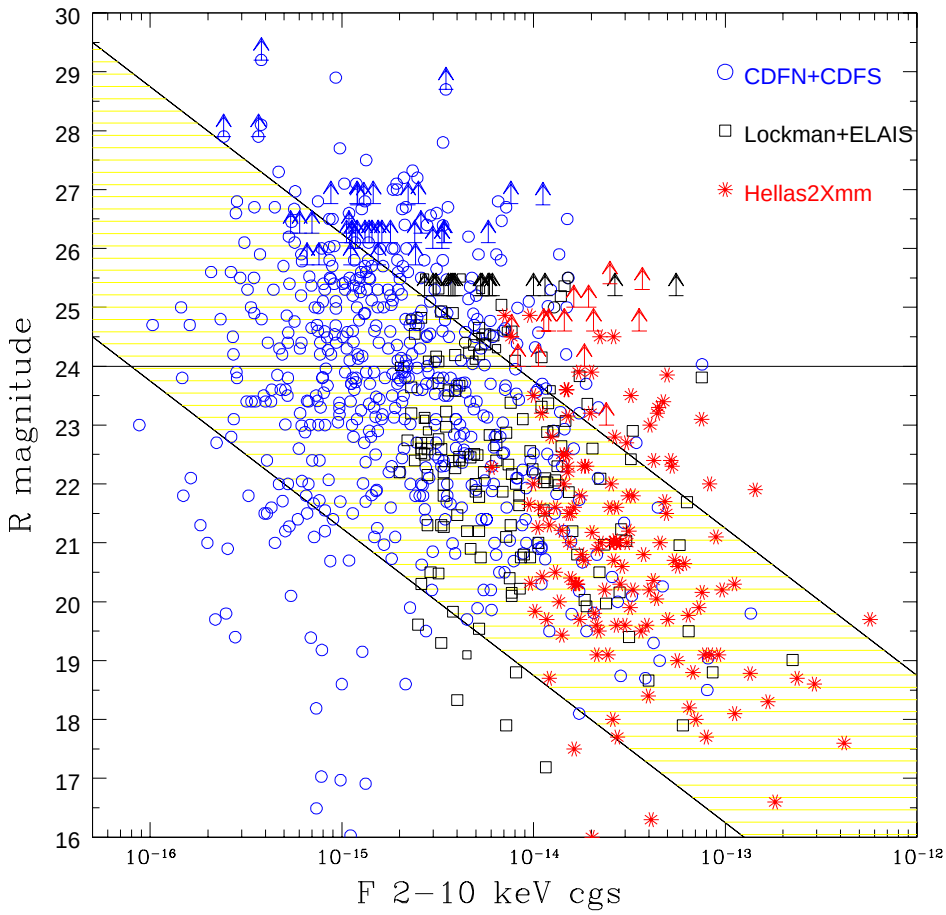

Figure 1.3 The 2–10 keV flux versus the R band magnitude for five different hard X–ray surveys. From bright to faint X–ray fluxes: *asterisks* mark the `HELLAS2XMM` sources (this PhD Thesis); *squares* refer to the sources in the Lockman Hole XMM–*Newton* observation (Mainieri et al. 2002) and in the ELAIS deep *Chandra* survey (Manners et al. 2003); *circles* mark the sources detected in the *Chandra* Deep Field South (Giacconi et al. 2002) and in the *Chandra* Deep Field North (Alexander et al. 2003; Barger et al. 2003). The shaded area represents the region occupied by known AGN (e.g. quasars, Seyferts, emission line galaxies) along the correlation $\log(X/O) = 0 \pm 1$. The horizontal straight line at R=24 represent a conservative limit for spectroscopic observations.

$-1 < log(X/O) < 1$ is a clear sign of AGN activity, since the majority of spectroscopically identified AGN in both ROSAT (e.g. Hasinger et al. 1998; Lehmann et al. 2001) and ASCA (Akiyama et al. 2000) surveys fall within this range, while normal galaxies and stars usually have lower ($log(X/O) < -2$) values.

const=5.5 (see Hornschemeier et al. 2000) and it can be used when datasets from different observations are compared.

The optical identification of sources discovered in deep and medium deep *Chandra* and XMM–*Newton* surveys confirms this trend to fainter X–ray fluxes and, at the same time, show evidence of a relatively large number of sources which deviate from $\log(X/O) = 0 \pm 1$ (Fig. 1.3). Indeed, the range of X/O now spanned by X–ray selected sources is extremely large, up to 6 dex or even more. Most important, an interesting new population of X–ray sources characterized by values of their X/O> 10 (i.e. sources that are optically weak with respect to the observed X–ray flux) is present in both deep and shallow surveys, and its fraction seems to be constant ($\sim 20\%$) over ~ 3 decades of fluxes.
Almost by definition, sources with X/O > 10 have faint optical magnitudes. For example, a 2–8 keV flux of $10^{-15}(10^{-16})$ erg cm^{-2} s^{-1}and an X/O=10 correspond to R magnitudes ∼25.5 (∼28), challenging (well beyond) the spectroscopic capabilities of 10m-class telescopes.
In this respect it is important to note that shallow, hard X–ray surveys, designed to sample relatively bright X–ray and optical fluxes, are best suited to investigate the nature of sources with high X/O: at fluxes of the order $10^{-14} - 10^{-13}$ erg cm^{-2} s^{-1}), the magnitudes of the optical counterparts of high X/O sources are of the order of $R \simeq 24$ or brighter, making spectroscopic follow–up observations feasible.
It seems reasonable to argue that most of the sources characterized by high X/O are high redshift, obscured AGN. If this were the case, they could contribute to reduce the disagreement between the redshift distribution predicted by XRB synthesis models and that observed in deep *Chandra* and XMM–*Newton* fields (Hasinger 2003; Gilli 2003), and provide an important contribution to the total energy density of the background light.

Black Hole demography

An important piece of observational evidence on how supermassive black holes (SMBHs) have assembled comes from the demography of the AGN population.
The tight correlation observed between the black hole mass and velocity dispersion of galactic bulges (the $M_\bullet$–σ relation, Gebhardt et al. 2000; Ferrarese & Merritt 2000) is generally taken as strong evidence that the growth of SMBH and the formation of galaxies go hand in hand (see, e.g., Ho 2004). The first implication of this relation is that most (if not all) galactic bulges contain "dormant" SMBHs. If this is the case, the observed local black hole mass density ($\rho_\bullet$) should be explained in terms of the overall black hole mass density accreted in the AGN phase. The BH mass density due to AGN can be estimated from the observed radiation(S) emitted by active black holes in a given energy band over the cosmic time, using the elegant Soltan's argument (Soltan 1982):

$$\rho_\bullet = \frac{1}{\eta c^2}\frac{4\pi k_{bol}}{c}(1+ < z >) \int S \, \frac{dn}{ds} \, dS. \qquad (1.2)$$

that, besides the knowledge of the differential counts ($\frac{dn}{dS}$) and of the average redshift of the peak of AGN activity ($\langle z \rangle$), requires $assumptions$ about the efficiency (η) of turning accreted rest-mass energy into radiated energy, and the bolometric correction (k_{bol}) which relates the total emissivity to the emissivity in the chosen band.

Hard X–ray surveys have already probed the largest fraction of the whole AGN population; this makes the results obtained from both deep and shallow surveys the most suitable to estimate the $total$ black hole mass density due to accretion. Moreover, given that the XRB spectral intensity records the bulk of the accretion power, the integral in Equation 1.2 can be rewritten:

$$\rho_\bullet = \frac{1}{\eta c^2} \frac{4\pi k_{bol}}{c} (1 + \langle z \rangle) I_0 \tag{1.3}$$

where $\langle z \rangle$ is the average redshift of the X–ray sources detected in the 2–10 keV band and I_0 is the absorption corrected XRB intensity in the same energy band.
Early estimates, made assuming the same evolution for obscured and unobscured sources (e.g. $\langle z \rangle$=2 observed for soft X–ray selected QSO) and coupled with the evidences that more than 80% of the accretion is obscured, led to a $\rho_\bullet = 6 \div 17 \times 10^5$ $M_\odot$ Mpc^{-3}, if a standard η=0.1 is adopted (Fabian & Iwasawa 1999; Elvis, Risaliti & Zamorani 2002).
With the data on hard X–ray selected active SMBHs rapidly accumulating, a lower value for $\rho_\bullet$ from AGN appears more plausible (see Fabian 2003 for a recent review). Moreover, now it is possible to safely (e.g. with the lowest number of arbitrary assumptions) compare the black hole mass density expected from the AGN activity with that observed in nearby galactic bulges (e.g. Haehnelt 2003).

Do Unified Schemes work?

As already shown, current synthesis models, built on a strictly X–ray based scheme, are far from being unique (see Comastri 2001 for a review); in particular, a simultaneous fit to all the observational constraints requires $at\ least$ to relax some of the key assumptions in Unified Schemes. Moreover, the broad band Spectral Energy Distribution (SED) of the XRB constituents, outside the X–ray domain, is essentially unconstrained, with the consequent lack of model predictive power at longer wavelengths. In this respect it is not surprising that the results of multi–wavelength follow–up from both shallow and deep surveys, have started to unveil that the sources responsible for a large fraction of the XRB energy density are characterized by broad band properties which are significantly different from those of AGN selected in the optical and soft X–ray bands (Barger et al. 2002, Giacconi et al. 2002; Willott et al. 2003). Although there are compelling theoretical and observational evidences which suggest that the large majority of the hard X–ray sources are obscured AGN, the origin of such a broad variety in their

multiwavelength properties is still far to be understood.
On the one hand, there is rather increasing evidence of the presence of luminous X–ray sources in the nuclei of galaxies without any evidence of optical nuclear activity nor of a high star formation rate in their optical spectra, which are instead typical of early-type "normal" galaxies (Hornschemeier et al. 2001; Giacconi et al. 2001; Barger et al. 2001; Comastri et al. 2002a,b). Moreover, there are evidences that the one–to–one relation postulated in Unified schemes between optical Type 1 and X–ray unobscured sources, and between optical Type 2 and X–ray obscured sources, does not hold expecially at high redshifts and luminosities (Brusa et al. 2003; Page et al. 2003).
On the other hand, the hard X–ray selection turned out to be very efficient in revealing an AGN population with optical to near–infrared colours redder than those of optically selected QSOs. In this respect, the discovery that a sizable fraction of hard X–ray sources are also associated to extremely red objects (EROs) with optical to near–infrared colour R-K > 5 (Lehmann et al. 2001; Mainieri et al. 2002; Alexander et al. 2002) is even more intriguing. The observed optical to near-infrared colors of EROs are consistent with both passively evolving elliptical galaxies at z$\sim$1 or with dust reddened starburst galaxies and obscured AGN. Given the key role played by this class of objects to constrain models for the formation and evolution of massive elliptical galaxies and star formation at high redshift, X–ray observations of those objects provide an exciting opportunity to investigate the link between galaxies and AGN evolution.

The goals of this PhD Thesis

The main goal of the present work is to provide further contributions to the understanding of the physical and evolutionary properties of AGN, which are necessary to derive the accretion history of super massive black holes that reside in most of galaxies.

In order to make significant progress in this direction the following issues will be addressed:

A) What is the nature and luminosity/redshift dependence of sources which seem to deviate from the simplest version of unified models? How many are they?

B) What is the nature of X–ray bright optically faint sources? What is their redshift? Are they highly obscured, high redshift AGN?

C) Which is the the evolution of hard X–ray sources? Is the evolution of low–luminosity AGN different from that of high–luminosity AGN? Is the relic Black Hole mass density accreted in the active phase consistent with the local one?

D) What are the optical/IR colors of obscured hard X–ray sources? How many hard X–ray sources are extremely red objects (EROs)? Conversely, what are the high energies properties of the near–infrared selected ERO population? How many infrared selected EROs are X–ray emitters?

Observations at high energies yield important information on the structure and nature of AGN; when coupled with deep optical and near–infrared (photometric and spectroscopic) follow-up, they provide constraints on the mass of the growing black holes and, therefore, are essential to better understand the nature of the various components of the X–ray background light and can be used as test for the accretion paradigm.In this framework, we have started a program of multiwavelength follow-up observations of hard X–ray selected sources serendipitously discovered in XMM–$Newton$ fields over ~ 4 deg^2 (the HELLAS2XMM survey; Baldi et al. 2002).
Conversely, optical and near–infrared surveys of galaxies are crucial to discriminate between different cosmological scenarios (e.g. hierarchical or monolithic growth of the structures) and, thus, to recover the galaxy

evolution path. With a complementary approach to that of hard X–ray surveys, in order to investigate the link between nuclear activity and the galaxy formation, XMM–*Newton* and *Chandra* observations of photometric and spectroscopically selected EROs have been obtained.

The HELLAS2XMM survey will be described in Chapter 1, with particular emphasis on the multiwavelength data obtained for the sources detected in ~ 1 deg^2, and on the importance of high spatial resolution observation in the optical identification process of hard X–ray sources counterparts.
In Chapter 2 I will present the multiwavelength properties of hard X–ray sources, as revealed from optical and X–ray spectroscopy of the brightest population responsible for the XRB energy density. In particular, I will focus the discussion on those sources which seem to deviate from the simplest version of unified models.
In Chapter 3 I will present spectroscopic identifications and near–infrared analysis of objects with high X/O selected in the HELLAS2XMM survey. I will also present different approaches developed to estimate the redshift of optically faint X–ray sources and needed to build an almost "complete" sample of hard X–ray selected sources.
In Chapter 4 the results from the HELLAS2XMM survey, complemented with those obtained from the deep surveys, will be used to derive the number and luminosity densities as a function of redshift. Observational constraints for the cosmic evolution, the integrated black hole mass density and the QSO2 will also be discussed.
In Chapter 5 the X–ray and optical properties of X–ray detected EROs from a large and complete near–infrared sample are presented, and compared with those of hard X–ray sources with similar R-K colors and QSO2. A selection criterion to pick up QSO2 on the basis of the observed optical, near–infrared and X–ray fluxes is proposed.
As a comparison with the results on X–ray detected EROs, in Chapter 6 the average high–energy properties of non–AGN EROs are investigated through the "stacking analysis" technique, and the existence of a dichotomy in the spectroscopic classification is confirmed also in the X–rays.
Finally, in the last Chapter, I will summarize the most important results of the present work and I will briefly discuss the implications for future observations.
I will assume a ΛCDM cosmology, with the following values for the Hubble constant and the cosmological parameters: H_0=70 km s^{-1} Mpc^{-1}, Ω_Λ=0.7, $\Omega_{\rm m}$=0.3 (Spergel et al. 2003).

Chapter 1

The HELLAS2XMM survey

The XMM–*Newton* High Energy Large Area Survey (hereafter HELLAS2XMM) has been originally conceived as the natural extension of the *Beppo*SAX HELLAS to the XMM–*Newton* capabilities, in order to fully exploit the larger throughput, effective area and better spectral and angular resolution of the new generation ESA satellite.
The HELLAS2XMM survey goal is to build a sample of $\sim$ 500 sources detected in ~ 4 square degrees at fluxes in the range of $\sim 10^{-14} - 10^{-12}$ erg cm^{-2} s^{-1}, and to provide for all the sources complete, medium–deep optical photometry, along with high signal–to–noise optical spectra and broad–band (e.g. radio and near infrared) multiwavelength coverage for most of the objects. The trade–off between the large area covered, the bright X–ray fluxes and the hard (2–10 keV) X–ray selection is essntial to obtain a statistically significant sample of obscured sources detected at fluxes where a significant fraction of the XRB is resolved ($\sim$ 50%; see, e.g., Comastri 2001 for a review) and at the same time optical spectroscopy is feasible with ground–based telescopes of the 4m and 8m classes.
This choice allow us to fill the gap between shallower hard X–ray surveys (HELLAS Fiore et al. 2001; ASCA LSS and MSS, Akiyama et al. 2003; SHEEP Nandra et al. 2004; XMM-HBS Caccianiga et al. 2004) and the recent deepest observations (CDFN – Barger et al. 2003, CDFS – Szokoly et al. 2004, Lockman Hole – Mainieri et al. 2002) (see Fig. 1.1).
The final aim of this project is to trace the accretion history in the Universe and to derive, over a wide range of redshifts and luminosities, the luminosity function of obscured AGN, to date basically unknown.

The project started at the beginning of 2001 and it is still on–going. The X–ray data and the log(N)–log(S) have been presented by Baldi et al. (2002). The sources are selected in a total of 20 XMM-*Newton* archival fields, the majority of them sharing a *Chandra* coverage, which, thanks to the higher angular resolution, helps in the process of optical identification (see Brusa et al. 2003).
At the time of writing, multiwavelength data have been fully exploited for

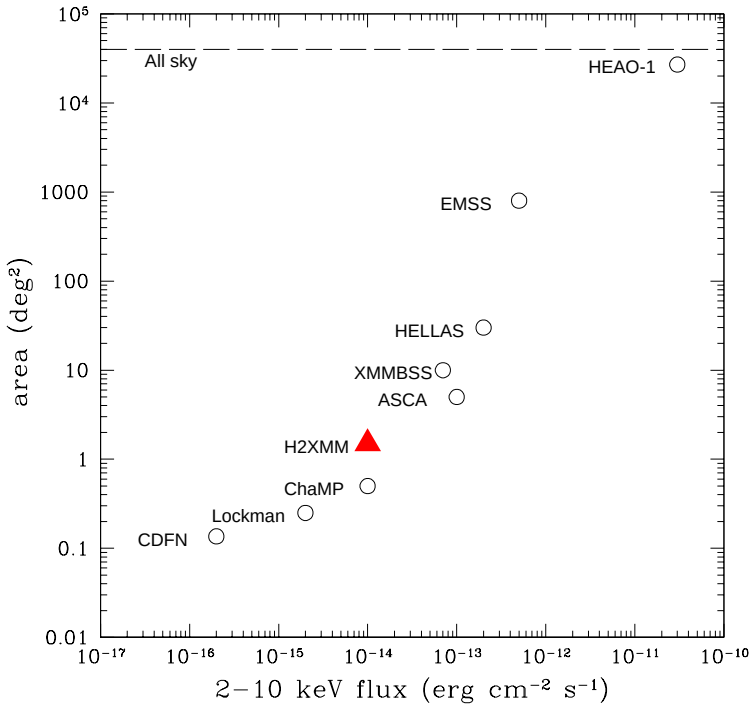

Figure 1.1 A compilation of extragalactic X–ray surveys in the 2–10 keV band. The surveyed area (Ω) is plotted against the limiting flux and is updated at the end of 2003. . Shown are the HEAO-1 survey, the *Einstein* Extended Medium-Sensitivity Survey (EMSS), the BeppoSAX High Energy LLarge Area Survey (HELLAS), the ASCA LSS survey, the XMM–BSS survey, the `HELLAS2XMM` survey (`HELLAS2XMM 1dF`, big triangle), the *Chandra* Multiwavelength Project (ChaMP), the deep XMM–*Newton* survey of the Lockman Hole (Lockman), the *Chandra* Deep Field North Survey (CDFN). The horizontal dashed line shows the solid angle of the whole sky.

a a sample of 122 sources detected in five XMM–*Newton* fields: around the bright quasars PKS0312-77 and PKS0537-28; around the cluster A2690; around the galactic star G158-100; and around the Seyfert galaxy Markarian 509. The multiwavelength data of these fields, covering a total of ~ 0.9 square degrees (hence the acronym '`HELLAS2XMM 1dF`' for this sample, Fiore et al. 2003) will be discussed in the next Section.
A specific field (the one surrounding the radio–loud quasar PKS 0312–77) is the best studied among the `HELLAS2XMM 1dF` sample, as it was the first with the largest coverage of multiwavelength observations. It will therefore be discussed in more details as a test case for the source identification process (see Sect. 2.2). In Sect. 2.3 and 2.4 the spectroscopic observations and breakdown, and the complete list of the sources in the `HELLAS2XMM 1dF` are reported.

1.1 Multiwavelength observations of the HELLAS2XMM 1dF sample

1.1.1 X–ray

The XMM–*Newton* observations of the five fields of the HELLAS2XMM 1dF sample have been obtained with the European Photon Imaging Camera (EPIC, Jansen et al. 2001), equipped with both the MOS and pn instruments. The data were processed using version 5.0 of the Science Analysis System* (SAS). The event files were cleaned up from hot pixels and soft proton flares. The hot pixels were removed using both the XMM–SAS and the IRAF† task *cosmicrays*, while for the proton flares a count rate threshold was applied removing all the time intervals with a count rate greater than 0.15 c/s in the 10–12.4 keV energy range for the two MOS and greater than 0.35 c/s in the 10–13 keV band for the pn unit (Baldi et al. 2002). The excellent relative astrometry between the three cameras (within 1″, below their FWHM of $\sim 6''$) allows us to merge the MOS and pn images in order to increase the signal to noise ratio and to reach fainter X–ray fluxes. An accurate detection algorithm developed by our group (Baldi et al. 2002) was run on the 2–10 keV cleaned event, in order to create a list of candidate sources. We then computed the probability that the detected counts originate from poissonian background fluctuations: 122 sources were detected above a detection threshold of p=2×10^{-5}. The count rate to flux conversion factor was derived assuming a power law with photon index Γ=1.7, absorbed by the Galactic column density toward the fields (Dickey & Lockman 1990), and weighted by the effective exposure time of the different EPIC cameras. The uncertainty in the derived fluxes is $< 15\%$ for $\Delta\Gamma = \pm 0.5$. The 2–10 keV fluxes range from $\sim 1 \times 10^{-14}$ to 4 $\times 10^{-13}$ erg cm^{-2} s^{-1}.
The same detection algorithm was also run in the 0.5–2 keV energy range in order to characterize the average spectral properties of the sources in our sample using the hardness–ratio technique.

For the sources in the sample with at least 40 counts in the combined pn + MOS datasets (all but three), the source spectrum and associate background and response files have been extracted from the original event files, in each of the XMM–*Newton* detector, using the standard SAS procedures (Puccetti, PhD Thesis). In the majority of the cases, the spectral counts were fitted using the X–ray spectral fitting package XSPEC‡ (version 11.2.0) and the χ^2 statistic with a simple absorbed power–law model, in order to derive the intrinsic N$_H$. When the spectral counts were lower than 120, the C-statistic (Cash 1979) was used instead.
The source with spectroscopic redshifts and those without were treated

*http://xmm.vilspa.esa.es/external/xmm_sw_cal/sas_frame.shtml

†IRAF is distributed by the National Optical Astronomy Observatories, which is operated by the Association of Universities for Research in Astronomy, Inc, under cooperative agreement with the National Science Foundation.

‡http://heasarc.gsfc.nasa.gov/docs/xanadu/xspec/

separately (see also Sect. 3.1 and 3.2); a detailed description of the spectral fitting procedures and results is reported in Perola et al. (2004) and Puccetti (PhD Thesis).

1.1.2 Optical Imaging and source identifications

All the five fields in the HELLAS2XMM 1dF sample were selected in the southern emisphere, in order to make extensively use of the facilities of the European Southern Observatory (ESO). We have obtained relatively deep (R=24-25) optical images for **all of the 122** hard X–ray sources in the HELLAS2XMM 1dF sample using EFOSC2 at the ESO 3.6m telescope. Exposures were typically of 600 s per image. Each R-band frame was cross-matched to the USNO catalog(Monet et al. 1998) and astrometrically calibrated using the package GAIA[§]. We obtained a good astrometric solution for each frame, with r.m.s. in each coordinate of about 0.1-0.2″.

The images were reduced using standard techniques including de–bias, flat–fielding, and fringing correction (if needed). The photometric calibration was performed for each night using the zero-point derived from the measured instrumental magnitudes of standard stars and assuming the average extinction reported in the Observatory web page[¶].
The optical source catalogue was created using the SExtractor software (Bertin & Arnouts 1996). Since the images have been obtained under different seeing conditions, the limiting magnitude has been conservatively estimated in each frame as the 3σ (sky value) over 2.5 times the seeing area. Using this definition, the limiting magnitudes range between 24.0 and 25.2, mainly depending on the image seeing.

Optical frames and X–ray images were brought to a common astrometric reference frame: we have accounted for the astrometric calibration of the X–ray images by looking for average displacement of bright Type 1 AGN (from 5 to 15 AGN) in the fields. Typical systematic shifts were of the order of 1″, the maximum shift was of $\sim 2''$.
We have also verified the effects of possible scale and rotational offsets in the matched astrometric solutions, that turned out to be negligible. The uncertainties in the determination of the X–ray positions are mainly ascribed to the XMM–*Newton* PSF, in particular at faint X–ray fluxes where the statistical error in RA and DEC determination are expected to be in the range 1-2″(see Sect. 6.3 in the First XMM-Newton Serendipitous Source Catalogue: 1XMM, User Guide to the Catalogue).

In order to accommodate any residual systematics in the astrometric calibration of the EPIC images (see Barcons et al. 2002) and to fully account for the PSF broadening in faint sources (e.g., sources with <100 cts), we have searched for optical counterparts for all the X–ray sources within a

[§]version 2.3-1 driven P.W. Draper from the Skycat software developed by ESO
[¶]http://www.eso.org/observing/support.html

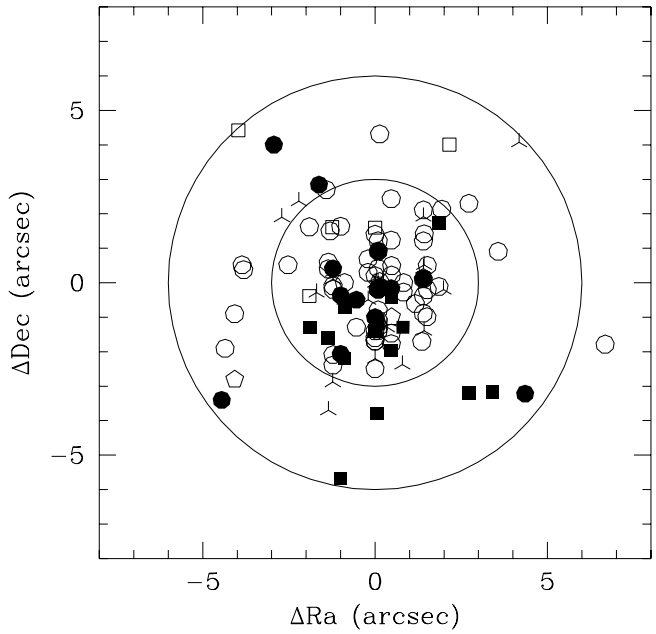

Figure 1.2 The displacement between the X–ray position and the position of the nearest optical counterpart for the HELLAS2XMM 1dF sample sources. Open circles = broad line AGN; filled circles = narrow line AGN; filled squares = emission line galaxies; open squares = normal galaxies; stars = stars; pentagons = clusters of galaxies; skeleton triangles = unidentified objects. The two circles have radii of 3 and 6 arcseconds.

conservative matching radius of 6″ from the astrometrically corrected X–ray centroid.

We found optical counterparts brighter than R$\sim$ 25 within $\sim$ 6″ from the X–ray position in 116 cases (actually within 3″ for $\sim$ 80% of the cases, see Fig. 1.2). The average displacement between the X–ray positions and the positions of the optical counterparts is of $2.1'' \pm 1.5''$. This is consistent with what found in other XMM–*Newton* surveys (Barcons et al. 2002; Hasinger et al. 2001). Six (5%) X–ray sources have optical counterparts fainter than R$\sim$ 25.

A better X–ray–optical matching is achieved for the X–ray brightest sources, generally characterized by the sharpest PSF. This is shown in Fig. 1.3, where the displacements between the optical and X–ray positions for the sources detected in the field of PKS 0312–77 (Brusa et al. 2003) are reported as a function of the off–axis angle and of the X–ray flux (X–ray brightest objects are associated with the smallest symbols). For the brightest sources, the displacement from the most likely optical counterpart is $< 2''$ even at large off-axis angles ($> 12'$). The average displacement ($\sim$ 2 arcsec) of the X–ray

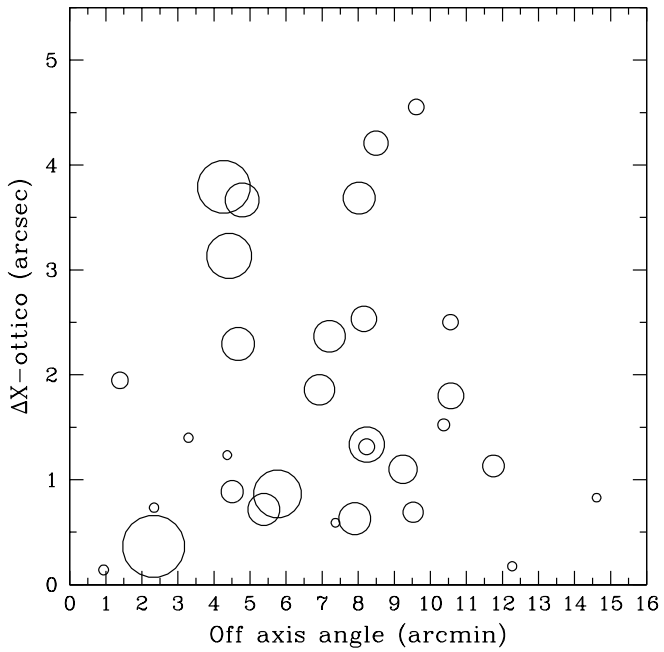

Figure 1.3 Displacements between the optical and X–ray positions as a function of the off–axis angle for the sources detected in the PKS 0312 field. The size of the symbols increases as the X–ray flux decreases.

faintest sources are consistent with those expected at these flux levels (see above). The residual astrometric differences between the X–ray and optical positions do not show any clear trend with the off–axis angle between 4 and 11 arcmin, where the bulk of the sources are detected.

We decided to adopt a statistical approach to securely identify the optical counterpart responsible for the X–ray emission, when two or more objects were detected in the XMM–*Newton* error circle. For each counterpart detected within 6″ from the X–ray position, we have computed the probability to find by chance an object within this radius: $P = 1 - e^{-\pi r^2 n(m)}$, where r is the distance between the X–ray and optical sources, and $n(m)$ is the surface density of galaxies at a given magnitude and it is derived from the number magnitude relation of field galaxies reported by Pozzetti & Madau (2000). If more than one counterpart is present, the most likely candidate is that with the lowest value of P.
A detailed description of the characterization of the hard X–ray counterparts is reported in Sect. 1.2.1.

1.1.3 Near–infrared

Deep K_s[‖] observations of a well–defined sample of peculiar sources in the HELLAS2XMM 1dF sample (11 sources undetected in the R–band and 4 X–ray Bright Optically Normal Galaxies) have been obtained with the Infrared Spectrometer And Array Camera ($ISAAC$, see Moorwood et al. 1999) mounted on the ESO/VLT telescope. The observations have been collected in service mode over several nights in September 2002 under good seeing conditions ($<0.8''$), with net exposure time of 36 min for each field. The data reduction has been performed in two steps: individual raw frames have been first corrected for bias and dark current, and flat-fielded using standard IRAF routines. For the sky subtraction and image co-adding we then used DIMSUM[**] a contributed package of IRAF. The final co-added images show flat, zero-leveled backgrounds and stable PSFs over the field of view. We estimated a 50% completeness at $K_s \approx 21$ by comparing our data with deeper surveys (e.g., Saracco et al. 2001; Bershady et al. 1998). Object detection has been performed running SExtractor (Bertin & Arnouts 1996) on the final co-added images; a detailed discussion on data reduction and analysis techniques is reported in Mignoli et al. (2004).

1.1.4 Radio

Radio (5 GHz) observations of the field of PKS 0312–77 were performed with the Australian Telescope Compact Array (ATCA) in the 6-km configuration (maximum baseline length), with a synthesized beam size (HPBW) of $\sim 2''$. The data were analyzed with the software package MIRIAD. Each bandpass was calibrated and cleaned separately to produce two individual images that were combined together into a single mosaic at the end of the reduction phase. Self–calibration was used to make additional correction to the antenna gains and to improve the image quality. The final maps have uniform noise of 50 μJy (1σ) over an area with a semicircular shape (due to the odd numbers of pointings) with a radius of about 10 arcmin, surrounded by an area where the noise increases for increasing distance from the center. The accuracy on the radio position is of the order of $\sim 2''$ for the faintest objects.

Observations of the A2690 and G158 fields have been obtained with the Very Large Array (VLA) Telescope, at 1.4649 GHz and 1.3851 GHz with a bandwitdth of 50 MHz, in B configuration. All the data were analysed using the NRAO AIPS reduction package. The data were calibrated using source 0137+331 as primary flux density calibrator (assuming a flux density of 15.4935 Jy at 1.4649 GHz and 16.1955 Jy at 1.3851 GHz) and the source 2333-237 as secondary calibrator.
The on–axis noise is of ~ 37 μJy (1σ), and increases up to ~ 60 μJy for the

[‖]The K_s (*K short*) filter is centered at shorter wavelength than the standard K filter in order to reduce thermal background.

[**]Deep Infrared Mosaicing Software, developed by P. Eisenhardt, M. Dickinson, A. Stanford and J.Ward, and available at ftp://iraf.noao.edu/contrib/dimsumV2

sources detected at large offaxis angles due to the primary beam attenuation. The accuracy on the radio position is of the order of $\sim 2''$ for the faintest objects.

Finally, source lists in the PKS 0537 and MKN509 fields have been cross–correlated, using a conservative searching radius of 15″, with the public NRAO/VLA Sky Survey radio catalog (NVSS, Condon et al. 1998; version 2.17), that contains sources with peak brightness in excess than 2.25 mJy (5 σ) at 1.4 GHz.

Given the difference in the limiting fluxes in the different fields, the full radio database is not homogeneous and could not be used for statistical purposes. However, the radio information (positional accuracy and radio flux, when available) has been extensively used in the identification of the X–ray counterparts and in the study of peculiar objects, respectively.

1.1.5 Additional X–ray observations: *Chandra* data

The XMM–*Newton* fields of PKS 0312–77 and PKS 0537–28 were also observed by *Chandra*, the first as part of the Performance and Verification phase of the satellite, the second in the framework of the `HELLAS2XMM` project.
The data were analyzed using version 2.2 and 3.0 of the *Chandra* Interactive Analysis of Observations (CIAO) software[††]. The high–background intervals were filtered out leaving about 24.7 and 20 ksec of useful data, respectively. The `WAVDETECT` algorithm (Freeman et al. 2002) was run on the cleaned full band (0.5–8 keV) images setting a false–positive threshold of 10^{-7}, which led to highly reliable detections, as shown in the CDFN field (e.g., Brandt et al. 2001a).

1.2 The PKS 0312 field: a test case of multiwavelength follow–up observations

The field around the bright quasar PKS 0312–77 has been observed both by *Chandra* and XMM–*Newton* during their Calibration and Performance Verification (PV) phases; deep radio observations at 5 GHz have been obtained with the ATCA telescope, along with the optical imaging at the ESO 3.6m telescope for the 35 objects detected in the combined *MOS1* + *MOS2* + *pn* XMM–*Newton* observation. Optical spectroscopy has been obtained for 28 sources, both at the ESO 3.6m and VLT/FORS1 telescopes. Finally, near–infrared observations for a dozen of objects have been obtained with ISAAC at VLT.
All the data have been already presented in the previous Sect. and are extensively discussed in Brusa et al. (2003) and Fiore et al. (2000, 2003). In the following I describe the identification process that, thanks to the

[††] http://cxc.harvard.edu/ciao/

radio, near–infrared and *Chandra* positional accuracy ($\sim 1''$), allowed us to unambiguously identify all but one of the optical counterparts of the 35 hard X–ray sources.

In Table 2.1 are reported all the relevant multiwavelength data for the 35 sources detected in the XMM–*Newton* observation

1.2.1 X–ray sources identification

At first, we have accounted for the astrometric calibration of the X–ray image by looking for average displacement of bright Type 1 AGN already identified in Fiore et al. (2000). We found an average shift of $\sim 2''$ (Δ(Ra)=1.67″; Δ(dec)=$-1.13''$), in agreement with the findings reported in Lumb et al. (2001), where the astrometric calibration was done with respect to the position of the bright central target.

Thirty–one X–ray sources have one or more optical counterparts brighter than R$\sim$24.0 within the XMM–*Newton* error box, while for four objects there are no obvious counterparts down to the magnitude limits of the optical images (see Sect. 1.1.2). The probability threshold adopted in the X–ray detection algorithm corresponds to less than 1 spurious X–ray detection. We are then confident that also X–ray sources without optical counterparts are real X–ray detections and in the following we address to these objects as blank fields. The displacements between the optical and X–ray positions as a function of the off–axis angle are reported in Fig 1.3 and the behaviour has been already discussed. For each of the 29 XMM–*Newton* sources covered by radio observations we also searched for radio sources within the X–ray error box (6″ radius). We found 5 X–ray/radio associations, while for the remaining 24 X–ray sources we report the 3σ upper limit (see Table 2.1)

1.2.2 Confusion problems

The additional *Chandra* data of the PKS 0312–77 field allowed us to quantitatively investigate confusion problems of X–ray sources, i.e. when the measured X–ray emission is indeed originated from two or more X–ray sources at a distance comparable to the XMM–*Newton* PSF. This could in principle be the case for four out of 31 sources, for which two candidate optical counterparts fall within the XMM–*Newton* error circle (sources 20, 22, 127, and 18 in Table 2.1). Only in one case (source 18, also known as P3, see Sect. 2.3.1) two objects are clearly resolved by *Chandra* within the XMM–*Newton* detection (see Fig. 2.4); the X–ray flux of the faintest source is only about 10% of the claimed counterpart, suggesting that most of the XMM–*Newton* flux belongs to P3. The subarcsec positional accuracy of *Chandra*, coupled in one case with the detection in the K–band, allows to unambiguously identify the correct optical counterparts of the remaining three sources and to exclude that two individual X–ray sources contribute to the measured XMM–*Newton* flux (see Fig. 1.4 for an example).

The multiwavelength coverage of our survey turned out to be extremely

Multiwavelength properties of the X–ray sources detected in the XMM–*Newton* observations

ID	XMM position RA	DEC	$\Delta_{XMM-opt}$ ["]	$\Delta_{Chandra-opt}$ ["]	P	S_{5Ghz} [mJy]	R	F_{2-10} [10^{-14} cgs]	HR	z	Class
12	03 15 29.36	−76 53 41.61	2.50	...[a]	< 0.01	...	21.0	2.78±0.74	−0.52 ± 0.10	0.507	AGN 1
20	03 14 16.76	−76 55 59.51	2.37	1.42	< 0.01	< 0.219	21.5	1.52±0.47	−0.44 ± 0.14	0.964	ELG
10	03 14 16.36	−76 45 36.51	0.69	2.60[b]	< 0.01	...	19.6	2.13±0.61	−0.65 ± 0.09	0.247	AGN 1
22	03 13 48.96	−76 45 59.41	1.31	0.31	< 0.01	...	21.6	2.71±0.58	−0.21 ± 0.13	2.140	AGN 1
36	03 13 43.55	−76 54 26.26	3.47	4.77	0.013	< 0.165	>24.6	1.45±0.47	−0.23 ± 0.19	...	...
13	03 13 34.26	−76 48 29.71	0.86	0.66	< 0.01	< 0.360	19.7	1.17±0.38	−0.56 ± 0.11	1.446	AGN 1
3	03 13 14.66	−76 55 55.81	1.23	1.04	< 0.01	< 0.150	18.3	16.72±1.03	−0.41 ± 0.03	0.420	AGN 1[†]
5	03 13 11.96	−76 54 29.71	1.40	0.64	< 0.01	< 0.168	19.1	8.37±0.68	−0.37 ± 0.04	1.274	AGN 1[†]
127	03 12 57.96	−76 51 20.31	0.36	0.55	< 0.01	< 0.159	23.5	1.00±0.29	0.36 ± 0.27	2.251	AGN 1
65	03 12 52.16	−77 00 59.51	...*	...*	...	< 0.300	>24.0	1.84±0.51	0.11 ± 0.21	...	...
6	03 12 53.96	−76 54 14.51	0.73	0.70	< 0.01	< 0.150	22.0	8.28±0.66	−0.26 ± 0.05	0.683	AGN 2[†]
18	03 12 39.26	−76 51 32.61	1.94	1.29	< 0.01	< 0.150	18.0	2.59±0.39	0.00 ± 0.11	0.159	GAL[†]
8	03 12 31.16	−76 43 24.01	1.10	0.62	< 0.01	...	13.7[e]	1.64±0.52	−0.72 ± 0.07	0.0517	GAL/
			2.90	1.49						0.0537	group?
			2.16	2.15						0.0517	
4	03 12 09.16	−76 52 13.01	0.14	0.60	< 0.01	< 0.225	18.2	6.49±0.56	−0.57 ± 0.03	0.890	AGN 1[†]
16	03 12 00.36	−77 00 25.61	0.63	1.33	< 0.01	6.545±0.500	22.2	1.51±0.46	0.81 ± 0.34	0.841	ELG
89	03 11 44.96	−76 56 45.01	2.29	1.13	0.054	< 0.150	23.6	1.48±0.37	0.33 ± 0.23	0.809	ELG
181	03 11 35.96	−76 55 55.81	3.79	...[c]	0.104	0.230±0.050	23.2	1.10±0.32	0.83 ± 0.35	0.709	ELG
35	03 11 31.76	−77 00 36.31	4.21	...[a]	0.048	< 0.360	22.0	1.83±0.53	−0.17 ± 0.18	1.272	AGN 1
			0.60[h]	...[a]	...	0.364±0.073	> 24.6			...	...
66	03 11 28.16	−76 45 16.31	3.68	...[d]	0.09	...	23.1	1.51±0.46	0.09 ± 0.20	1.449	AGN 1
17	03 11 24.76	−77 01 39.01	4.55	...[a]	< 0.01	1.298±0.088	17.7	2.74±0.60	−0.30 ± 0.13	0.320	BL Lac
31	03 11 13.86	−76 53 59.11	...*	...*	...	< 0.150	> 24.6	1.20±0.33	−0.17 ± 0.16	...	...
29	03 11 13.36	−76 54 31.11	3.13	1.57	< 0.01	< 0.150	18.7	1.21±0.33	−0.24 ± 0.16	...	...
11	03 11 12.76	−76 47 01.91	1.86	1.50	< 0.01	< 0.366	21.5	1.56±0.49	−0.59 ± 0.09	0.753	AGN 1
9	03 11 05.56	−76 51 58.01	0.89	0.13	< 0.01	< 0.150	23.2	1.98±0.38	−0.45 ± 0.08	1.522	AGN 1
7	03 10 49.96	−76 39 04.01	0.83	...[a]	< 0.01	...	18.6	29.2±3.10	−0.19 ± 0.07	0.381	AGN 1
21	03 10 49.76	−76 53 16.71	0.72	0.24	< 0.01	< 0.150	22.3	1.51±0.36	−0.28 ± 0.13	2.736	AGN 1
28	03 10 37.36	−76 47 12.71	2.53	1.09	< 0.01	< 0.366	20.8	1.78±0.46	−0.23 ± 0.14	0.641	ELG
45	03 10 18.96	−76 59 57.91	...*	...[a]	...	< 0.171	> 25.0	1.94±0.57	0.09 ± 0.20	...	...
2	03 10 15.76	−76 51 33.21	0.59	0.64	< 0.01	9.284±0.073	17.6	41.6±1.60	−0.44 ± 0.02	1.187	AGN 1[†]
124	03 10 01.60	−76 51 06.71	1.33	1.88	< 0.01	< 0.300	22.5	1.41±0.45	−0.25 ± 0.18		...
501	03 09 52.16	−76 49 27.41	...*	...[a]	...	< 0.279	>24.5	1.36±0.45	1 ± 0.40	...	...[f]
14	03 09 51.16	−76 58 24.71	1.52	...[a]	< 0.01	< 0.150	18.4	3.97±0.70	−0.20 ± 0.10	0.206	Starburst
24	03 09 31.66	−76 48 45.01	1.80	...[a]	< 0.01	< 0.546	21.8	1.76±0.54	−0.52 ± 0.13	1.838	AGN 1
116	03 09 18.46	−76 57 59.31	1.13	...[a]	0.017	< 0.183	23.9	2.01±0.67	0.74 ± 0.36	0.814[g]	ELG
34	03 09 12.06	−76 58 25.91	0.17	...[a]	< 0.01	< 0.222	19.1	9.24±1.13	0.45 ± 0.10	0.265	AGN 2

Table 1.1 * blank field; [a] out of *Chandra* ACIS–I field; [b] at the edge of ACIS field; [c] CCD gap; [d] not detected; [e] the R–band magnitude refer to the three nuclei altogether (see §5.3); [f] we note that a R=20.1 counterpart lies at 5.9″ from the XMM centroid; [g] redshift based on a single faint line; [†] sources reported in Fiore et al. 2000

useful to investigate confusion problems also for the sources for which *Chandra* data are not available. The closest optical counterpart of source 35 (R=22), at a distance of $\sim 4''$ from the X–ray centroid, has been identified with a Broad Line AGN at z=1.272; given the AGN surface density at these faint optical magnitudes ($\sim$100 deg^{-2} at R=22, assuming a B-R color of 0.6; Koo & Kron 1988), the corresponding probability that the source lies entirely by chance in the XMM–*Newton* error box is 6.0×10^{-4}. However, a relatively bright ($S_{5GHz} \sim 0.4$ mJy) radio source, associated with an optically blank field (R> 24.6, see Fig. 1.5) is almost coincident with the X–ray centroid. A bright (K=18.5) source clearly emerges in the infrared band at the position of the radio source; the $R - K$ color > 5.1 places this source among the

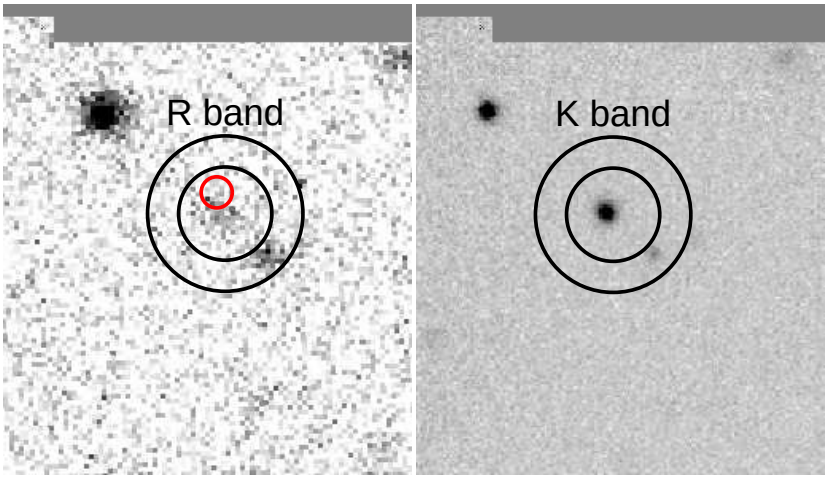

Figure 1.4 (*left panel*) R–band image of source 127. The small $1''$ circle represents the position of the source detected by *Chandra*; the $3''$ and $5''$ large circles are centered on the XMM–*Newton* position; (*right panel*) K–band image for source 127.

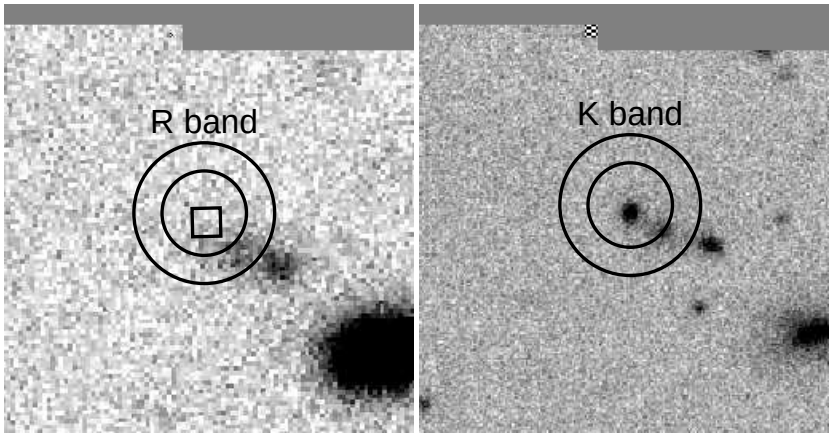

Figure 1.5 (*left panel*) R–band image of source 35. The small $1.5''$ width box represents the radio detection position, the $3''$ and $5''$ large circles are centered on the XMM–*Newton* position; (*right panel*) K–band image for source 35.

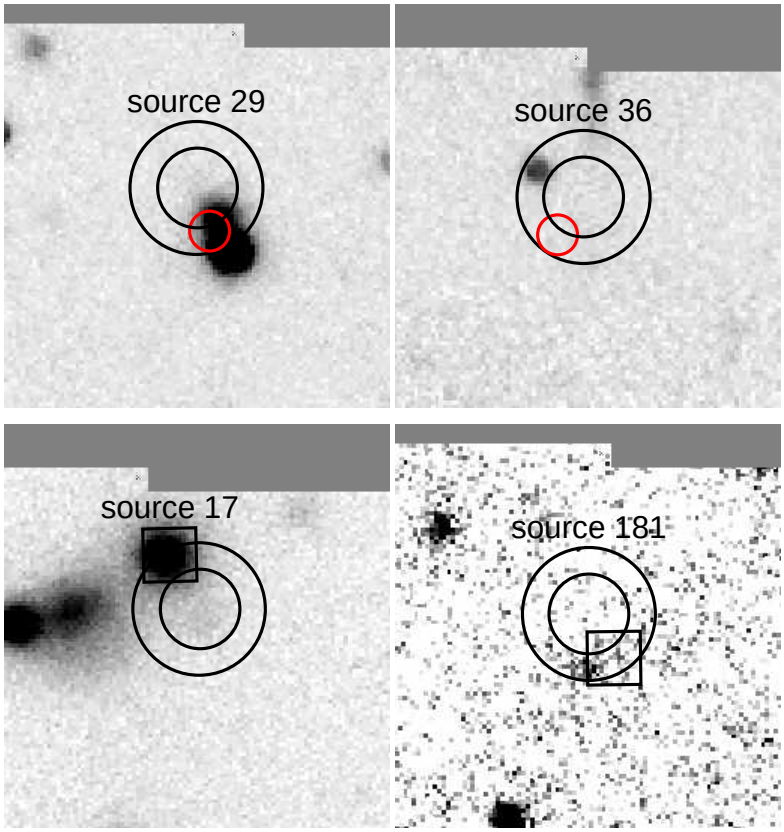

Figure 1.6 EFOSC2 R–band images of 4 sources at a distance$> 3''$ from the XMM–*Newton* centroid. The $3''$ and $5''$ large circles are centered on the XMM–*Newton* position. (*top panels*) sources 29 and 36: the small circles refer to the *Chandra* centroid and indicate a radius of $1.5''$; (*bottom left panel*) source 17 and 181: the squares refer to the radio centroids ($4''$ width). See Sect. 3.2 for details.

Extremely Red Object (ERO; $R - K > 5.0$) population. Given the EROs surface density at K< 18.5 ($\sim$800 deg^{-2}, Daddi et al. 2000) and the fraction of radio–emitters EROs at this level ($< 10\%$, see, e.g., Smail et al. 2002) the corresponding probability that a radio emitting ERO lies entirely by chance in the XMM–*Newton* error box is $< 5.0 \times 10^{-4}$. It is then likely that both the Broad Line AGN and the ERO contribute to the measured X–ray emission, although on the basis of the chance coincidence argument we are not able to definitely disentangle the contribution of each source; therefore, we have associated half of the X–ray flux to the Broad Line AGN and half to the ERO.

Sources at distance $> 3''$

Twenty–five out of 31 sources in the present sample show optical counterparts within a $3''$ radius from the XMM–*Newton* centroid. The probability P of chance coincidence, as defined in Sect. 1.1.2, is in all cases,

but one (see Table 2.1) lower than 0.01, strongly supporting the reliability of our identifications.
The *Chandra* and radio detections turned out to be extremely useful to identify five out of the six remaining sources for which the closest optical counterpart lies between 3 and 5 arcsec from the XMM–*Newton* centroid (Fig. 1.6):

- the optical counterpart of source 29 ($r \simeq 3''$) is a galaxy very close to a bright F/G star; it lies at $\sim 1.5''$ from a *Chandra* source and it is most likely the correct identification.
- a *Chandra* source within the XMM–*Newton* error box of source 36 lies at $\sim 4.8''$ from the possible optical counterpart which therefore cannot be the correct identification. In the following we refer to this source as an optically blank field.
- the radio detection of the optical counterpart of source 17 ($r = 4.5''$) strongly suggests that the identification is secure;
- a faint radio source, detected at the 3.5σ level at $\sim 3''$ from the nearest optical counterpart of source 181 is likely to be the correct identification given the uncertainty on the radio position ($2 - 3''$)
- source 35 has been already discussed in the previous subsection.

The remaining object (source 66) is associated with a faint optical counterpart (R=23.1), classified as a Broad Line AGN, at a distance of $3.7''$. Given the AGN surface density at these faint magnitudes ($\sim$300 deg^{-2}, Mignoli et al. 2002) the probability of chance coincidence is 1.8×10^{-3}; we are therefore confident that the identification is correct.

The relative shifts between X–ray and optical centroids are plotted in Fig. 1.7 and also reported in Table 2.1).
Thanks to the extremely good positional accuracy of *Chandra*, complemented by medium–deep radio and K–band observations, we have unambiguously identified the optical counterparts of $\sim$85% of the hard X–ray selected sources (29 out of 35 X–ray sources); only in one case (source 35) we cannot provide an unique identification. As a consequence, the spectroscopic completeness of the present sample is limited only by the faintness of the optical counterparts: five X–ray sources turned out to be optically blank fields at the limit of our images.
Taking into account the *Chandra* coverage of the XMM–*Newton* field, coupled with radio and infrared data we have revealed confusion problems in 2 out of 35 sources ($\sim 6\%$) at an X–ray flux level of about 10^{-14} erg cm^{-2} s^{-1}.

1.2.3 Comparison with different detection algortihms

A list of serendipitous sources detected in XMM–*Newton* observation of the field of PKS 0312−77 has already been published by Lumb et al. (2001,

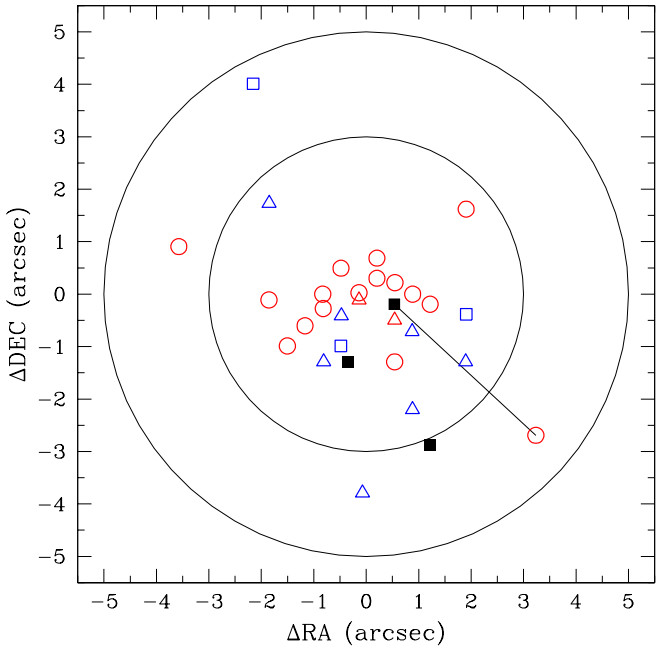

Figure 1.7 Displacement between optical and X–ray positions of the proposed optical counterparts of the X–ray sources in the PKS 0312–77 field, after the astrometric calibration. Symbols are as follows: open circles are Broad Line AGNs, open triangles are Narrow Emission–line objects (Narrow Line AGNs and ELGs), empty squares are galaxies, and filled squares are spectroscopically unidentified sources. The solid line connects the two possible counterparts of source 35 (see Sect. 3.1). The circles refer to the XMM–*Newton* error circles of 3" and 5", respectively.

hereinafter L01) and is included in the First XMM–*Newton* Serendipitous Source Catalogue (SSC)[‡‡] : this allowed us to perform a critical comparison between the number of detected sources and their X–ray fluxes, obtained with differeny methods, on the basis of the available information.

- L01: Using a sliding–cell detection algorithm (the XMM–SAS task EBOXDETECT) and a detection threshold of 5σ, 52 sources were detected in the soft (0.5–2 keV) band; for 47 of these sources the 2–10 keV flux was also reported.

- SSC: A total of 142 sources were detected in at least one of the five different energy bands (0.2-0.5; 0.5-2; 2-4.5; 4.5-7.5; 7.5-12 keV) and/or in one of the three EPIC cameras, with a maximum likelihood parameter (ML, from the task EBOXDETECT) larger than 8.

[‡‡]2003, Version 1.0.1, released by the XMM-Newton Survey Science Centre, http://xmmssc-www.star.le.ac.uk/

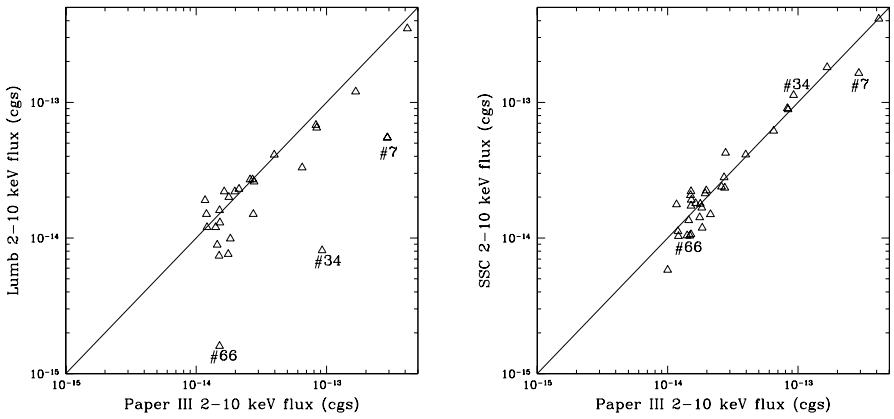

Figure 1.8 (*Left panel*) Comparison between the 2–10 keV fluxes of the sources detected in the PKS0312 field with our procedure and those estimated by L01 for the 27 common sources. The solid line represent the relation 1:1 between the two fluxes estimated. Three sources discussed in the text are also shown in the plot. *Right panel* As the *left panel*, but for the 32 PKS0312 common sources in the SSC and our samples.

The comparison between our sample, L01 sample and SSC sample is not straightforward due to the different detection algorithms, thresholds, band selection and, partly, to the different versions of the analysis software adopted in the data reduction. We also note that the L01 results have been obtained on the basis of preliminary calibrated data.
There is a significant difference in the total number of X–ray detected sources. The origin of this discrepancy could be mainly ascribed to the hard X–ray selection of our sample. Twenty-seven of the 35 sources in our sample have been reported by L01; 32 of the 35 sources have also been detected by the SSC when the detection in the 2-4.5 keV band (the energy range closest to the 2–10 keV band where the signal-to-noise ratio is maximized) is considered. We note that all of the sources in common between L01 and our sample are also included in the SSC sample. The five sources which belong to our sample and the SSC catalogue only (# 127, 65, 16, 89, and 45 in Table 1) are detected with ML>12 in the SSC 2-4.5 keV band; therefore we consider these sources as highly reliable. The absence of these sources in L01 is likely due to their hard X–ray spectrum (all of them have HR>0; see Table 1). Three sources are reported in our catalogue (# 181, 501, and 116) but not in the L01 and SSC ones; they are the hardest sources in our sample, and appear robust X–ray detections by visual inspection. The lack of these objects in the L01 and SSC sample is most likely due to the hard X–ray selection. Four sources reported in L01 with fluxes brighter than our flux limit are not present in our sample, although they are included in the SSC catalogue. Their non-detections in the SSC 2-4.5 keV band and their soft X–ray colors (quoted in Table 1 of L01) justify their absence in our 2-10 keV sample.

We have also compared the flux measurements of individual objects detected above the limiting flux of our survey ($F_{2-10} \simeq 10^{-14}$ erg cm^{-2} s^{-1}) which are in common in the three samples reported above. Our investigation reveals that the L01 fluxes are typically lower than ours by $\sim$ 25–30% at fluxes $\gtrsim 3 \times 10^{-14}$ erg cm^{-2} s^{-1} (see Fig. 1.8, *left panel*). Since the fluxes in the two samples have been computed assuming the same spectral model ($\Gamma = 1.7$ and Galactic absorption), the differences are likely to be due to a different correction adopted for the encircled energy fraction. This is particularly pronounced for the bright sources detected at large off–axis angles (see, e.g., source # 7). Two sources in the L01 sample deviate by more than one order of magnitude from our flux measurements (# 34 and # 66); we think that this is likely due to typos in Table 1 of L01.
Conversely, there is a good agreement between our fluxes and the SSC ones (see Fig. 1.8, *right panel*) for the 32 common sources. This result gives further support to the reliability of our flux estimates. The SSC 2-10 keV fluxes have been computed using the summed count rates in the 2-4.5 and 4.5-7.5 keV bands extrapolated to the 2-10 keV band assuming the same spectral model adopted in this paper.

1.3 Optical spectroscopy

The spectroscopic follow–up observations of the optically bright population (sources with R< 22) have been performed with the ESO 3.6m telescope equipped with EFOSC2 during three different observing runs (for a total of 9 nights from Jan 2001 to Nov 2001). We used mostly the EFOSC2 grism #13 with a 1.5 arcsec slit, which yields a dispersion of about 2.8 Å per pixel and provides a good spectral coverage up to 9000 Å. The exposure times vary between 600 and 2400 s, depending on the target magnitude.
The spectroscopic follow–up of the remaining sources with R$=22-24$ has been performed in service mode with the ESO VLT/UT2 telescope equipped with FORS1 during period 69. A total of 24 hours of VLT time have been devoted to this program. The grism 150I with a 1.3 arcsec slit was used, providing a dispersion of 5.4 Å per pixel and a wide spectral domain ($\approx 3500 \div 10000$Å). The FORS1 exposure times range from 480 up to 6300 s; dithering of the targets along the slits was applied for the faintest objects in order to optimally remove the fringing at wavelengths longer than 7500 Å.
All the spectroscopic data have been reduced using standard IRAF routines. Bias exposures taken on each night were stacked, checked for consistency with the overscan regions of spectroscopic frames, and subtracted out. The bias–subtracted frames were then flat–fielded in a standard manner using internal lamp flats obtained during the same run. The sky background was removed by fitting a third–order polynomial along the spatial direction in source free regions. In all the observing runs the wavelength calibration was made using arc lamps (He–Ar for the EFOSC2 data, He–Ar–Hg for the FORS1 data). The flux calibration of the spectra was obtained using

observations of spectro-photometric standard stars (Oke, 1990), performed within a few hours from the object's spectroscopy.

We have obtained optical spectra of 97 of the 110 sources with optical counterparts brighter than R=24; six sources have counterparts with R between 24 and 25, still accessible to VLT spectroscopy, but demanding exposure times too long for the time allocated to our VLT run. The distributions of the X–ray and optical flux of the remaining 13 sources with optical counterpart brighter than R=24 but without optical spectroscopy is consistent with that of the sources with optical spectroscopy. Therefore the optical spectroscopic identifications can be considered representative of the HELLAS2XMM 1dF sample of sources with counterparts brighter than R=24. For 93 sources the optical spectroscopy produced reliable redshifts. In the four remaining cases the redshift determination is tentative, based on a faint, single line. The spectroscopic completeness of the HELLAS2XMM 1dF sample is $\sim 80\%$, one of the highest for hard X–ray selected sources at fluxes of $\sim 10^{-14}$ erg cm^{-2} s^{-1}.

1.4 Source breakdown

In the majority of the cases optical spectra are of sufficiently good quality to allow a reliable classification of the optical counterpart. The optical counterparts have been classified into three broad categories:

- **Broad Line AGN (AGN 1):** objects with permitted emission lines broader than 2000 km/s (FWHM);
- **Narrow Emission Line Galaxies (NELGs):** objects with permitted emission lines narrower than 2000 km/s or high-ionization state emission lines (**AGN 2**), and extragalactic sources without obvious AGN features in their optical spectra but with the presence of at least one, strong emission feature (e.g. strong [OII] or Hα emission lines, Emission Line Galaxies, **ELGs**). In six cases the presence of broad emission lines in the optical spectrum cannot be excluded, due to the insufficient quality of the spectrum and the classification of the object is therefore uncertain (see notes in Table 1.2).
- **X–ray Bright Optically Normally Galaxies (XBONG) and Early Type Galaxies (ETG)** objects without strong emission lines (equivalent width EW$< 5-8$ Å) but with stellar absorption lines and a red continuum.

The source breakdown includes: 60 AGN1 (both broad line QSO and Seyfert 1 galaxies); 17 AGN2; 12 emission line galaxies (ELGs); 5 early–type galaxies with $41.9 <$log$L_{2-10keV} < 43.0$ (XBONGs), all probably hosting an AGN; 2 Early Type Galaxies (ETG) probably associated with groups or clusters of galaxies; 1 Star.

Table 1.2 **The HELLAS2XMM 1dF sample**

Multiwavelength properties of the X–ray sources detected in the H2XMM 1dF sample

Id	X-ray Ra 2000	X-ray Dec 2000	optical RA 2000	Optical Dec 2000	Diff. arcsec	$F_{2-10keV}$ 10^{-14} cgs	R	Class.	z	$logL_{2-10keV}$ erg/s	N_H cm^{-2}	Radio flux mJy
05370037[a]	05 41 00.4	-28 39 05	–	–	–	4.93	24.0	–	–	–	–	< 2.25
05370015	05 40 54.3	-28 43 45	05 40 54.2	-28 43 47	2.4	3.19	19.9	AGN1	0.880	44.03	$0.37\pm^{1.17}_{0.37}$	< 2.25
05370022[b]	05 40 51.3	-28 36 42	05 41 51.4	-28 36 46	4.3	2.40	$\gtrsim$23.0	–	–	–	–	< 2.25
05370175	05 40 45.6	-28 39 07	05 40 45.7	-28 39 08	1.7	2.08	19.8	AGN1	1.246	44.32	$50.7\pm^{60.3}_{33.3}$	< 2.25
05370008	05 40 34.2	-28 31 08	05 40 34.2	-28 31 09	1.2	5.63	19.0	AGN2*	0.379	43.44	<0.18	< 2.25
05370021	05 40 26.1	-28 50 39	05 40 26.3	-28 50 42	4.2	3.22	23.5	ELG*	1.192	44.35	$0.16\pm^{1.50}_{0.16}$	< 2.25
05370135	05 40 24.7	-28 46 16	05 40 24.6	-28 46 16	1.3	1.21	21.3	AGN2	0.484	43.02	$1.72\pm^{2.93}_{1.44}$	< 2.25
05370043	05 40 22.1	-28 31 40	05 40 22.1	-28 31 40	0.2	3.06	22.7	AGN2	1.797	44.77	$10.5\pm^{9.4}_{4.8}$	< 2.25
05370091[c]	05 40 21.2	-28 50 38	05 40 21.1	-28 50 38	1.2	2.50	23.7	–	–	–	–	< 2.25
05370162	05 40 13.0	-28 44 02	05 40 13.0	-28 44 02	0.0	0.86	21.6	–	–	–	–	< 2.25
05370019	05 40 10.6	-28 40 51	05 40 10.5	-28 40 53	2.7	1.62	20.3	AGN1	1.330	44.15	<0.44	< 2.25
05370072	05 40 04.4	-28 38 14	–	–	–	0.83	$\gtrsim$24	–	–	–	–	< 2.25
05370159	05 40 02.7	-28 37 29	–	–	–	1.06	$\gtrsim$24	–	–	–	–	< 2.25
05370031	05 40 00.8	-28 34 56	05 40 00.8	-28 34 56	0.2	1.30	20.5	AGN1	3.276	44.96	$0.12\pm^{2.96}_{0.12}$	< 2.25
05370007	05 39 59.0	-28 37 53	05 39 59.0	-28 37 53	0.2	2.90	20.6	AGN1	0.842	43.93	<0.14	< 2.25
05370035	05 39 58.7	-28 37 07	05 39 58.7	-28 37 08	1.4	1.24	22.8	AGN1	0.897	43.65	$0.18\pm^{0.85}_{0.18}$	< 2.25
05370157	05 39 58.6	-28 41 26	–	–	–	0.77	$\gtrsim$24.5	–	–	–	–	< 2.25
0537042a	05 39 57.5	-28 49 14	05 39 57.2	-28 49 14	3.8	1.39	21.6	AGN1	1.945	44.48	$0.33\pm^{1.37}_{0.33}$	< 2.25
0537042b	05 39 58.8	-28 49 19	05 39 59.0	-28 49 19	2.0	2.10	21.5	–	–	–	–	< 2.25
05370013	05 39 57.2	-28 51 09	05 39 57.0	-28 51 08	2.6	2.54	22.0	AGN1	0.901	43.96	<0.39	< 2.25
05370017	05 39 57.0	-28 50 28	05 39 56.7	-28 50 27	3.9	2.62	20.7	AGN1	0.904	43.96	<0.28	< 2.25
05370153	05 39 56.1	-28 46 22	–	–	–	1.13	$\gtrsim$24.6	–	–	–	–	< 2.25
05370012	05 39 52.7	-28 47 09	05 39 52.8	-28 47 09	1.5	1.49	22.5	–	–	–	–	< 2.25
0537052a	05 39 50.4	-28 33 45	05 39 50.4	-28 33 45	0.4	1.11	21.5	AGN1	1.665	44.24	$0.83\pm^{1.36}_{0.83}$	< 2.25
0537052b	05 39 51.9	-28 33 45	05 39 51.8	-28 33 45	1.7	1.36	23.7	–	–	–	–	< 2.25
05370004	05 39 49.9	-28 38 32	05 39 50.0	-28 38 32	1.5	7.02	18.0	AGN1	0.894	44.39	<0.24	< 2.25
05370054[c]	05 39 45.3	-28 49 10	05 39 45.2	-28 49 10	1.3	1.62	25.0	–	–	–	–	< 2.25
05370014	05 39 43.0	-28 27 20	05 39 43.1	-28 27 19	2.0	3.00	19.6	AGN1	1.659	44.68	<1.32	257.4±7.7
05370041	05 39 39.7	-28 31 43	05 39 39.8	-28 31 42	1.9	1.56	20.4	AGN1	1.644	44.38	<0.79	< 2.25
05370078	05 39 38.7	-28 48 07	05 39 38.7	-28 48 08	1.3	1.44	22.0	AGN1	1.622	44.33	$14.2\pm^{48.4}_{10.0}$	< 2.25
05370036[d]	05 39 38.7	-28 52 49	05 39 39.2	-28 52 51	6.9	5.65	20.6	AGN1	1.329	44.71	<0.39	< 2.25
05370006	05 39 34.8	-28 41 16	05 39 34.8	-28 41 16	0.1	2.02	16.0	STAR	–	–	–	< 2.25
05370060	05 39 33.6	-28 35 19	05 39 33.7	-28 35 20	2.0	1.72	23.9	–	–	–	–	< 2.25
05370003	05 39 29.5	-28 49 00	05 39 29.4	-28 49 00	1.2	11.21	18.1	AGN1	0.317	43.55	<0.10	< 2.25
05370024	05 39 25.8	-28 44 56	05 39 25.7	-28 44 54	2.0	4.57	21.0	XBONG	0.075	41.82	<0.12	< 2.25
05370010	05 39 25.3	-28 32 37	05 39 25.4	-28 32 36	1.5	4.24	22.4	–	–	–	–	< 2.25
05370002	05 39 23.5	-28 42 24	05 39 23.5	-28 42 23	0.9	18.21	16.6	AGN1	1.244	45.14	<0.10	< 2.25
0537011a	05 39 20.5	-28 37 22	05 39 20.5	-28 37 21	0.9	4.76	23.4	AGN2[d]	0.981	44.33	$1.33\pm^{1.50}_{0.90}$	< 2.25
0537011b	05 39 21.6	-28 38 04	05 39 21.6	-28 38 06	2.5	0.88	21.7	–	–	–	–	< 2.25
05370040	05 39 20.1	-28 36 37	05 39 20.1	-28 36 38	1.1	1.54	21.0	AGN1	1.485	44.25	$0.28\pm^{1.54}_{0.28}$	< 2.25
05370164	05 39 17.2	-28 38 20	05 39 17.1	-28 38 17	3.3	1.49	23.6	AGN2	1.824	44.48	†	< 2.25
05370111[c]	05 39 11.5	-28 37 17	05 39 11.6	-28 37 15	2.4	3.69	24.5	–	–	–	–	< 2.25

Table 1.2 **The HELLAS2XMM 1dF sample - continued**

Id	X-ray Ra 2000	X-ray Dec 2000	optical RA 2000	Optical Dec 2000	Diff. arcsec	$F_{2-10keV}$ 10^{-14} cgs	R	Class.	z	$logL_{2-10keV}$ erg/s	NH cm^{-2}	Radio flux mJy
05370009	05 39 10.7	-28 35 28	05 39 10.8	-28 35 26	2.5	3.75	20.8	AGN1	0.770	43.95	$0.14\pm^{1.20}_{0.14}$	< 2.25
05370016	05 39 09.3	-28 41 05	05 39 09.4	-28 41 45	1.4	4.84	21.7	AGN2[e]	0.995	44.35	$1.32\pm^{1.56}_{0.88}$	< 2.25
05370005	05 39 05.5	-28 33 17	05 39 05.5	-28 33 16	1.2	8.94	21.1	AGN1	1.158	44.75	$0.16\pm^{0.69}_{0.16}$	< 2.25
05370123	05 38 51.4	-28 39 49	05 38 51.5	-28 39 49	1.4	7.53	23.1	AGN2*	1.153	44.72	$6.63\pm^{21.58}_{4.06}$	< 2.25
05370020	05 38 50.9	-28 37 57	05 38 50.9	-28 37 58	0.8	5.43	20.7	AGN1	0.763	44.21	<0.11	< 2.25
03120012	03 15 29.4	-76 53 42	03 15 28.8	-76 53 40	2.5	2.78	21.0	AGN1	0.507	43.49	<0.24	–
03120020	03 14 16.8	-76 56 00	03 14 16.5	-76 56 02	2.4	1.61	21.5	ELG[f]	0.964	43.87	<0.70	< 0.22
03120010	03 14 16.4	-76 45 37	03 14 16.5	-76 45 36	0.7	2.13	19.6	AGN1	0.246	42.74	<0.14	–
03120022	03 13 49.0	-76 45 59	03 13 49.3	-76 46 00	1.3	2.71	21.6	AGN1	2.140	44.85	$4.61\pm^{5.85}_{3.60}$	–
03120036[c]	03 13 43.5	-76 54 26	03 13 42.9	-76 54 24	3.2	1.45	24.6	–	–	–	–	< 0.16
03120013	03 13 34.3	-76 48 30	03 13 34.5	-76 48 30	0.9	1.17	19.7	AGN1	1.446	44.25	$0.71\pm^{2.10}_{0.71}$	< 0.36
03120003	03 13 14.7	-76 55 56	03 13 14.3	-76 55 56	1.2	16.70	18.3	AGN1	0.420	44.03	<0.03	< 0.15
03120005	03 13 12.0	-76 54 30	03 13 11.8	-76 54 31	1.4	8.37	19.1	AGN1	1.274	44.50	<0.14	< 0.17
03120127	03 12 58.0	-76 51 20	03 12 57.9	-76 51 20	0.4	1.00	23.5	AGN1	2.251	44.79	$17.2\pm^{80.0}_{15.0}$	< 0.16
03120065[b]	03 12 52.2	-77 00 59	–	–	–	1.47	$\gtrsim$24	–	–	–	–	< 0.30
03120006	03 12 54.0	-76 54 15	03 12 53.8	-76 54 15	0.7	8.28	22.0	AGN2	0.680	44.16	<0.16	< 0.15
03120018	03 12 39.3	-76 51 33	03 12 38.7	-76 51 33	1.9	2.59	18.0	XBONG	0.159	42.24	$0.46\pm^{0.84}_{0.46}$	< 0.15
03120008[a,l]	03 12 31.2	-76 43 24	03 12 31.3	-76 43 25	1.1	1.64	13.7	ETG/GROUP	0.052	41.08	$0.15\pm^{0.45}_{0.15}$	–
03120004	03 12 09.2	-76 52 13	03 12 09.2	-76 52 13	0.1	6.49	18.2	AGN1	0.890	44.49	<0.08	< 0.22
03120016	03 12 00.4	-77 00 26	03 12 00.5	-77 00 26	0.6	1.51	22.2	AGN2*	0.841	43.79	$35.5\pm^{43.1}_{21.6}$	6.54±0.50
0312089a	03 11 45.0	-76 56 45	03 11 44.4	-76 56 46	2.3	1.30	23.6	ELG	0.809	43.56	$3.05\pm^{7.34}_{2.89}$	< 0.15
03120181	03 11 36.0	-76 55 56	03 11 36.0	-76 56 00	3.8	1.10	23.2	ELG	0.709	43.49	$24.6\pm^{40.2}_{20.3}$	0.23±0.05
03120035[h]	03 11 31.8	-77 00 36	03 11 31.8	-77 00 32	4.3	1.83	22.0	AGN1	1.272	44.16	$0.23\pm^{2.15}_{0.23}$	0.36±0.07
03120066	03 11 28.2	-76 45 16	03 11 29.2	-76 45 15	3.7	1.51	23.1	AGN1[d]	1.449	44.23	<1.76	–
03120017	03 11 24.8	-77 01 39	03 11 25.4	-77 01 35	4.6	2.74	17.7	XBONG	0.320	42.93	$0.13\pm^{0.45}_{0.13}$	1.30±0.09
03120031[c]	03 11 13.9	-76 53 59	03 11 13.6	-76 54 00	1.0	1.20	23.6	–	–	–	–	< 0.15
03120029	03 11 13.4	-76 54 31	03 11 13.0	-76 54 34	3.1	1.21	18.8	–	–	–	–	< 0.15
03120011	03 11 12.8	-76 47 02	03 11 13.3	-76 47 02	1.9	1.56	21.5	AGN1	0.753	43.72	<0.24	< 0.37
03120009	03 11 05.6	-76 51 58	03 11 05.3	-76 51 58	0.9	1.98	23.2	AGN1	1.522	44.45	<0.84	< 0.15
03120007	03 10 50.0	-76 39 04	03 10 50.2	-76 39 04	0.8	29.20	18.6	AGN1	0.381	44.12	$0.12\pm^{0.24}_{0.12}$	–
03120021	03 10 49.8	-76 53 17	03 10 49.7	-76 53 16	0.7	1.51	22.3	AGN1	2.736	44.85	<4.19	< 0.15
03120028	03 10 37.4	-76 47 13	03 10 37.9	-76 47 11	2.5	1.78	20.8	ELG	0.641	43.43	$0.54\pm^{2.70}_{0.54}$	< 0.37
03120045[c]	03 10 19.0	-76 59 58	03 10 18.9	-76 59 58	0.5	1.94	24.4	–	–	–	–	< 0.17
03120002	03 10 15.8	-76 51 33	03 10 15.9	-76 51 33	0.5	41.70	17.6	AGN1	1.187	45.50	<0.05	9.28±0.07
03120124	03 10 01.6	-76 51 07	03 10 01.7	-76 51 08	1.3	1.41	22.5	–	–	–	–	< 0.30
03120501	03 09 52.2	-76 49 27	03 09 51.0	-76 49 23	5.9	1.36	20.0	XBONG	0.205	42.22	†	< 0.28
03120014	03 09 51.2	-76 58 25	03 09 51.4	-76 58 26	1.5	3.97	18.4	ELG	0.206	42.66	<0.26	< 0.15
03120024	03 09 31.7	-76 48 45	03 09 32.1	-76 48 46	1.8	1.76	21.8	AGN1	1.838	44.58	<3.36	< 0.55
03120116	03 09 18.5	-76 57 59	03 09 18.2	-76 58 00	1.1	2.01	23.9	ELG	0.814[i]	43.87	†	< 0.18
03120034	03 09 12.1	-76 58 26	03 09 12.1	-76 58 26	0.2	9.80	19.1	AGN2	0.265	43.34	$4.33\pm^{1.81}_{1.35}$	< 0.22
26900038	23 59 57.2	-25 05 43	23 59 57.2	-25 05 44	1.4	2.25	21.0	ELG	0.904	43.93	$4.96\pm^{3.42}_{1.96}$	0.95±0.04
26900075[c]	23 59 56.6	-25 10 20	23 59 56.4	-25 10 18	3.3	2.06	24.6	–	–	–	–	< 0.14
26900039	23 59 39.8	-25 00 57	23 59 39.8	-25 00 57	0.2	3.90	19.6	AGN1	0.930	44.20	$6.35\pm^{3.95}_{2.54}$	< 0.17
26900028	23 59 33.4	-25 07 58	23 59 33.3	-25 07 57	2.0	3.30	21.8	AGN1	0.738	43.88	<0.33	< 0.17
26900006	00 01 22.8	-25 00 19	00 01 22.7	-25 00 19	1.4	12.20	18.7	AGN1	0.964	44.68	<0.09	7.98 ±0.06

Table 1.2 **The HELLAS2XMM 1dF sample - continued**

Id	X-ray Ra 2000	X-ray Dec 2000	optical RA 2000	Optical Dec 2000	Diff. arcsec	$F_{2-10keV}$ 10^{-14} cgs	R	Class.	z	$\log L_{2-10keV}$ erg/s	NH cm^-2	Radio flux mJy
26900029[c]	00 01 11.6	-25 12 03	00 01 11.5	-25 12 6	3.9	3.56	25.1	–	–	–	–	0.17±0.05
26900010	00 01 06.8	-25 08 46	00 01 06.8	-25 08 47	1.4	3.08	21.0	AGN1	1.355	44.47	<0.38	< 0.15
26900003	00 01 02.4	-24 58 47	00 01 02.4	-24 58 49	1.7	11.16	20.3	AGN1	0.433	43.85	<0.08	< 0.18
26900002	00 01 00.2	-25 04 59	00 00 59.9	-25 05 00	4.2	14.35	21.9	AGN1	0.850	44.66	$0.54\pm^{0.29}_{0.30}$	94.04±0.04
26900014	00 00 44.3	-25 07 38	00 00 44.3	-25 07 40	2.2	1.63	21.6	–	–	–	–	< 0.12
26900022	00 00 36.6	-25 01 05	00 00 36.6	-25 01 06	1.0	3.14	21.2	AGN2	0.592	43.64	$1.05\pm^{0.69}_{0.50}$	< 0.13
26900007	00 00 34.6	-25 06 19	00 00 34.6	-25 06 21	1.7	1.68	20.3	AGN1	1.234	44.22	<0.29	0.20±0.04
26900004	00 00 31.7	-24 54 59	00 00 31.9	-24 54 57	3.6	7.96	17.7	AGN1	0.284	43.35	<0.05	< 0.18
26900013[l]	00 00 30.1	-25 12 14	00 00 29.8	-25 12 17	4.9	1.63	17.5	ETG/GROUP	0.154	42.07	†	< 0.13
26900001	00 00 27.7	-25 04 41	00 00 27.7	-25 04 43	1.6	7.81	19.1	AGN1	0.336	43.43	<0.06	< 0.12
26900012	00 00 26.0	-25 06 48	00 00 26.0	-25 06 51	2.5	1.70	20.3	AGN1	0.433	43.03	$0.14\pm^{0.27}_{0.14}$	0.11±0.04
26900015	00 00 22.8	-25 12 20	00 00 22.9	-25 12 22	2.2	1.74	19.7	AGN1	1.610	44.40	$1.52\pm^{2.47}_{1.27}$	< 0.14
26900009	00 00 21.2	-25 08 13	00 00 21.2	-25 08 12	1.4	2.16	20.9	AGN1	0.995	44.00	$0.14\pm^{0.43}_{0.14}$	< 0.11
26900072	00 00 13.7	-25 20 11	00 00 13.6	-25 20 13	2.1	4.05	23.0	ELG	1.389[i]	45.37	$59.3\pm^{77.7}_{49.5}$	< 0.15
26900016	00 00 02.8	-25 11 38	00 00 02.7	-25 11 37	1.5	2.75	21.0	AGN1	1.314	44.37	$0.34\pm^{0.72}_{0.34}$	< 0.13
15800002	00 34 19.1	-11 59 37	00 34 19.0	-11 59 39	2.3	9.64	20.2	AGN1	0.848	44.49	<0.13	< 0.16
15800012	00 34 18.5	-12 08 09	00 34 18.5	-12 08 09	0.5	6.79	18.8	AGN2	0.233	43.04	$1.63\pm^{0.74}_{0.54}$	< 0.16
15800011	00 34 15.4	-12 08 47	00 34 15.5	-12 08 45	2.9	1.84	20.7	AGN1	2.069	44.69	<0.50	< 0.14
15800062	00 34 13.9	-11 56 00	00 34 13.8	-11 56 00	1.1	4.49	23.3	AGN2	1.568	44.80	$26.3\pm^{44.7}_{18.1}$	< 0.16
15800025	00 34 10.0	-12 11 26	00 34 09.9	-12 11 32	5.8	2.56	21.0	ELG	0.470	43.37	$0.29\pm^{0.61}_{0.28}$	< 0.14
15800019	00 33 57.3	-12 00 40	00 33 57.2	-12 00 38	1.9	3.12	21.8	AGN2[d]	1.957	44.84	$7.26\pm^{11.67}_{5.45}$	< 0.13
15800008	00 33 47.5	-12 03 25	00 33 47.5	-12 03 26	1.5	2.58	21.0	AGN1	1.151	44.22	<1.42	< 0.12
15800092	00 33 42.5	-12 01 34	00 33 42.7	-12 01 37	4.6	2.65	22.8	ELG[d]	0.993	44.16	$16.8\pm^{16.0}_{9.0}$	0.13±0.04
15800013	00 33 39.6	-12 08 26	00 33 39.6	-12 08 28	2.0	1.82	22.3	ELG	1.326[i]	44.20	$1.92\pm^{2.12}_{1.13}$	< 0.13
15800005	00 33 24.1	-12 06 51	00 33 24.1	-12 06 49	2.5	2.35	20.2	AGN1	1.207	44.30	<0.13	< 0.11
15800017	00 33 20.6	-12 05 40	00 33 20.6	-12 05 38	1.3	2.83	20.3	AGN1	1.946	44.79	<0.61	< 0.11
15800001	00 33 15.7	-12 06 57	00 33 15.7	-12 06 59	1.8	7.29	19.9	AGN1	1.211	44.79	<0.31	< 0.12
50900036	20 44 46.4	-10 38 40	20 44 46.7	-10 38 43	5.4	3.30	20.2	AGN2	0.694	43.84	<0.97	279.0±7.5
50900001	20 44 28.7	-10 56 29	20 44 28.4	-10 56 33	5.6	4.97	23.9	AGN2[d]	1.049	44.40	<1.14	< 2.25
50900061	20 44 20.5	-10 49 04	20 44 20.5	-10 49 03	1.6	4.22	20.4	XBONG	0.324[i]	43.16	$0.47\pm^{0.45}_{0.26}$	< 2.25
50900020	20 44 19.4	-10 56 20	20 44 19.5	-10 56 19	1.6	7.58	20.2	AGN1	0.770	44.30	$0.48\pm^{1.53}_{0.48}$	< 2.25
50900067	20 44 07.1	-10 56 11	20 44 07.2	-10 56 12	1.5	5.29	22.3	AGN1	1.076	44.44	<0.57	< 2.25
50900013	20 43 49.7	-10 32 44	20 43 49.5	-10 32 40	5.0	4.42	23.2	AGN2	1.261	44.55	$2.52\pm^{4.58}_{2.15}$	< 2.25
50900031	20 43 49.2	-10 37 46	20 43 49.1	-10 37 43	3.0	6.13	20.6	AGN1	0.556	43.82	<0.10	< 2.25
50900039	20 43 22.8	-10 40 30	20 43 22.5	-10 40 31	4.7	5.19	22.4	AGN1[d]	0.818	44.17	<0.83	< 2.25

NOTES on single objects: [a] Group of galaxies in the error-box; [b] Nearby bright star; [c] Aperture photometry at the position of a bright K source (Mignoli et al. 2004); [d] Classification tentative; [e] Two nearby objects, a type 2 AGN and an emission line galaxy, at the same redshift; [f] Two nearby emission line galaxies at the same redshift; [g] Emission from a group or cluster of galaxies, redshift based on nearest galaxy; [h] Two possible counterparts, a type 1 AGN and an R-K$\gtrsim$ 6.1 radio source (Brusa et al. 2003); [i] redshift tentative, based on a single faint emission line. [l] Extended emission, redshift based on a bright early–type galaxy; † N_H unconstrained (see Perola et el. 2004; Puccetti, PhD thesis)

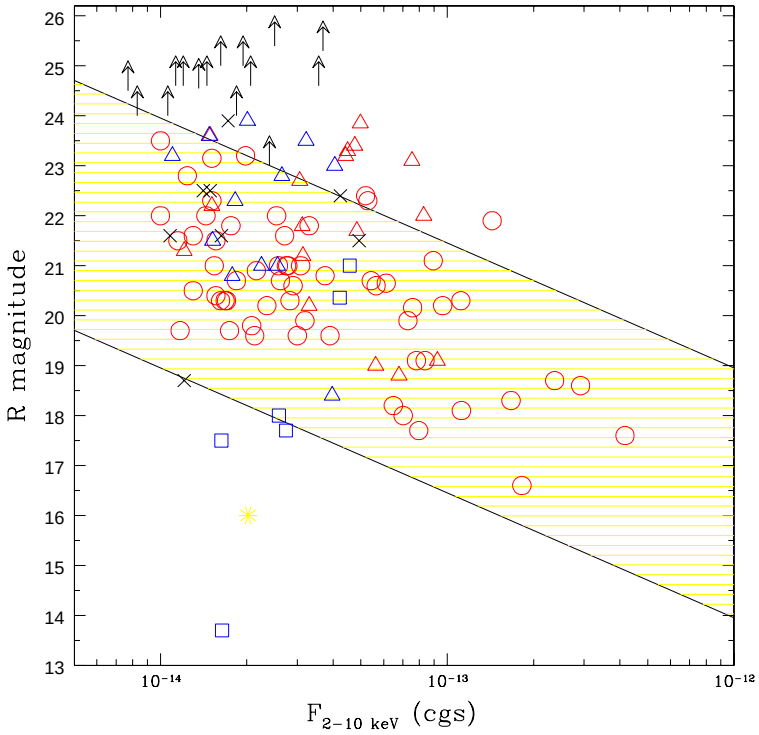

Figure 1.9 The optical (R band) magnitude versus the X–ray (2-10 keV) flux for the HELLAS2XMM 1dF sample. Different symbols identify different source classes: open cyrcles = broad line AGNs (AGN1); open triangles = narrow line AGNs (AGN2 and ELG); open squares = early-type galaxies (XBONG); crosses and arrows= spectroscopically unidentified sources. The dotted lines indicate the loci of constant X–ray-to-optical flux ratio, delimiting the region of "classic" AGNs ($-1 < log(X/O) < 1$).

In summary, 94 of the 97 sources with optical spectroscopy are associated with AGN emission, the majority (60/97, 63%) are Type 1 AGN. The optical spectra of all the 97 X–ray sources are available at the link: http://stars.bo.astro.it/ marfield/HELLAS2XMM/sample.html.

Table 1.2 gives for each source the Xid (col. 1), the X–ray position (cols. 2-3), the position of the optical counterpart (cols 4-5), the displacement between the X–ray and optical positions (col. 6), the 2–10 keV flux (col. 7), the R–band magnitude of the optical counterpart or the three σ upper limit (col. 8), the optical classification and redshift from the spectrum (cols. 9-10), the unabsorbed hard X–ray luminosity and the intrinsic X–ray column density (cols. 11-12), and the radio flux (col 13).
Classifications are as described above; radio fluxes or upper limits are at 1.4 GHz for the PKS 0537 (NVSS, 5σ), A2690 (VLA, 3σ), G158 (VLA, 3σ) and MKN509 (NVSS, 5σ) fields; for the PKS0312 field the fluxes have been obtained at 5 GHz (ATCA) and the upper limits are given at the 3σ level (see Sect. 1.1.4 for details of the observations).

In Fig. 1.9, the already discussed R–band magnitude vs. 2–10 kev flux plane is shown for the sources in the HELLAS2XMM 1dF sample in the same Figure is highlighted the the well–defined correlation between the X–ray flux and optical magnitude around $< lg(F_{\rm x}/F_{\rm R}) >= 0 \pm 1$ observed for optically and soft X–ray selected quasars (see Introduction).
In the following I will investigate in more details the nature and properties of the sources located in different regions of this plane.

Chapter 2

Optical appearance of hard X–ray sources

The presence of X–ray activity is generally witnessed by strong emission lines in the optical spectra, and viceversa.
Moreover, in their simplest version (e.g., Antonucci 1993), AGN unification models predict a one–to–one relation between optical Type 1 and X–ray unobscured sources, and between optical Type 2 and X–ray obscured sources. However, recent multiwavelength programs of follow–up observations of hard X–ray selected sources have started to reveal a complex nature for the hard X–ray source population and have already pointed out several hints for a departure from this simple scheme (Barger et al. 2002; Willott et al. 2003; Akiyama et al. 2001; Fiore et al. 2001; Maiolino et al. 2003; see Comastri 2004 and reference therein).
The multiwavelength coverage of our survey and the high spectroscopic completeness ($\sim 80\%$) allows us to investigate the large spread in the overall optical to X–ray properties of hard X–ray selected sources in much more details.
In the following I will discuss the observed optical to X–ray properties of the sources in the `HELLAS2XMM 1dF` sample for which spectroscopic redshifts and optical classifications are available and the *intrinsic* X–ray column densities have been derived from proper X–ray spectral analysis (see Perola et al. 2004; Puccetti PhD Thesis).
In particular, I will focus the discussion on two classes of objects (X–ray absorbed BL AGN and XBONG, see Next Sects.) that seem to suggest the necessity for (substantial) revision of the classic Unified schemes.

2.1 Broad–Line AGN

The 60 objects with broad emission lines in the optical spectrum have an average X–ray–to–optical flux ratio $< lg(F_{\rm x}/F_{\rm R}) >$=0.17 with a dispersion of 0.45 (see Fig. 1.9) which is typical of soft X–ray selected Type 1 AGN

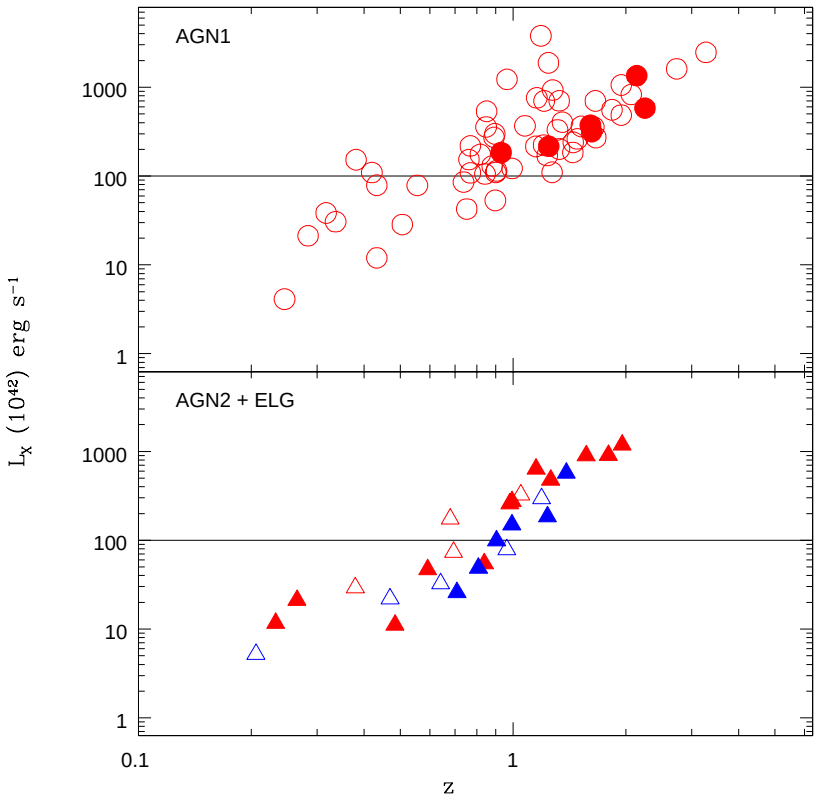

Figure 2.1 The luminosity–redshift plane for the BL AGN (upper panel) and the NL AGN and ELG (lower panel). Empty symbols mark unabsorbed sources, filled symbols mark mark objects with X–ray column densities $> 10^{22}$ cm^{-2}. X–ray luminosities are corrected for absorption. High(Low)–luminosity objects lie above(below) the dashed line at $L_X = 10^{44}$ erg s^{-1}.

(Lehmann et al. 2001).

The redshift, luminosities and rest–frame column densities are listed in the last three columns of Table 1.2. While a population of BL AGNs with an *unobscured* X–ray spectrum is present at all redshifts and spans a wide range in luminosities, some examples of *X–ray obscured*, BL AGNs are present at high redshifts and X–ray luminosities (see upper panel of Fig. 2.1): in the HELLAS2XMM 1dF sample one finds six out of sixty optically classified BL AGN, whose best fit logN_H is greater than 22 and for two objects the absorbing column is greater than 10^{23} at the 90% confidence level. In these cases the spectroscopic classification turns out opposite to the X–ray classification, when the latter is based on the X–ray obscuration.
The 10% fraction (6/60) is in agreement with the finding (3/29) by Page et al. (2003). It is worth stressing that the 6 X–ray absorbed BL AGN have $L_{2-10keV} > 10^{44}$ erg s^{-1}, while all the BL AGN with $L_{2-10keV} < 10^{44}$, i.e. the Seyfert 1 objects, have log(N_H)<22.

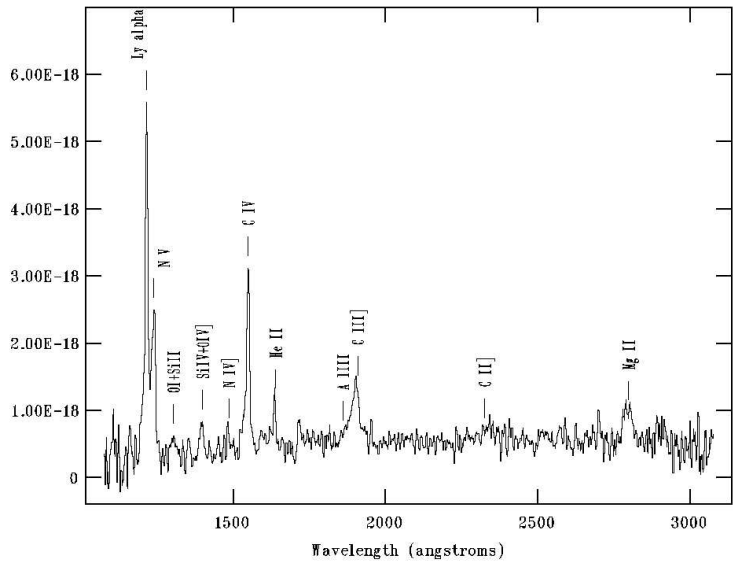

Figure 2.2 The optical spectrum of a X–ray absorbed, BL AGN/ERO at z=2.251 (source 03120127), discussed in Sect. 2.1.

A very interesting object is the highly absorbed ($N_H \sim 10^{23}$ cm^{-2}) source 03120127 identified with a broad—line quasar at z=2.251 on the basis of the MgII and CIII] lines (see Fig. 2.2). The other emission lines are narrow (FWHM<2000 km s^{-1}) and the underlying continuum is very red if compared to that of optically selected BL AGNs (e.g., Brotherton et al. 2001). For this source additional K–band imaging is available; the EFOSC2/R–band and VLT/K–band images are shown in Fig. 1.4. The optical counterpart is associated with a bright near–infrared source (K= 18.4) having an optical to near–infrared color of R-K=5.1, considerably redder than that of high–redshift quasars (R-K$\sim$ 2), suggesting a dominant contribution from the host galaxy.

As far as the multiwavelength properties (continuum shape, luminosity, hard X–ray spectrum, and upper limit on the radio emission) are concerned, this object is very similar to source N2_25 in the ELAIS survey (Willott et al. 2003) which is indeed classified as a reddened quasar at high redshift.

2.2 Narrow Emission Line Objects

Twenty–nine objects with narrow emission lines have been found. On the basis of their optical lines ratios and intensities, 17 are classified as Type 2 AGN (AGN2) while for the remaining 12 we cannot provide a secure classification (mostly because only one emission line is present in the spectral

range) and we refer to them as Emission–Line Galaxies (ELGs).

Both AGN2 and ELG are reported in the bottom panel of Fig. 2.1, with different colours. All of these sources span the same redshift and luminosities ranges of AGN1. Moreover, about half of the objects lie above the threshold of X–ray luminosity $> 10^{44}$ erg s^{-1} and can be therefore classified as QSO2. It is also worth noticing that all but one of the ELGs have X–ray luminosities larger than 2×10^{43} erg s^{-1} (Fig. 2.1), typical of Seyfert 2 galaxies, strongly suggesting the presence of an active nucleus even in the objects where a more accurate optical classification is not possible.

In the context of AGN unified schemes, Type 2 AGN are expected to be intrinsically absorbed sources. The average X–ray–to–optical flux ratio of AGN 2 and ELG in the present sample is $< lg(F_{\rm x}/F_{\rm R}) >$=0.67 with a dispersion of 0.62 (see Fig. 1.9) which is considerably larger than the average value observed for AGN1. This is a first indication that the active nucleus is obscured both at X–ray and optical frequencies (for a more detailed discussion see Sect. 4). The absorbing column densities estimated from the X–ray spectral analysis are generally as expected (larger than 10^{22} cm^{-2} at the 90% confidence level, filled symbols in Fig. 2.1), confirming that the majority of the sources are X–ray obscured. However, one also finds four objects classified as AGN2 with $N_H < 10^{22}$ cm^{-2}. Here the most probably origin of the discrepancy is the complexity of the X–ray spectra, which is found in detailed studies of bright sources (e.g. Turner et al. 2000).
Similar examples of "unabsorbed Type 2" AGN have been reported by Panessa & Bassani (2002) and Pappa et al. (2002).

2.3 X–ray Bright Optically Normal galaxies (XBONG)

Among the 122 sources in the H2Xmm 1dF sample (see Table 1.2), seven objects ($\sim$ 6%) have been optically identified as "absorption line galaxies": three in the PKS 0312 field (03120018, 03120017, 03120008 and 03120501); one in A2690 field (26900013); one in the PKS 0537 field (05370024); one in the MKN 509 field (50900061).
These findings are in agreement with the results from both *Chandra* and XMM–*Newton* surveys that have reveled a population of X–ray emitting sources associated with the nuclei of galaxies without any obvious signature of AGN activity in their optical spectra (Mushotzky et al. 2000, Fiore et al. 2000, Barger et al. 2001, Giacconi et al. 2001, Hornschmeier et al. 2001; Comastri et al. 2001a,b; Severgnini et al. 2003; Georgakakis et al. 2004). The unprecedent arcsec *Chandra* spatial resolution has unambiguously demonstrated that such a population of X–ray Bright Optically Normal Galaxies (hereinafter XBONG, Comastri et al. 2002a) is associated to luminous X–ray sources, confirming previous claims at bright X–ray fluxes based on lower spatial resolution *Einstein* and ROSAT observations (Elvis et al. 1981,

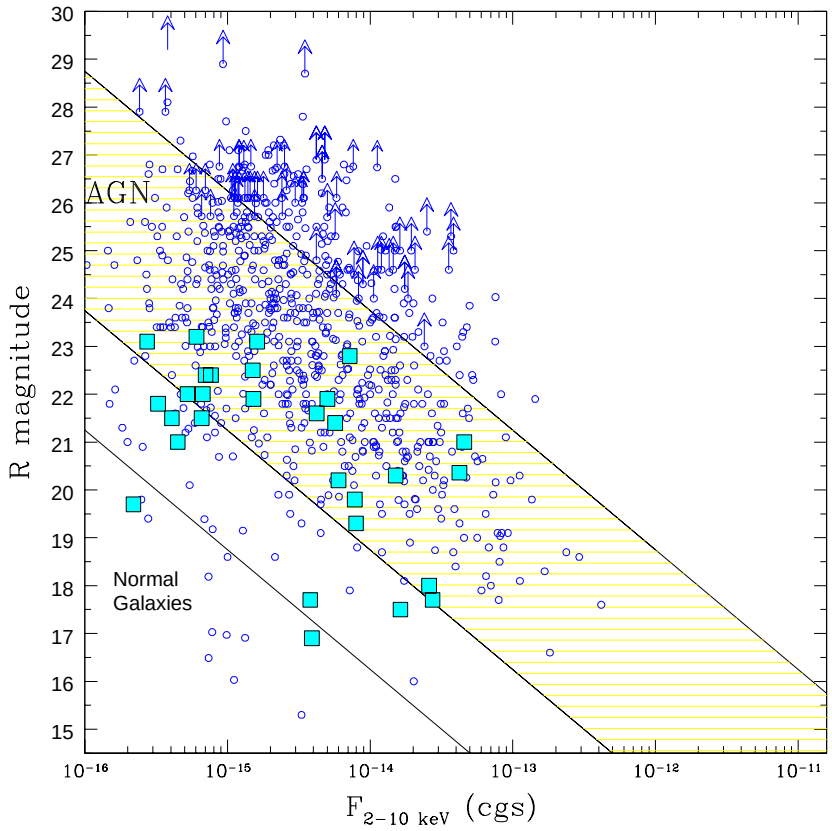

Figure 2.3 The 2–10 keV X–ray flux versus the R magnitude for a sample of hard X–ray selected sources from the HELLAS2XMM 1dF survey and other *Chandra* and XMM–*Newton* surveys (Barger et al. 2001a,b; Mainieri et al. 2002; Barger et al. 2002). The cyan squares correspond to "bona fide" XBONG, while the blue circles are other classes of AGN. The locii of AGN (shaded area at $-1 < log(X/O) < 1$) and normal galaxies (at $log(X/O) < -2$) are also highlighted.

Griffiths et al. 1995).

The XBONG X–ray luminosities span the range 10^{41}–10^{43} erg s^{-1} and are therefore in between those of AGN ($\gtrsim 10^{42}$ erg s^{-1}) and those expected for normal galaxies on the basis of the L_X–L_B correlation of early-type galaxies ($\sim 10^{40-41}$ erg s^{-1}, Fabbiano, Kim, & Trinchieri, 1992). This can be seen in terms of X–ray to optical flux ratio (Fig. 2.3): the average value of the XBONG is $< lg(F_{\rm x}/F_{\rm R}) >\sim -1$, while the typical value for AGN is $lg(F_{\rm x}/F_{\rm R}) \sim 0$ (see Introduction) and normal galaxies generally show $lg(F_{\rm x}/F_{\rm R}) \lesssim -2$. Although a few XBONG could be luminous examples of otherwise normal elliptical galaxies whose X–ray emission arise from the integrated contribution of stellar sources, such a possibility is clearly inconsistent with the majority of the objects An alternative understanding and characterization of the sources powering XBONG can be achieved by means of extensive follow–up observations.

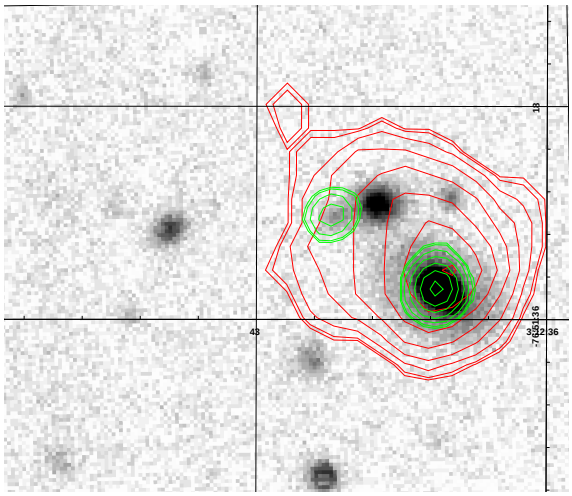

Figure 2.4 The *Chandra* (green/light grey) and XMM–*Newton* (red/black) contours of P3 overlayed on the EFOSC R band image

2.3.1 The prototype of XBONG: P3 galaxy

The first object optically identified with a normal, early–type galaxy for which a detailed multiwavelength study has been performed is source 03120018. This object was originally discovered by *Chandra* (CXOUJ 031238.9–765134 in Fiore et al. 2000) and it is usually known as P3, being the third source catalogued in the field containing the quasar PKS 0312–77. A detailed description of data reduction and analysis procedures is extensively reported in Comastri et al. (2002b). I will summarize the most important results based on the broad–band spectral energy distribution from radio to X–rays.

- X–rays

  Source P3 was detected both by *Chandra* and XMM–*Newton*. A good description of the X–ray spectrum is obtained fixing the power-law slope at Γ=1.9 (the average value for the sources in our sample, see Perola et al. 2004); this gives an upper limit on absorption column density at the source frame of $N_H < 1.3 \times 10^{22}$ cm^{-2},consistent with the value reported in Comastri et al. (2002b). The absorption-corrected 2–10 keV luminosity is about 3 $\times 10^{42}$ erg s^{-1}. The good agreement between the power-law slope and the hard X–ray flux measured by *Chandra* and XMM–*Newton* suggests that the maximum fractional variability is of the order of 30% on a time scale of about 7 months.

- Optical and Near–infrared spectra

  Optical spectra and imaging have been obtained with the ESO 3.6m telescope. The magnitudes in the R and B bands are 18.0 and 19.7, respectively. The average redshift is $z = 0.1595 \pm 0.0007$, measured from the position of the principal absorption lines and comparison with an early–galaxy template.

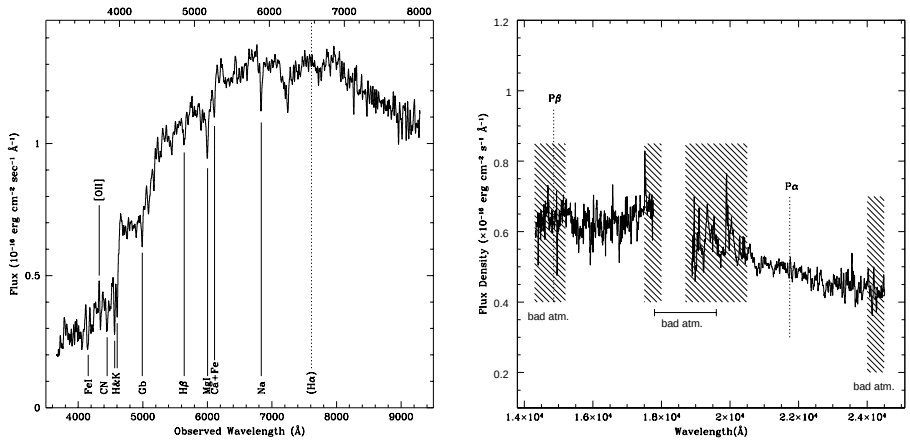

Figure 2.5 (*Left panel*): The flux calibrated optical spectrum of P3. The spectral features are indicated with solid lines, while the dotted line is at the wavelength corresponding to Hα. (*Right panel*): The VLT ISAAC infrared spectrum of P3. The shaded regions correspond to wavelengths of bad atmospheric transmissions. The expected positions of Pα and Pβ lines are also indicated. [From Comastri et al. 2002b].

Near–infrared spectra in the SH (1.42-1.83 μm) and SK (1.84-2.56 μm) filters have been obtained at the ESO/VLT with ISAAC. The corresponding H and Ks magnitudes are 15.7 and 14.9, respectively. Additional imaging observations in the L (3.8–5 μm) band have been performed with the ISAAC camera. The source is not detected at the limiting magnitude of 13.4 (3σ upper limit).

- Radio
  The object remains undetected at the limit of the ATCA observations and only an upper limit on the radio emission at 5 GHz has been obtained ($S_{5\mathrm{GHz}} < 0.15$ mJy).

The XMM–*Newton* and *Chandra* contours are overlaid on a R band optical image in Fig. 2.4. It can be seen that the elongated XMM–*Newton* contours are probably due to the presence of a faint X–ray source which is clearly resolved by *Chandra* at a distance of $\sim$6″ from P3. This object appears to be coincident with an extremely faint R $>$ 24 optical counterpart. Its X–ray flux is only about 10–15 % of P3, while its hardness ratio suggests a spectral shape similar to P3.

In the left panel of Fig. 2.5 the optical spectrum is shown with the principal identified absorption lines labelled. Also plotted are the emission line [OII] at 3727 Å and the expected position of the Hα features. Unfortunately, at the redshift of P3 the Hα line position coincides with the stronger atmospheric telluric band in the optical. In the right panel of Fig. 2.5 the near–infrared spectrum is shown.

2.3.2 What's going on in the nucleus of P3 ?

The broad band observations discussed above are shown in a ν vs νF_ν plot in the left panel of Fig. 2.6.
At the first sight, the overall spectral energy distribution (hereinafter SED) is clearly dominated by the optical–infrared light of the host galaxy. However, the relatively high X–ray luminosity and the X–ray spectral properties strongly suggest nuclear activity in the central regions of P3. Based on the *Chandra* detection and the optical spectrum, Fiore et al. (2000) suggested three different possibilities, namely: 1) a radiatively inefficient advection dominated accretion flow (ADAF) 2) a BL LAC object, and 3) a completely obscured AGN.
Moreover, the featureless optical spectrum can be also explained if the nuclear light from an AGN is over-shined by the stellar continuum of a relatively bright host galaxy. In the following I will discuss these possibilities in more details.

ADAF models The observed fluxes in the radio and X–ray bands have been compared with the model spectra of Quataert & Narayan (1999) for several values of the physical parameters involved in the ADAF models with winds as most of the bolometric luminosity predicted by these models is produced in the hard X–ray and radio bands. For the range of model parameters computed by Quataert & Narayan (1999) the X–ray flux density is about 1–2 order of magnitude greater than the radio flux density (see their Fig. 7). Although the hard X–ray spectrum is consistent with the flat power law slope expected by (some) ADAF models (see Di Matteo et al. 2000), the model predicted radio flux is in excess of the present upper limit: the observed lower limit on the X–ray to radio flux density of P3 ($> 10^3$) is clearly inconsistent with ADAF model predictions.

LLAGN The observed SED is consistent with an early-type galaxy template normalized to match the optical and infrared spectrum plus the average SED of radio–quiet AGN (Elvis et al. 1994) rescaled to the observed X–ray flux (Fig. 2.6, right panel). In this case the optical AGN emission lines are diluted by the host galaxy starlight. We note that the average SED of radio quiet quasars has been obtained from a sample of high-luminosity quasars and thus is unlikely to be appropriate for low-luminosity AGN (hereinafter LLAGN) which are known to be characterized by a quite different broad-band spectrum (Ho 1999). In particular, low-luminosity objects lack an ultraviolet excess and have a more pronounced contribution from X–rays to the overall energy output. Prompted by the similarities between LLAGN and the P3 multiwavelength data, the broad-band SED of the four LLAGN hosted by an elliptical galaxy in the Ho (1999) sample have been compared with that of P3 and normalized to the observed X–ray flux (see Fig. 2.7, left panel). Although the comparison sample is very small, we note that the average flux in the radio band of low-luminosity AGN greatly exceeds the observed upper limit. The general trend of increasing X–ray variability for decreasing X–ray

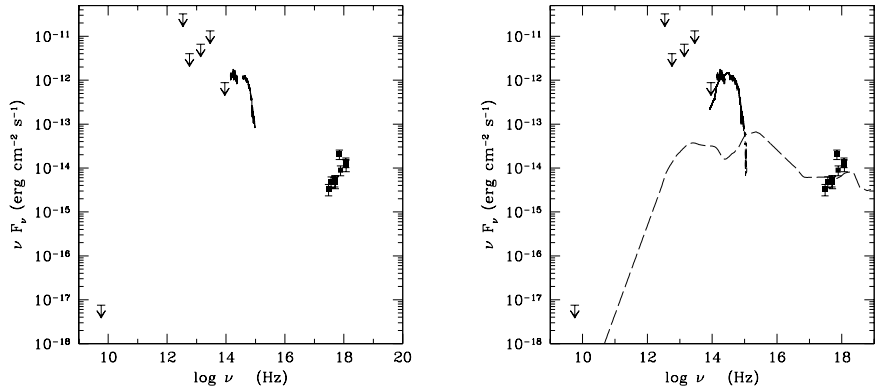

Figure 2.6 (*Left panel*): The broad-band spectral energy distribution of P3, including the upper limits in the 12μ, 25μ, 60μ and 100μ IRAS bands (retrieved from the NED database). (*Right panel*): The radio to X–ray spectral energy distribution of P3 is compared with the average SED of a radio–quiet AGN (long dashed line) plus an early-type galaxy template (solid line).

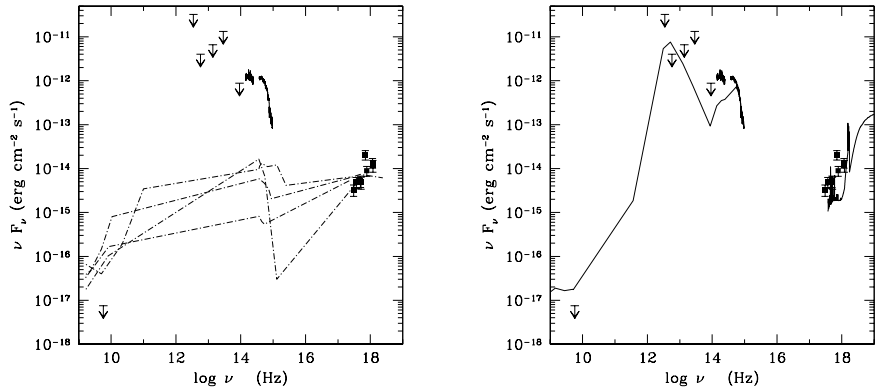

Figure 2.7 (*Left panel*): the SED of the four low-luminosity AGN in the Ho (1999) sample (dot–dashed lines) hosted by an E–galaxy (NGC 6251, NGC 4261, M84 and M87) normalized to the P3 X–ray flux. (*Right panel*): The observed SED is compared with that of the highly obscured Seyfert 2 galaxy NGC 6240 (Vignati et al. 1999).

luminosities (Nandra et al. 1997) would also be inconsistent with the lack of strong X–ray variability.

BL LAC objects The BL Lac hypothesis might be tenable despite the presence of a large Calcium break and the low radio flux density. Indeed, there is increasing evidence that the Blazars SED can be unified in a spectral sequence determined from the total luminosity (Fossati et al. 1998, Ghisellini et al. 1998). The objects populating the low–luminosity extreme of the

sequence are called HBL (High peak BL Lacs) as their SED peak at relatively high frequency (typically in the X–rays) when compared to that of other blazars. The upper limit on the 5 GHz radio luminosity density ($< 10^{39}$ erg s^{-1}), on the radio to X–ray spectral index ($\alpha_{rx} < 0.6$) and the flat slope in the X–ray band would be consistent with the presence of a rather extreme member of the HBL class hosted by P3. The lack of X–ray variability, however, may constitute a problem with this interpretation.

Compton Thick AGN An alternative explanation would be the presence of an hidden, obscured AGN. In order to test whether this is the case for P3 we have compared the observed SED with that of NGC 6240, a highly obscured, Compton Thick AGN (Vignati et al. 1999). The AGN SED is normalized to match the P3 optical flux (Fig. 2.7, right panel). Besides the disagreement at long wavelengths, which can be due to a more intense star–formation in NGC 6240, the P3 multiwavelength data are in relatively good agreement with the obscured AGN template. If P3 hosts a Compton thick AGN with a SED similar to that of NGC 6240 then a luminous ($\sim$ of 10^{44} erg s^{-1}) X–ray source should be present at higher energies. In this case the observed X–ray emission would be due to a scattered nuclear component known to be common among highly obscured AGN (Vignali et al. 2001 and references therein). The lack of strong X–ray variability would support this hypothesis.

2.3.3 Other XBONG in the HELLAS2XMM survey

Two sources (03120008 and 26900013) are more extended than the XMM-*Newton*/EPIC PSF at their off-axis angles (Ghizzardi 2001).
In particular, 03120008 is the softest source in the HELLAS2XMM 1dF sample (HR=-0.72, source 8 in Table 1.1), and is also characterized by the lowest X–ray–to–optical flux ratio ($lg(F_{\rm x}/F_{\rm R}) \sim -2.5$). Deep R–band image revealed a complex morphology: the peak of the X–ray emission is almost coincident with the brightest nucleus of an interacting system at z$\sim$0.05 containing at least three nuclei in a common envelope (Fig. 2.8, left panel). The total R–band magnitude of the system is R=13.7. The optical spectra of the three nuclei are very similar, showing an absorption–line spectrum typical of early–type galaxies, without any emission line except for a weak Hα in the faintest one (Fig. 2.8, right panel). Both the optical and X–ray data favour thermal emission due to intracluster or intragroup hot, optically thin, plasma. Unfortunately, the source lies at the edge of the ACIS–I field in the *Chandra* observation, leaving the issue of wheter the X–ray emission is associated to the whole group unsettled.
As already pointed out, XBONG could be the host galaxies of BL Lac objects; if this were the case, deep radio observations would be the most useful tool to test this possibility. The only other sources for which a broad–band spectral energy distribution is available is 03120017, that shows an X–ray to optical flux ratio similar to that of P3 ($\sim$ -1). The relatively strong radio emission of this source ($S_{5\rm GHz} \sim 1.3$ mJy) and the relatively unobscured

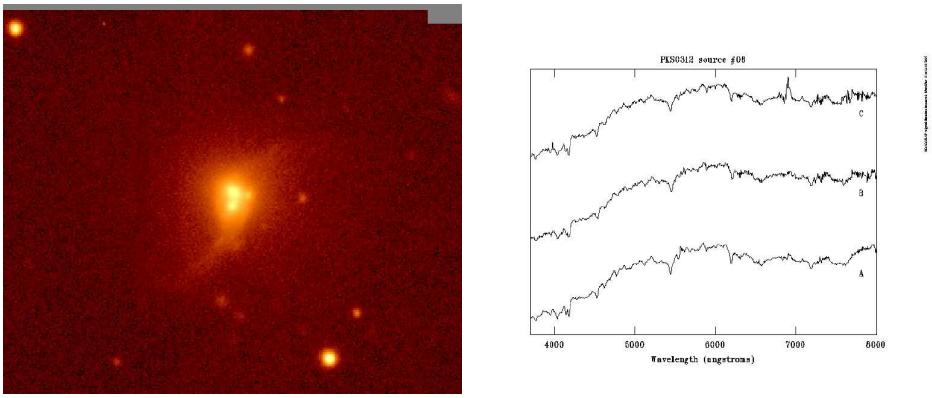

Figure 2.8 *(left panel)* The R–band image of source 8, with superimposed the XMM–*Newton* contours. *(right panel)* The optical spectra of the three nuclei associated with source 8, in order of increasing optical brightness.

X–ray spectrum ($N_H \sim 10^{21}$ cm^{-2}) favours the BL Lac hypothesis for this object. Furthermore, the 5 GHz luminosity ($\sim 3 \times 10^{40}$ erg s^{-1}), which is considered a good indicator of the overall spectral energy distribution (see Fig. 7*(a)* in Fossati et al. 1998), suggests that this object could be a rather extreme example of a high–energy peaked BL Lac (HBL; Ghisellini et al. 1998; Costamante et al. 2001). This also explains the dominance of the stellar continuum over the BL Lac non–thermal emission in the optical band.

2.4 Decoupling between the X–ray and optical properties

2.4.1 The rôle of the dust: anomalous A_V/N_H

A fraction of $\sim 10\%$ of BL AGN in the `HELLAS2XMM 1dF` sample have X–ray column densities larger than 10^{22}. These results confirm previous claims from both ASCA and *Beppo*SAX (Akiyama et al. 2000; Fiore et al. 2001a,b; Comastri et al. 2001) hard X–ray surveys.
Recently, Watanabe et al. (2004) have reveled anomalously small dust to gas ratio in circumnuclear gas of QSO selected in the hard X–rays from the ASCA survey and concluded that a fraction up to 30% of UV selected known QSO1 may show Type 2 nature in the X–rays.
This can be seen in terms of dust-to-gas ratio in a circumnuclear region. In some AGN, the nuclear extinction estimated in optical light is significantly smaller than that derived from the X–ray spectrum. Since the former is caused by dust, while the latter by gas phase metal, this suggests that a dust-to-gas ratio is much smaller than the standard value obtained in the Galaxy (Maiolino et al. 2001). The substantial variance in the dust to gas ratio, may be ascribed to the depletion of small grains due to coagulation (Maiolino, Marconi, & Oliva 2001), or, alternatively, to a geometrical separation with respect to the line of sight between the X–ray absorbing gas and dust in

front of the broad line region (Weingartner & Murray 2002).
From a purely empirical side one should not forget that variability may also play a role (see e.g. NGC 4151, Ulrich 2000 and reff. therein; Perola et al. 2004).
None of these hypotheses, though, offer an obvious answer to the fact that the anomalous cases appear to be concentrated at QSO luminosities. In any cases, the anomaly in dust-to-gas ratio affects not only the understanding of physical conditions in a circumnuclear region, but also the view of the unified scheme of AGNs; there may be a population that shows Type 1 nature in optical/UV region but show Type 2 nature in X–ray region.

It is interesting to note that, on average, the 6 absorbed BL AGN in the HELLAS2XMM 1dF sample have redder optical to near–infrared continua as measured from the optical spectra and or the optical to near–infrared colors, suggesting a dominant contribution of the host galaxy starlight or an intrinsically absorbed continuum. Many candidates of "red", presumably moderately absorbed, BL AGNs (both Seyfert and QSOs) have recently been found in radio, X–ray, and near-infrared surveys (Webster et al. 1995; Kim & Elvis 1999; Vignali et al. 2000; Wilkes et al. 2002). It has been suggested that a significant fraction of them has been missed in traditional optical/UV selections of AGNs due to the moderate absorption to the nucleus and therefore, the number density of the red AGNs can be comparable to that of optically-selected ones (Cutri et al. 2001, 2002).

Although it seems premature to claim that a population of X–ray obscured Type 1 AGN has been discovered, it is interesting to note that, if a sizable number of these objects will be found by more sensitive X–ray observations, they could have the same role in contributing to the XRB of the so far elusive class of Quasar 2 (see also Sect. 4.3).

2.4.2 The rôle of the host galaxy

The high X–ray luminosities and the relative ratios between X–ray, optical and radio fluxes strongly suggest that nuclear activity is going on in almost all the XBONG. The very nature of the mechanism responsible of the observed properties is, however, still puzzling.

It has been initially proposed that the sharp transition in the optical appearance of accreting sources at relatively low X–ray luminosities is related to a different mechanism in powering the X–ray emission with respect to high luminosities objects, raising the possibility that the X–ray galaxy population has evolved with cosmic time.
The detailed multiwavelength study of P3 (see Sect. 2.3.1) has pointed out that a heavily obscured (possibly Compton thick) AGN is the most likely explanation of the X–ray emission. It is important to note that such a possibility is not the general rule: while it is almost certain that XBONG are powered by accretion onto a massive black hole, it remains to be proved that

Compton thick absorption is ubiquitous among these sources.
On the basis of high–signal to noise X–ray spectra and/or high quality optical data, several authors have clearly demonstrated that the X–ray emission does not need to be heavily obscured and that XBONG do not definitively constitute a new class of X–ray sources. Severgnini et al. (2003) have reported a detailed X–ray spectral analysis of 3 optically normal galaxies extracted from the XMM Bright Serendipitous Source Sample. On the basis of good statistics of the XMM–*Newton* data, they have unveiled the presence of an AGN in all of them, detecting both X–ray obscured and unobscured AGNs with intrinsic 2–10 keV luminosities in the range between 10^{42} – 10^{43} erg s^{-1}. The absorption–like optical spectrum can be simply the results of the combination of the absorption associated with the AGN, the optical faintness of the nuclear emission with respect to the host galaxy, and inadequate observational set–up (e.g. low–resolution spectroscopy or bad atmospheric conditions) during the observations.
This could be particularly important for faint surveys, in which XBONG are being found in sizable numbers ($\sim$ 40–60% of the sources classified in deep *Chandra* surveys) at modest redshift ($\lesssim 1$). Moran et al. (2002) had indeed convincingly shown that the defining spectral signatures of distant Seyfert 2s *can* be completely overwhelmed by their host-galaxy light. The majority of the apparently normal galaxies that have turned up in deep *Chandra* surveys, at least those with flat (presumably absorbed) X–ray spectra and/or substantial X–ray luminosities, would probably have optical spectra similar to those of nearby Seyfert 2s.
According to this hypothesis, the majority of XBONG are therefore "classical" AGN, and the lack of AGN signatures in the optical spectrum is only an effect of the nuclear low–luminosity compared to that of the host galaxy.

A more complicate scenario than that outlined above is suggested at least for the sources for which a large amount of multiwavelength data (like for P3 and 03120017) is available. Indeed, the presence of an advection dominated accretion flow (ADAF) or a BL Lac object cannot be ruled out among the XBONG which are also relatively luminous at radio frequencies (see Brusa et al. 2003); a few examples of radio bright XBONG have been also reported by Gunn et al. (2003) in the 13hr XMM–*Newton* survey.
Almost all the possibilities investigated for P3 can be at the origin of the observed properties of few rather peculiar objects detected in the hard X–rays.

Whatever is the nature of the central engine powering the XBONG X–ray emission, a better knowledge of the space densities of these objects and of their luminosity and redshift distributions would have important consequences for the synthesis of the X–ray background: given that both low luminosity and obscured objects are strongly biased against in flux limited surveys, they might constitute an important fraction of the sources responsible of the background light (Comastri et al. 2002a).

***

The results discussed above highlight the need of a multiwavelength coverage to properly classify and study the variety of continuum and emission–line properties of the X–ray source population, and do clearly point to a complex link between optical and X–ray properties.
The overall picture emerging from our study suggests that the optical appearance of hard X–ray selected AGN is different from what expected on the basis of the unified schemes, implying that classification schemes may not apply beyond the waveband in which they were made. It is worth noting that the results that the overall hard X–ray source population cannot be described by the Unified Model in its simple formulation, add further complications to the classification scheme of AGNs.
It is interesting to note that there are several examples of obscured AGN discovered only by means of X–ray observations and not recognized by optical spectroscopy (see also Matt et al. 2001 and reference therein; Maiolino et al. 2003); therefore, X–ray spectroscopy could provide a stringent test on the role of obscuration in these objects, as hard X–ray spectra due to strong low energy absorption are expected.

Chapter 3

High X/O sources

An interesting new population of X-ray sources is present both in the deep and shallow surveys. These objects are characterized by values of their X-ray–to–optical flux ratio, as defined in the Introduction, X/O> 10, which are significantly larger than those typical of Broad Line AGN and soft X-ray selected sources in the ROSAT surveys (0.1$<$ X/O $<$10; Lehmann et al. 2001; Zamorani et al. 1999; Alexander et al. 2001).

The redshift and luminosity distribution of these sources are key parameters to test the prediction of XRB synthesis models.
It seems reasonable to argue that most of the sources characterized by a high value of X/O are high redshift, obscured AGN. Indeed, when an absorbing screen is present, the ratio between the optical to X-ray optical depth, in the observer frame, scales roughly as $(1+z)^{3.6}$, because dust extinction increases in the UV while X-ray absorption strongly decreases going toward the high energies. The net result is that the observed optical flux of high-z QSO can be strongly reduced and the observed magnitudes can be mainly due to the host galaxy starlight; conversely, the 2-10 keV X-ray flux can be much less reduced. The shape of the hard X–ray spectrum is responsible of a strong positive K–correction which "boosts" the X–ray flux and favours the detection of high redshift sources*. The hypothesis of high obscuration is supported by an analysis of their X–ray spectral properties, as determined from X–ray colours which are harder than the average spectrum of the objects with lower X/O (see Alexander et al. 2001; Mainieri et al. 2002).

If sources with large X/O were obscured AGN at $z \gtrsim 1$, a natural consequence would be that a significant fraction of them (i.e. those detected at the brightest X–ray fluxes, $> 10^{-14}$ erg cm^{-2} s^{-1}) could belong to the population of high luminosity, highly obscured Quasar (QSO2) postulated in the simplest versions of XRB models based on AGN unification

*The same effect has been already extensively used to detect high redshift, luminous, infrared galaxies at submillimeter wavelengths (Hughes et al. 1998)

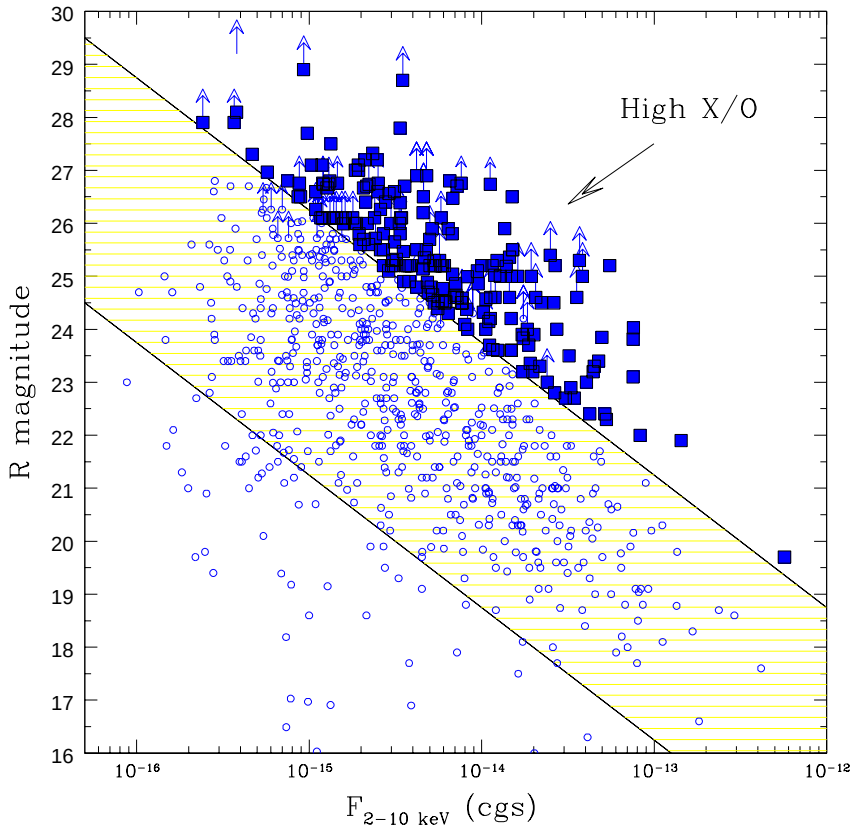

Figure 3.1 The 2–10 keV X–ray flux versus the R magnitude for a sample of hard X–ray selected sources from the HELLAS2XMMsurvey and other *Chandra* and XMM–*Newton* surveys (Barger et al. 2001a,b; Mainieri et al. 2002; Barger et al. 2002). The squares correspond to high X/O, while the circles are other classes of AGN. At X/O$<$ 0.1 normal galaxies are also present. The classical locus of AGN is reported highlighted.

schemes (i.e. Comastri et al. 1995). Moreover, they could contribute to reduce the disagreement between the redshift distribution predicted by XRB synthesis models and that observed in deep *Chandra* and XMM–*Newton* fields (Hasinger 2003; Gilli 2003), and provide an important contribution to the total energy density of the background light.

On the other hand, if they were at lower redshifts, they could belong to the population of rapidly evolving AGN postulated by Franceschini et al. (2002) and closely linked to starburst galaxies discovered in the infrared band with ISO, calling for substantial revisions of the models (Gilli, Salvati & Hasinger 2001).

Since high luminosity, obscured quasars may also provide a relevant fraction of the black hole mass density due to growth by accretion, a much better knowledge of their space density and evolutive properties is needed to understand and quantify the evolution of accreting black holes with cosmic time.

It is interesting to note that the fraction of high X/O in hard X–ray samples is almost constant (about 20%) down to $\sim 10^{-16}$ erg cm^{-2} s^{-1} in the 2 Ms CDFN observation and over the entire range of X–ray fluxes sampled by deep and shallow surveys (see Fig. 3.1).
As already discussed in the Introduction, spectroscopic redshifts for the sources detected at the brighter X–ray fluxes (as in the HELLAS2XMM sample) can be obtained with 10m class telescopes. Most of the X/O$\gtrsim 10$ objects from ultra-deep *Chandra* and XMM–*Newton* surveys (e.g. CDFN, CDFS) have R> 25 and therefore are not accessible to optical spectroscopy. The redshift of objects with $25 \lesssim$R$\lesssim 27$ could be determined through photometric redshifts techniques, on the basis of good quality optical and near–infrared data and the comparison of the observed SED to galaxy and AGN templates. This is also feasible with 10m class telescopes. Spectroscopic and photometric redshifts of fainter sources (R$\gtrsim 27$) must await next generation facilities like the 30-50m ground based telescopes and NGST. In the mean–time, redshift estimates based on alternative approaches (e.g by detecting and identifying emission features in the X–ray spectrum) are needed.

In the following I will describe the main efforts made in the framework of the HELLAS2XMM survey to estimate the redshifts and derive the intrinsic X–ray properties (luminosity and column density) of high X/O sources. More specifically: the spectroscopic observations of the X–ray brightest sources (Sect. 3.1), near–infrared follow–up of R–band undetected objects (Sect. 3.2) and alternative approaches developed to derive redshifts for faint sources (Sect. 3.3).

3.1 Spectroscopic classification of high X/O in the HELLAS2XMM 1dF sample

For all the sources in the HELLAS2XMM 1dF sample we have computed the X–ray to optical flux ratio. The X–ray flux is that reported in Table 1.2. The R band flux is computed by converting R magnitudes into specific fluxes and then multiplying by the width of the R filter. We used $f_R(0) = 1.74 \times 10^{-9}$ erg cm^{-2} s^{-1} $\mathring{A}^{-1}$ and $\Delta\lambda_R = 2200\mathring{A}$ (Zombeck 1990). The X–ray to optical flux ratio can thus be written:

$$\log(\mathrm{X/O}) = \log(\mathrm{F_X}) + 5.4176 + \mathrm{R}/2.5 \qquad (3.1)$$

Twenty–eight objects in the HELLAS2XMM 1dF sample satisfy the selection criterion log(X/O)> 1. These are reported in Table 3.1.
The high level of X–ray flux coupled with the large area surveyed allowed us to select a sizable subsample (13 objects, about 50% of the entire HELLAS2XMM high X/O population) of objects with optical counterparts between R=22 and R=24, thus bright enough for reliable spectroscopic redshifts and classifications to be obtained with ground–based telescopes.

Table 3.1 **High X/O sources in the HELLAS2XMM 1dF sample**

Id	$F_{2-10keV}$ 10^{-14} cgs	R	lg(X/O)	Class.	z	$logL_{2-10keV}$ erg/s	N_H 10^{22} cm^{-2}
05370022	2.40	$\gtrsim$23.0	> 1.0	–	–	–	–
05370021	3.22	23.5	1.32	ELG	1.192	44.35	$0.16\pm^{1.50}_{0.16}$
05370091[a]	2.50	$\gtrsim 24.5$	> 1.61	–	–	–	–
05370159	1.06	$\gtrsim$24.0	> 1.04	–	–	–	–
05370157	0.77	$\gtrsim$24.5	> 1.10	–	–	–	–
05370153	1.13	$\gtrsim$24.6	> 1.31	–	–	–	–
05370054[a]	1.62	$\gtrsim 25.0$	> 1.63	–	–	–	–
05370060	1.72	23.9	1.21	–	–	–	–
05370010	4.24	22.4	1.00	–	–	–	–
0537011a	4.76	23.4	1.45	AGN2[b]	0.981	44.33	$1.33\pm^{1.50}_{0.90}$
05370164	1.49	23.6	1.03	AGN2	1.824	44.48	uncons.
05370111[a]	3.69	$\gtrsim 25.3$	> 2.10	–	–	–	–
05370123	7.53	23.1	1.53	AGN1	1.153	44.72	$6.63\pm^{21.58}_{4.06}$
03120036[a]	1.45	$\gtrsim 24.6$	> 1.42	–	–	–	–
03120065	1.47	$\gtrsim$24	> 1.18	–	–	–	–
03120006	8.28	22.0	1.13	AGN2	0.680	44.16	< 0.16
03120031[a]	1.20	$\gtrsim 24.6$	> 1.34	–	–	–	–
03120045[a]	1.94	$\gtrsim 25.0$	> 1.70	–	–	–	–
03120116	2.01	23.9	1.28	ELG	0.814[c]	43.87	uncons.
26900075[a]	2.06	$\gtrsim 24.6$	> 1.57	–	–	–	–
26900029[a]	3.56	$\gtrsim 25.1$	> 2.01	–	–	–	–
26900002	14.35	21.9	1.33	AGN1	0.850	44.66	$0.54\pm^{0.29}_{0.30}$
26900072	4.05	23.0	1.22	ELG	1.389[c]	45.37	$59.3\pm^{77.7}_{49.5}$
15800062	4.49	23.3	1.39	AGN2	1.568	44.80	$26.3\pm^{44.7}_{18.1}$
50900001	4.97	23.9	1.67	AGN2[b]	1.049	44.40	< 1.14
50900067	5.29	22.3	1.06	AGN1	1.076	44.44	< 0.57
50900013	4.42	23.2	1.34	AGN2	1.261	44.55	$2.52\pm^{4.58}_{2.15}$
50900039	5.19	22.4	1.09	AGN1[b]	0.818	44.17	< 0.83

Classification as in Table 1.2. [a] Sources selected for K–band observations (see Sect. 3.2); [b] Classification tentative; [c] redshift tentative, based on a single faint line.

This has to be compared with the 9 out of 38 identifications in the CDFN, SSA13 and LH samples (including 3 photometric redshift of faint optical sources in the LH sample; see Sect. 3.3.1).
The observations were performed with FORS1 at the VLT and details are given in Sect. 1.3. The identification breakdown of these sources is quite varied and is given in Table 3.1: 4 objects are classified as Type 1 AGN (AGN1), 6 as Type 2 AGN (AGN2) and 3 as Emission Line galaxies (ELG). For the identified objects, rest–frame column densities and unabsorbed 2–10 keV luminosities have been derived. *All* the sources have intrinsic hard X–ray luminosity $L_{2-10} \gtrsim 10^{44}$ erg s^{-1}, i.e. in the Quasar regime. Combining the optical and X–ray information, one third of the identified sources (3 AGN2

and 1 ELGs) can be classified as "classic" Type 2 Quasars, based on the absence of broad optical lines and X–ray obscuration in excess than 10^{22} cm^{-2}. Also present in this sample is an absorbed BL AGN, thus classified as an X–ray Type 2 QSO.
These results strongly confirm that spectroscopic follow–up of high X/O selected in large area surveys provide an efficient method to find high–luminosity, narrow–line objects: the paucity of Type 2 QSO among the identified sources in deep X–ray surveys might therefore be partly due to a selection effect.

The redshift distribution of the identified HELLAS2XMM high X/O spans the range z$\sim$0.7-1.8. Evidences that high X/O sources lie at $z > 1$ have been already raised on the basis of photometric data (see e.g. Alexander et al. 2001; Mainieri, PhD Thesis). It has been proposed that these objects would help to reduce the disagreement between the observed redshift distribution (mainly weighted by the brightest sources) and that predicted by AGN synthesis models. However, so far only for a handful of objects have been published optical or near–infrared spectra (see e.g. Gandhi et al. 2004; Willott et al. 2003). These results therefore, constitute the *first spectroscopic proof over a statistically significant sample that high X/O sources (that constitute a significant fraction of the optically faint population) lie at z$\sim$1.*

3.2 Near–infrared observations of faint optical sources in HELLAS2XMM

All but two of the remaining sources with high X/O and without spectroscopic redshift in the HELLAS2XMM 1dF sample are undetected in the R–band (see Tab. 3.1). These objects are again very challenging to be followed–up with the optical spectrographs attached to 10m class telescopes, being both very faint ($R \gtrsim 24$) and spread over large area of the sky, making unfeasible any deep exposures with multi-object instruments.

The trend of finding redder sources among unidentified objects at fainter optical fluxes, as well as the increasing fraction of EROs, are well documented results obtained by various X-ray surveys (Mainieri et al. 2002; Alexander et al. 2002). This motivates the choice of the near infrared as the natural band to carry out a follow-up study of high X/O sources.
Therefore, we started a pilot study in the K_s band selecting a restricted (11 objects), but meaningful, sample of HELLAS2XMM high X/O sources undetected in the optical band down to the limit of our images. The details on the data acquisition, analysis and reduction of the K_s fields have been already presented in Sect. 1.1.3.
We searched in the K_s catalog for objects closer than 6″ to the X-ray position; for the identification of the infrared counterparts we made use of

Table 3.2 Near–infrared and X–ray properties of high X/O in the HELLAS2XMM 1dF sample

ID	lg(X/O)	RA(K_s) (J2000)	DEC(K_s) (J2000)	K_s [a]	$R-K$ [b]	m [c]	z_{min}	M_K	N_H 10^{22} cm^{-2}	L_X [d] 10^{44} erg s^{-1}
26900075	>1.65	23 59 56.41	-25 10 17.6	18.32	6.3 ± 0.7	E	$1.30^{+0.20}_{-0.20}$	-25.83	$15.3^{+23.2}_{-9.1}$	3.5
26900029	>1.89	00 01 11.50	-25 12 06.5	17.68	7.4 ± 1.0	P	$2.40^{+0.90}_{-0.40}$	-29.74	$2.8^{+3.5}_{-2.1}$	11.2
16274069	>1.72	00 50 30.86	-52 00 47.6	17.83	6.6 ± 0.8	E	$1.40^{+0.20}_{-0.20}$	-26.53	$2.6^{+1.6}_{-1.1}$	3.6
16274181	>1.50	00 50 31.51	-52 06 33.9	18.69	6.2 ± 0.4	E	$1.30^{+0.10}_{-0.10}$	-25.45	$1.1^{+3.2}_{-1.0}$	1.2
03120045	>1.79	03 10 18.93	-76 59 58.4	18.70	5.7 ± 0.7	P	$1.65^{+0.35}_{-0.65}$	-28.02	$6.6^{+7.4}_{-3.8}$	4.9
03120031[e]	>1.42	03 11 13.65	-76 53 59.6	18.31	5.3 ± 0.5	D	$0.80^{+0.20}_{-0.20}$	-24.77	$1.2^{+1.2}_{-0.8}$	0.5
03120036[e]	>1.50	03 13 42.90	-76 54 23.9	19.11	5.5 ± 0.5	E	$1.05^{+0.20}_{-0.20}$	-24.44	$1.2^{+1.5}_{-1.0}$	1.0
05370111[e]	>2.19	05 39 11.60	-28 37 15.1	17.66	6.8 ± 0.7	E	$1.45^{+0.20}_{-0.20}$	-26.80	$12.0^{+16.6}_{-7.2}$	2.8
05370054[e]	>1.71	05 39 45.22	-28 49 09.8	18.91	>6.2	E	>1.30	-25.24	$1.6^{+2.4}_{-1.2}$	>1.6
05370091[e]	>2.06	05 40 21.13	-28 50 37.6	18.99	5.1 ± 0.5	E	$0.90^{+0.20}_{-0.20}$	-24.17	$15.7^{+49.9}_{-11.2}$	2.0

[a] "total" magnitude: MAG_BEST from *SExtractor*.
[b] Fixed 3″-diameter aperture color.
[c] Morphology from least-square fit: P=point-like – E=Bulge profile – D=Disky profile.
[d] 2-10 keV, unabsorbed X–ray luminosity
[e] source in the FOV of *Chandra* observations.

the *Chandra* positional accuracy (when available) and the X–ray to infrared association was made following the procedure described in Sect. 1.2. *Ten out of 11 sources were securely identified with a relatively bright ($K_s \leq 19$) near-infrared object.*

The bright near-infrared counterparts have optical to near-infrared colors considerably redder than the field population and all of them are classified as Extremely Red Objects (EROs, with $R-K>5$). Given the ERO surface density expected at these magnitude levels ($\sim$1 object per square arcmin, see Daddi et al. 2000; Roche et al. 2002), it is remarkable that we found them nearly ubiquitous in the relatively small X–ray error boxes.
The $R-K$ color distribution of all of the *ISAAC* detections with $K_s<21.5$ is reported in Fig. 3.2. The exceptional nature of the high X/O counterparts is quite obvious. The six $R-K>6$ counterparts, with $K_s<19$, are very rare objects: in this region of the color-magnitude plane one finds 20 galaxies in total, representing the mere 3% of the whole galaxy population; the three brightest counterparts, with $K_s<18$ *and* $R-K>6$, are unique with respect to the galaxy field population, as no other object shares the same photometric properties, and they were never found by any other X–ray survey.

3.2.1 Near-Infrared Morphologies

We have combined the photometric information with an accurate morphological analysis. With the exception of the identifications of 26900029 and 03120045, morphologically classified as point–like objects, all of the other sources are clearly extended. The good quality of the data allowed us to distinguish between disky (exponential) and bulge ($r^{1/4}$) profiles in the extended objects and to obtain a reliable measure of the *intrinsic* effective

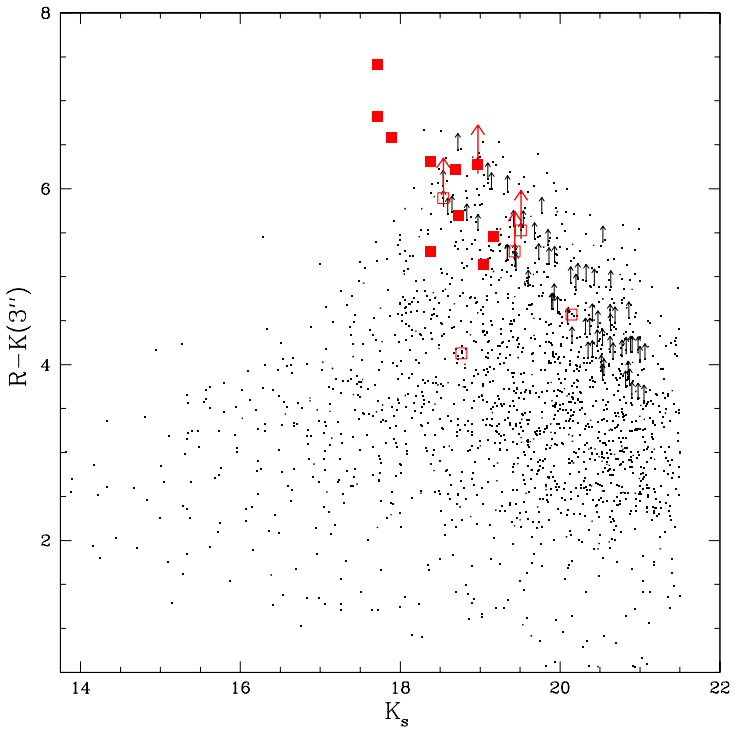

Figure 3.2 Fixed-aperture R-K_s color versus "total" K_s magnitude for all the *ISAAC* detections with $K_s < 21.5$; the large filled squares indicate the ten counterparts of the selected hard X-ray sources with high X/O. The large empty squares are the "secondary" counterparts.

radius of the host galaxies (see Mignoli et al. 2004 for a careful description of the analysis). The morphological breakdown is dominated by elliptical profiles, and only one source can be described by a disky profile. Moreover, on the basis of extensive simulations, we have determined that the possible contribution from unresolved sources, which would be expected to trace the X-ray emitting AGN, is almost negligible ($\lesssim$ 15%) in all the ellipticals and can be important ($\sim$50%) only for the disky galaxy. Table 3.2 gives all the relevant photometric and morphological information about the detected counterparts.

3.2.2 Colour based redshifts

The lack of a multi-band coverage does not allow us to estimate a precise photometric redshift. Nevertheless, "minimum" photometric redshifts ($z_{\rm min}$) for all of the sources have been estimated using the color-redshift diagram ($R-K$ vs. z) and different templates according to the different morphologies: for the point-like sources, since the emission from the AGN is contributing significantly in the optical/near-IR range, we have used as

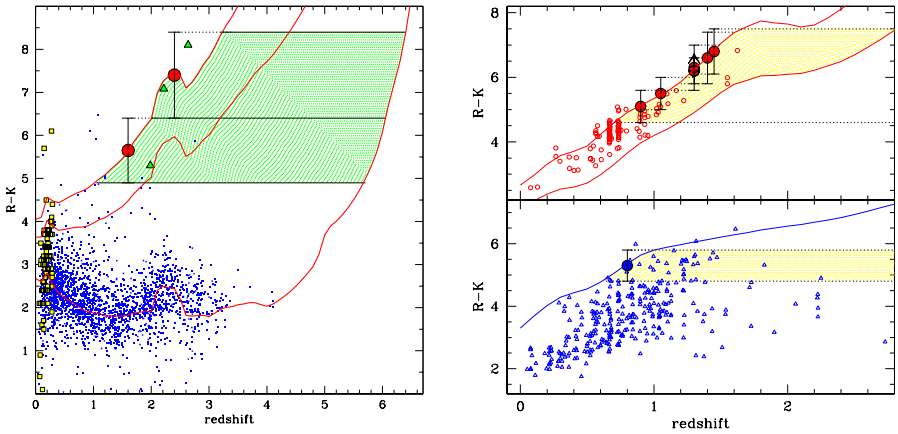

Figure 3.3 Redshift vs. optical-to-near infrared color for point-like objects (left panel) and for extended objects (right panel). In both panels, the large filled dots represent our sources. In left panel, the small squares are the optically selected quasars from Barkhouse & Hall 2001), whereas the larger squares indicate the 2MASS quasar sample (Hutchings et al. 2003). The three solid triangles are the high-z reddest QSO from Gregg et al. (2002). The curves represent the color–redshift relations for the adopted quasar template with three different extinction values ($E(B-V) = 0.0, 0.4, 0.7$, from bottom to top). In right panel, the smaller empty symbols are sources from the K20 spectroscopic survey (Cimatti et al. 2002b).; also the "maximum color – minimum redshift" tracks are shown (see Mignoli et al. 2004 for details). In both panels the redshift-permitted region of `HELLAS2XMM` sources is shaded.

QSO template the composite spectrum from the Large Bright Quasar Survey (LBQS; Francis et al. 1991), extended to the near-IR using the mean quasar energy distribution for radio quiet quasar of Elvis (1994; see also Maiolino et al. 2000); for extended objects (both bulge and disky morphology) the adopted templates consist of a set of synthetic spectra (Bruzual & Charlot 1993), with different star formation histories and spanning a wide range of ages (the basic set of templates includes only solar metallicity and Salpeter's Initial Mass Function).

Point-like objects

In the left panel of Fig. 3.3 the color-redshift diagram for the two point-like sources (large filled dots) is shown, along with data taken from literature and with the composite spectrum from the LBQS, extended to the near-IR as described above. The effect of the intergalactic medium (IGM) attenuation (Madau et al. 1995) is clearly visible at high redshift. In order to reproduce the red quasars $R-K$ colour, we have included the effect of internal dust attenuation on the Francis extended template: the attenuated templates reproduce quite well most of the low-z red quasar sample, as well as the high-z reddest QSOs, with E(B-V) ranging from 0 to 0.7, corresponding to

$A_V < 2.0$ (see also Gregg et al.2002). It is worth to note that most (10 over 13) of QSOs with $R-K > 5$ and known redshift lie at $z > 1$; using the template drawn from the maximum extinction value ($E(B-V) \simeq 0.7$) in the color–redshift diagram and the the observed $R-K$ colors, it is possible to derive the minimum redshift of the two extremely red point-like sources.

Extended sources

Following a similar procedure, minimum redshifts for sources with a bulge or disky profile have been estimated, using for comparison the samples of early-type galaxies and dusty systems in the K20 spectroscopic survey (Cimatti et al. 2002b).
To conservatively derive a minimum redshift for early-type galaxies, the model which best represents the upper envelope of the K20 data in the $R-K$ vs. z plane (i.e. providing the reddest colors at each redshift) has been adopted; a lower $z_{\rm form}$ and/or a more gradual star formation history in the models would result in bluer colors and in a corresponding higher $z_{\rm min}$.
To reproduce the colors of the most extreme emission-line dusty objects, we have chosen a model with constant Star-Formation Rate (SFR) and $E(B-V) = 0.6$ (cf. Cimatti et al. 2002a and Pozzetti et al. 2003).
We have then assigned a $z_{\rm min}$ to each of our sources according to their $R-K$ color and morphological type: the minimum redshifts for bulge and disky profile sources are in the range of $0.80 \leq z \leq 1.45$ (Fig. 3.3, right panel).
Taking into account that the M_{stars}/L_K ratio for an old stellar population could vary from 0.3 (for an age of 1 Gyr, assuming a Salpeter IMF) to about 1 (for 6 Gyrs, the age of the universe at $z = 0.9$), we estimate the galaxy stellar Masses of our hosts: they are all above 3×10^{10} $M_\odot$ (and 4 of them above 10^{11} $M_\odot$), corresponding to the stellar-Mass of an L^* galaxy in the local Universe (Cole et al. 2001).
The elliptical hosts of hard X-ray sources with extreme X/O are, therefore, among the *most massive spheroids* at these redshifts, possibly addressing the issue of elliptical galaxy formation and the expected co-evolution with the black-hole accretion (Granato et al. 2001).

3.2.3 X–ray properties

The XMM–*Newton* spectra of all the ten high X/O sources have been fitted with a single power law model plus absorption in the source rest–frame assuming for all of them the "minimum" redshift estimated in the previous section. The quality of the X-ray spectra in terms of S/N ratio is not such to simultaneously constrain both the slope and column density. For this reason the former has been fixed at Γ=1.9, the average value obtained by fitting the "bright" part of the HELLAS2XMM sample (see Perola et al. 2004, for a detailed description of the spectral analysis procedures). The best fit values for the intrinsic column densities and unabsorbed X-

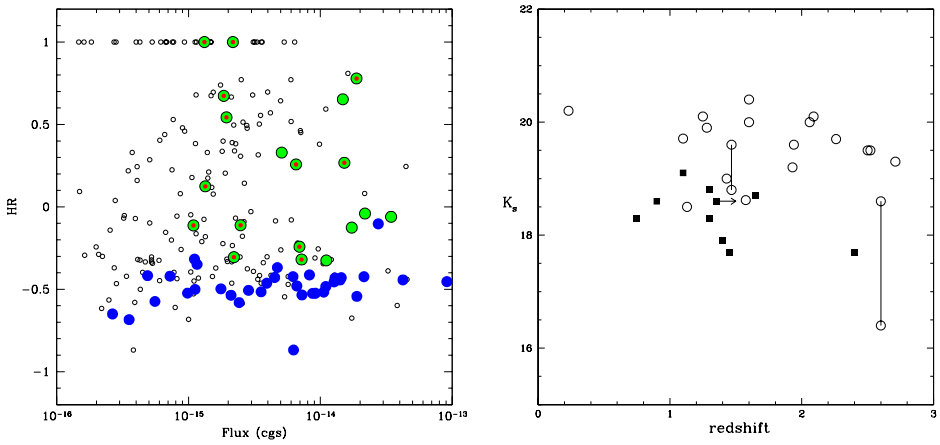

Figure 3.4 (*left panel*) HR vs. the hard X–ray flux is reported for all the sources with spectroscopic or photometric redshifts in the CDFN. Sources with high X/O are marked with green symbols, and those with R-K$>$ 5 colors are dotted with additional red symbols. As a comparison, sources with an unobscured X–ray spectrum and optically identified as Broad Line AGN are marked with blue circles. (*right panel*) Redshift vs. K_s magnitude for our targets (filled square) and for a comparison sample of high X/O sources with ERO colors extracted from the literature (empty circles; see text). The two pairs of connected circles represent two lensed objects in the Abell2390 field (Crawford et al. 2001) with observed and de-magnified K_s.

ray luminosities are listed in Table 5. More than half (6 out of 10) of the sources in the sample have N_H larger than 10^{22} cm^{-2}, while the 90% upper limits of the remaining 4 do not rule out significant X-ray absorption. In order to check whether X-ray absorption is common among this type of objects we have built up a comparison sample of high X/O sources with ERO colors serendipitously discovered at X-ray fluxes comparable to those of the HELLAS2XMM sample. We have considered only those X-ray sources for which a reliable spectroscopic or photometric identification was available in the literature: #19 and #25 in the Lockman Hole (Mainieri et al. 2002; see also Stevens et al. 2003); A15 and A18 in A2390 field (Crawford et al. 2001, Gandhi, Crawford & Fabian 2002); N2_21 and N2_28 in the ELAIS survey (Willott et al. 2003). All but one (N2_21) of the objects in the comparison sample have column densities in excess of 10^{22} cm^{-2}, in agreement with the results obtained for the HELLAS2XMM sample.
The unabsorbed 2–10 keV X-ray luminosities of all but two of the objects in the HELLAS2XMM and in the comparison sample are larger than 10^{44} erg s^{-1}. The majority of relatively bright hard X-ray selected sources with high X/O and ERO colors are therefore obscured, high-luminosity AGN, i.e., Type 2 quasars (see also Fiore et al. 2003).

At fainter X-ray fluxes, sources with extremely high X-ray-to-optical flux ratios have been also discovered in the deep pencil-beam surveys. From

the Barger et al. (2003) catalog of the 2 Ms CDF-N observation, we have selected all of the objects with X/O>10 and $R-K$>5; among these, 13 sources have a spectroscopic or photometric redshift. For the two brightest sources absorption column densities in excess of 10^{23} cm^{-2} were derived through proper spectral analysis (see Civano et al. in preparation). In the remaining cases, the intrinsic column densities have been inferred from the Hardness-Ratio technique. In Fig. 3.4 (*left panel*) the HR vs. the hard X–ray flux is reported for all the sources with spectroscopic or photometric redshifts in the CDFN. Sources with high X/O are marked with green symbols, and those with R-K>5 colors are dotted with additional red symbols. In the same plot, sources with an unobscured X–ray spectrum and optically identified as Broad Line AGN are marked with blue circles. In all but one cases, intrinsic column densities derived from the observed HR are in excess of 10^{22} cm^{-2} (see also Alexander et al. 2002 for the 1 Ms CDF-N observation).
Figure 3.4 (*right panel*) shows that all but one of the 19 sources in the comparison samples lie in the same redshift range derived for HELLAS2XMM sources, thus reinforcing the reliability of the redshift determination method (Sect. 3.2.2).
Deep HST ACS observations of a small sample of 7 *Chandra* sources in the CDF-S with extremely high X/O and red colors (EXOs: Extreme X-ray-to-Optical ratio sources) have been recently discussed by Koekemoer et al. 2003. All of them were not detected down to very faint optical magnitudes ($z(850) \simeq 28$), although these sources are clearly detected in the K_s band ($K_{vega} \simeq$ 20.4–23). It has been proposed that these sources could be high-redshift ($z > 6$) L* galaxies powered by a moderately luminous AGN ($L_X = 2-6 \times 10^{44}$ erg s^{-1}). If they were at lower redshifts, they would be unusually under-luminous galaxies. The *Chandra* EXOs could then constitute the high–redshift tail of a population of obscured AGN which is sampled at lower redshifts by the HELLAS2XMM high X/O sources. The relatively soft X-ray spectra of *Chandra* EXOs, as inferred from their Hardness-Ratio distribution, would also be consistent with a high-z hypothesis.

3.3 High X/O sources in a context and other redshift determinations

As already pointed out, spectroscopic redshifts for sources with high X/O demand the utilization of 8m class telescopes and can be obtained only for the brightest sources. The majority of the objects, however, have optical counterparts well below the capabilities of the largest telescopes, calling for different methods of redshift estimates.

3.3.1 A statistical approach

A comprehensive picture of the space densities of high X/O sources can be obtained through the full exploitation of data from both shallow and deep surveys. In Fiore et al. (2003) a method to statistically assign a redshift to

all the unidentified sources in hard X–ray samples has been proposed.

In addition to the results from the HELLAS2XMM 1dF sample, those obtained from other three hard X-ray surveys have been used:

- 1 - CDFN 1Ms sample (from Brandt et al. 2001a; Barger et al. 2002): 88 sources with $F_{2-10keV} > 10^{-15}$ erg cm^{-2} s^{-1}in the inner 6.5 arcmin radius region plus 32 sources with $F_{2-10keV} > 5\times10^{-15}$ erg cm^{-2} s^{-1}in the annulus between 6.5 and 10 arcmin radii, for a total of 120 sources (67 with a spectroscopic redshift).
- 2 - Lockman Hole sample (fluxes from Baldi et al. 2002; identifications from Mainieri et al. 2002): 55 sources in the inner 12 arcmin radius region, 44 already identified (41 spectroscopic redshifts and 3 photometric redshifts);
- 3 - SSA13 sample (from Mushotzky et al. 2000; Barger et al 2001): 20 sources with $F_{2-10keV} > 3.8 \times 10^{-15}$ erg cm^{-2} s^{-1}in a 4.5 arcmin radius region, 13 with spectroscopic redshift.

The combined sample consist of 310 hard X-ray selected sources, 221 (70%) of them with spectroscopic redshifts. The classifications of the optical spectra from the additional samples are adopted from the above publications, when available. Otherwise, a classification based on visual inspection of the published optical spectra (Barger et al. 2001, 2002), adopting the criteria in Sect. 1.3 has been used.
In the following, two broad optical categories will be considered: *optically unobscured AGN*, i.e. Type 1, broad emission line AGN, and *optically obscured AGN*, i.e. AGN whose nuclear optical emission is totally or strongly reduced by dust and gas in the nuclear region and/or in the host galaxy. The identified sample includes 113 optically unobscured AGN and 108 optically obscured AGN.

Table 3.3 gives the total number of sources and the number of spectroscopic identification in two flux intervals ($F_{2-10keV} = 10^{-15} - 10^{-14}$ erg cm^{-2} s^{-1}and $F_{2-10keV} \gtrsim 10^{-14}$ erg cm^{-2} s^{-1}) and in three bins of X/O (> 10; 3–10; 0.1-3. 11 sources have X/O< 0.1). In both bins of X–ray fluxes the number of objects with X/O> 3 is comparable to that of those with X/O=0.1-3, but the degree of completeness in the identifications, is much higher above 10^{-14} erg cm^{-2} s^{-1}. Notably, among

Table 3.3 **Number of sources and class ratio per bins of flux and X/O**

	$F_{2-10} < 10^{-14}$		$F_{2-10} > 10^{-14}$	
	N. sources (Id) %	non–AGN1/AGN1	N. sources (Id) %	non–AGN1/AGN1
$0.1-3$	72(54) 75%	$1.21^{+0.36}_{-0.30}$	97(94) 97%	$0.31^{+0.09}_{-0.07}$
$3-10$	29(7) 24%	$2.5^{+3.7}_{-2.0}$	36(30) 83%	$1.1^{+0.5}_{-0.4}$
>10	22(1) 5%	-	43(19) 44%	$3.8^{+3.2}_{-2.0}$

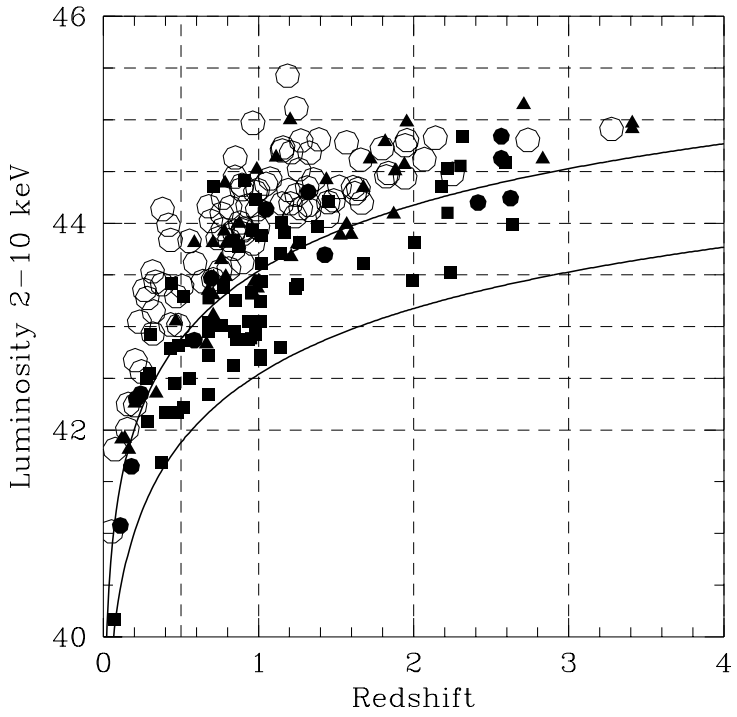

Figure 3.5 The 2-10 keV luminosity as a function of the redshift for the sources in the combined sample. Symbols are as follows: open circles = HELLAS2XMM; filled squares = CDFN; filled triangles = Lockman Hole; filled circles = SSA13). The lower and upper solid lines represent the flux limits of 10^{-15} erg cm^{-2} s^{-1}(i.e. Chandra deep surveys) and 10^{-14} erg cm^{-2} s^{-1}(i.e. HELLAS2XMM 1dF survey) respectively.

the 65 sources with X/O$>$ 10 in this combined sample ($\sim$20% of the overall X–ray population), 20 have been spectroscopically identified, the majority (13) from the HELLAS2XMM survey (Sect. 3.1).

Table 3.3 gives also the ratio of optically obscured to optically unobscured AGN, per bins of X/O and fluxes. Although the errors on the ratios are large, a trend toward a higher fraction of optically obscured objects is suggested going both toward higher X/O values and toward lower fluxes.

For all the identified sources, the rest frame 2–10 keV, absorption corrected X–ray luminosities have then been estimated from the redshift and the observed softness ratios (defined as (S-H)/(S+H), where S and H are the 0.5-2 keV and 2-10 keV fluxes respectively) and assuming a power law index $\Gamma = 1.8$. (see Fiore et al. 2003 for a detailed discussion on the uncertainties related to the assumed X-ray spectral parameters). The luminosity vs. redshift plane for the sources with spectroscopic redshift in the combined sample is shown in Fig. 3.5.

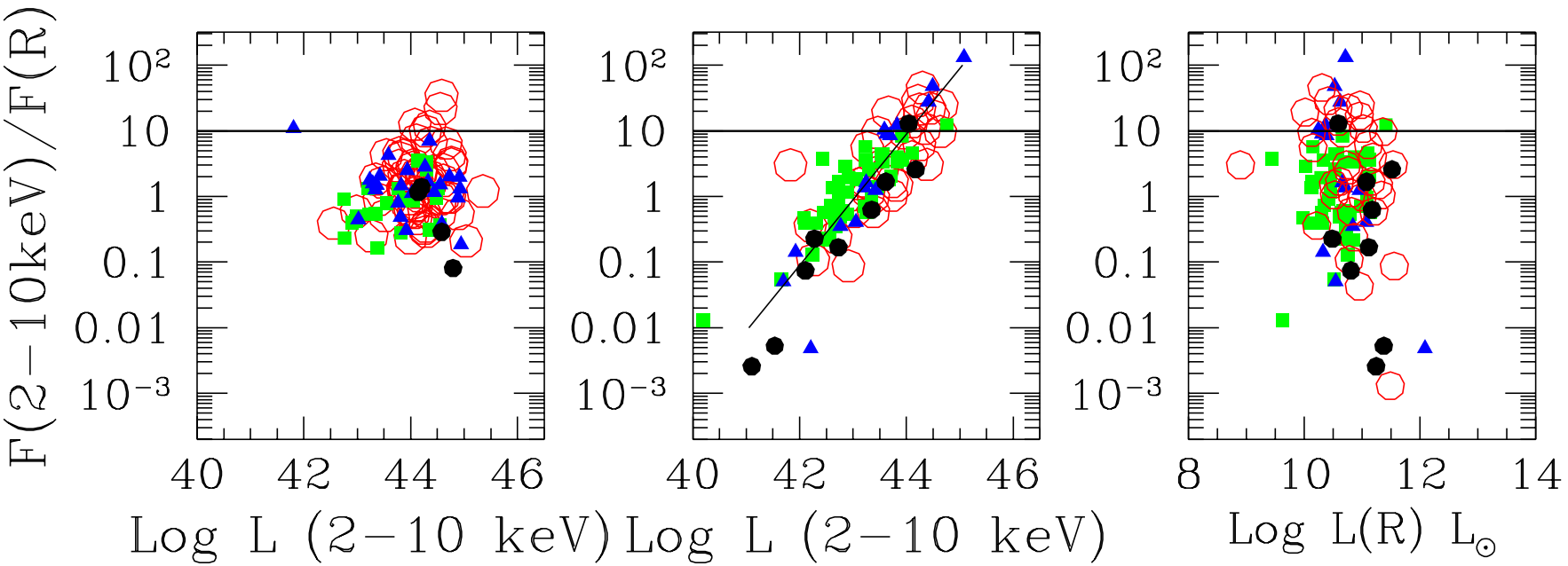

Figure 3.6 The X-ray to optical flux ratio as a function of the X-ray luminosity for Type 1 AGN (left panel) and non Type 1 AGN and galaxies (central panel), and as a function of the optical luminosity for the latter class (right panel). Symbols as in Fig. 3.5. The horizontal lines mark the level of X/O=10. The diagonal line in the central panel is the best linear regression between log(X/O) and $\log L_{2-10keV}$.

In the left panel of Fig. 3.6, the X/O ratio as a function of the X-ray luminosity for broad line AGN (i.e. the *optically unobscured* AGN) is shown. The average X/O for the 113 broad line AGN of the combined sample is 1.2 ± 0.3 (standard deviation). The average X/O of 35 optically selected QSO from the PG sample with ASCA and BeppoSAX fluxes (George et al. 2000; Mineo et al. 2000) is 0.3 ± 0.4. The difference in the average is due to the fact that optical selection produces a tail toward low X/O: $\sim 15\%$ of the optically selected QSO are very X-ray faint, see Laor et al. (1997), having X/O$<$0.1, against $\sim 1\%$ for the broad line AGN in the combined sample.
The central panel of Fig. 3.6 shows the X/O ratio as a function of the X-ray luminosity for narrow-line AGN and galaxies (i.e. the *optically obscured* AGN). There is here a striking correlation between X/O and $L_{2-10\rm keV}$: higher luminosity AGN tend to have higher X/O. The solid diagonal line in the panel represents the best linear regression between log(X/O) and $\log L_{2-10keV}$ (a least square fit gives a slope slightly flatter). A very similar correlation is obtained computing the ratio between the X-ray and optical luminosities, instead of fluxes (because the differences in the K corrections for the X-ray and optical fluxes are small in comparison to the large spread in X/O).
All objects plotted in the central panel of Fig. 3.6 do not show broad emission lines, i.e. the nuclear optical-UV light is completely blocked, or strongly reduced, unlike the X-ray light. Indeed, the optical R band light of these objects is dominated by the host galaxy and therefore, *X/O is roughly a ratio between the nuclear X-ray flux and the host galaxy starlight flux*.
It is worth noting that while the X-ray luminosity of obscured objects spans about 4 decades, the host galaxy R band luminosity has only a moderate scatter (~ 1 dex) around the mean value of 10^{11} $L_\odot$ (Fig. 3.6, right panel) and it is rather independent of redshift (Fiore et al. 2003b). The X-ray to optical flux and luminosity ratios of non broad line AGN therefore might be used to investigate and constrain the relationship between the supermassive black hole masses and efficiency of accretion, and bulge optical luminosity (e.g. Gebhardt et al. 2000).

The redshift distribution of the 221 sources in the combined sample with a spectroscopically confirmed redshift shows a sharp decrease at z >1.2 (shaded area in Fig. 3.7) which is similar to that observed in the CDFN (Barger et al. 2003) and CDFS (Hasinger 2003).
Making use of the above described correlation and assuming the ratio between obscured and unobscured sources reported in Table 3.3, it is possible to predict luminosities for the faint X–ray sources, and therefore to statistically assign redshifts to the 30% of the unidentifed sources in the combined sample, following the procedure outlined in Fiore et al. 2003 (Sect. 5.2).
When the sources with an estimated redshift are added, the overall distribution is still peaked at $z \simeq 1$, but the decrease above this redshift is less sharp (continous area in Fig. 3.7), thus suggesting that the low redshift peak in the distribution of the sources with spectroscopic redshift is enhanced

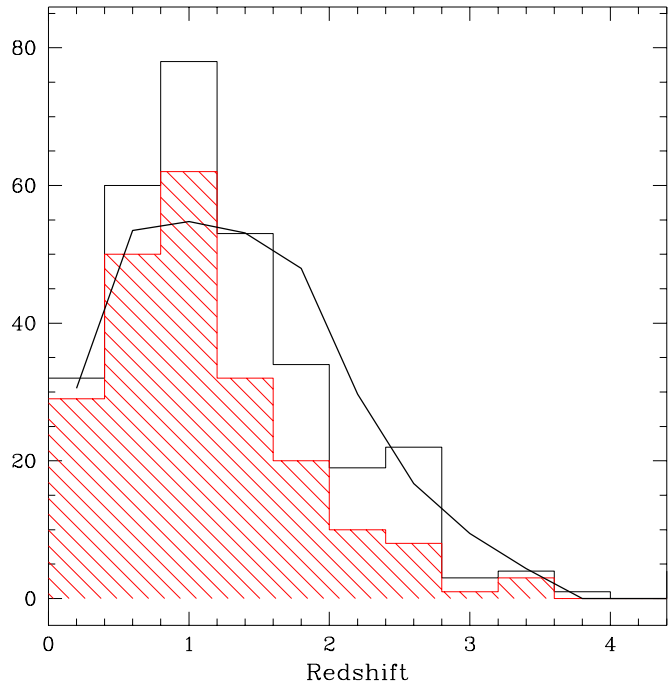

Figure 3.7 The z distribution of the 310 sources in the combined sample. Shaded histogram = distribution of the spectroscopically identified sources (70 % of the sample). Solid histogram = full sample. The luminosity and the redshift of the sources without a spectroscopic redshift have been estimated using the correlation in Fig. 3.6, and the fraction of obscured to unobscured sources in Table 3, see Sect. 5.2 for details. The black thick line represents the expectation of the AGN synthesis models of the XRB (Comastri et al. 2001), folded through the appropriate sky-coverage, where unobscured and obscured AGN follow the same pure luminosity evolution.

by the incompleteness of the optical identification, in particular at high X/O values (Table 3.3).
The solid thick curve in Fig. 3.7 represents the expectation from the baseline AGN synthesis models of the XRB presented in Comastri et al. (2001), where unobscured and obscured AGN, in a fixed proportion, share the same, pure luminosity cosmological evolution. The adopted model predicts a much broader peak between z=1 and z=1.8, falling short of the observed distribution at z$<$ 1 and demanding for a slightly higher number of objects at z=1-2. The agreement is instead rather good at z$>$ 2. The contrast does not appear as dramatic as, e.g., in Franceschini et al. (2002) and Hasinger (2003), but is confirming that at least one of the main assumptions, namely the pure luminosity evolution, which tends to broaden the peak, is not supported by the data, as definitely shown in next Chapter.

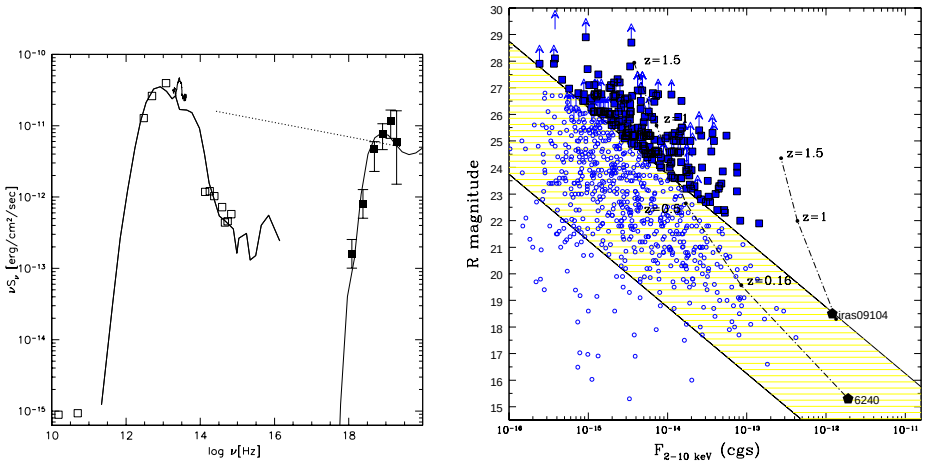

Figure 3.8 (*left panel*) The broad band spectral energy distribution of IRAS 09104+4109 (adapted from Franceschini et al. 2000). (*right panel*) The 2–10 keV flux versus the R band magnitude for a sample of `unconventional` AGN detected in the `HELLAS2XMM` survey (empty squares) and in deeper *Chandra* and XMM–*Newton* surveys (filled squares, see Comastri, Brusa & Mignoli 2003). Green and cyan symbols refer to objects with $f_X/f_{opt} > 1$ and `XBONGs`, respectively. The dash dotted lines represent the redshift tracks computed as described in the text. The filled symbols in the lower part of the diagram correspond to nearby heavily Compton thick AGN (Maiolino et al. 1998).

3.3.2 An approach based on the SED

In the following we try to further investigate the nature of high X/O sources assuming that they are powered by heavily obscured accretion. In order to properly address this issue it is important to point out that as long as the absorption column density does not exceed values of the order of "a few" $\times\ 10^{24}$ cm^{-2} (mildly Compton–thick) the high energy spectrum recovers at $E >$10–20 keV (see Fig. 3.8, left panel). At longer wavelengths the nuclear radiation can be completely blocked by dust and the optical infrared spectrum is dominated by the host galaxy starlight. There are several examples of mildly Compton thick sources in the local Universe discovered thanks to X–ray observations (see e.g. Maiolino et al. 2003 and the discussion in Chapter 3). The prototype of the former is NGC 6240 at $z = 0.0245$ (Vignati et al. 1999) discovered by BeppoSAX. Whether Compton thick AGN are common at high redshift is still debated (Fabian, Wilman & Crwaford, 2002) only a few sources have been reported to date (e.g. IRAS 09104+4109 at $z = 0.442$ Franceschini et al. 2000; IRAS F15307 at $z = 0.92$ Ogasaka et al. 1997, Iwasawa, Fabian & Ettori, 2001; CDFS_202 at z=3.7 Norman et al. 2002). As already noted, moving the SED of a mildly Compton thick object (Fig. 3.8, left panel) to progressively higher redshifts, the K–corrections in the optical and X–ray band work in the opposite direction and the optical to X–ray flux ratio changes in a non–linear way. We have computed the optical magnitude in the R band and the 2–10 keV X–ray flux which would be observed for

a source with the SED reported in the left panel of Fig. 3.8 from $z = 0$ to $z = 1.5$. The redshift tracks in the optical magnitude versus X–ray flux plane (Fig. 3.8, right panel) have been normalized to the observed X–ray flux and R magnitude of NGC 6240 and IRAS 09104+4109, characterized by a similar SED but different X–ray luminosities (about 3×10^{44} erg s^{-1} and 10^{46} erg s^{-1} respectively). The results clearly indicate that the observed high values of the X–ray to optical flux ratio are consistent with those expected by a population of high redshift, mildly Compton thick AGN with X–ray luminosities in the range log$L_X = 44 - 46$ erg s^{-1}. Thus, at the face value, this "toy" model shows that sources with X/O> 1 $can\ be$ mildly Compton thick, luminous AGN in the redshift range 0.5–1.5, but the approximations adopted appear to be too much simple to draw quantitative conclusions. Indeed, results from X–ray spectral analysis (see previous Sections) indicate that Compton thin absorption, rather than Compton thick is present in the majority of the high X/O. Moreover, from a statistical analysis of the sources in the CDFN, Bauer et al. (2003) placed a significant upper limit ($< 10\%$) on the fraction of Compton Thick sources.

3.3.3 X–ray constraints

Since its discovery by early X–ray observations, the fluorescent FeKα neutral iron emission line at 6.4 keV it is by now recognized to be an ubiquitous features in the high energy spectra of nearby Seyfert galaxies and an important diagnostic of the physical and dynamical status of the obscured, accreting gas (e.g. Tanaka et al. 1995). Moreover, given that the iron line is by far the strongest emission feature in the X–ray band, it can be used as a redshift indicator. In fact, an accurate (e.g. Δz=0.1, of the order or even better that the error associated to photometric techniques) redshift estimate can be achieved only if the counting statistic is such to allow a reliable detection of the emission feature and a reliable measure of its centroid energy.
With these caveats, it is clear that the CDFN 2 Ms observation constitutes the best dataset for a systematic search for redshifted iron lines in high X/O sources detected at the brightest fluxes (Civano, Comastri & Brusa 2004).

As an example I report here the detection of a highly significant emission line feature which is present around 3 keV in the spectrum of the unidentified $Chandra$ source CXOHDFN 123556.12+621219.1 ($F_{2-8keV} = 1.9 \times 10^{-14}$ erg cm^{-2} s^{-1}, R=23.7, X/O $\simeq$ 18; data from Alexander et al. 2003; Barger et al. 2003). The X–ray spectrum fitted with an absorbed power–law plus a neutral iron line is shown in the left panel of Fig. 3.9. The observed line energy corresponds to an X–ray redshift of z=1.14$^{+0.11}_{-0.04}$ (or slightly higher z=1.24 if the ionised 6.7 keV emission is assumed). There is also evidence of substantial intrinsic absorption with a column density $N_H \simeq 3 \times 10^{23}$ cm^{-2}; in the right panel of Fig. 3.9 the confidence contours of the intrinsic column density versus redshift are reported. Given its unabsorbed X–ray luminosity of about 10^{44} erg s^{-1} in the 2–10 keV band, this object could be classified

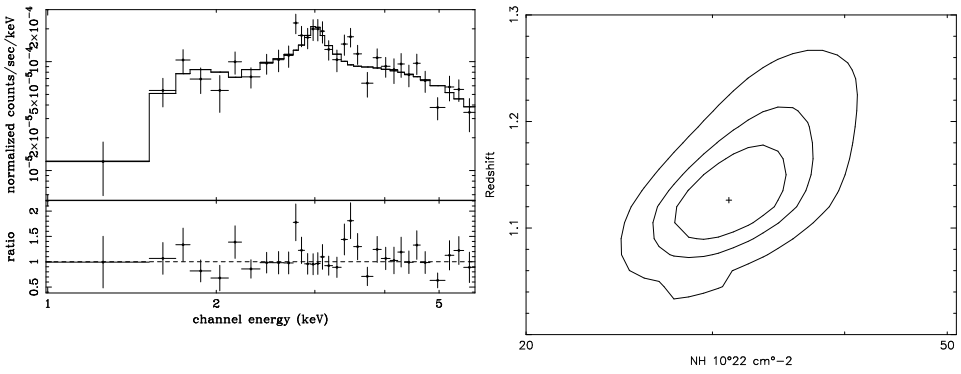

Figure 3.9 (*Left panel*): The X–ray spectrum of source CXOHDFN 123556.12+621219, fitted with an absorbed power–law plus a FeKα line and residuals of a power law fit to the *Chandra* X–ray spectrum of source CXOHDFN 123556.12+621219.1. *(Right panel)*: 68, 90 and 99% confidence contours of the intrinsic column density versus redshift

as an highly obscured, highly luminous Type 2 quasar.

Chapter 4

The evolution of the accretion in the Universe

The difficulty in the identification of optically faint X–ray sources, coupled with the small area covered, leads to a strong bias against high–redshift sources and renders the ultra-deep surveys alone inadequate to properly sample the redshift distribution and to build luminosity functions. To overcome this problem, in the previous Section, we have used the results obtained for a combined sample of 310 sources (70% with spectroscopic redshifts) from the HELLAS2XMM 1dF and deeper *Chandra* and XMM–*Newton* surveys (CDFN, SSA13, Lockman Hole), to statistically assign the luminosities, hence the redshifts, to the remaining 30% of the sources without optical spectroscopic identification.
This virtually "complete" sample is now used to derive the number and 2–10 keV luminosity densities of hard X-ray sources up to z$\sim$ 3 (Sect. 4.1), the contribution of AGN to the local Black Hole mass density (Sect. 4.2) and the spatial density of QSO2 (Sect. 4.3).

4.1 The evolution of hard X-ray selected sources

The number and luminosities densities have been computed from the combined sample described in Sect. 3.3.1 and in three luminosities bins: logL(2-10)=43-44, logL(2-10)=44-44.5 and logL(2-10)=44.5-46. The approach is rather similar to that followed by Cowie et al (2003), based on a combination of the CDFN and a ROSAT sample. Moreover, to properly sample the X–ray brightest fluxes in deriving the cosmological evolution of the number and luminosity densities of accretion dominated, hard X-ray selected sources, we have also included 66 sources from the HEAO1 A2 all sky survey (Grossan, 1992) with $F_{2-10keV} > 2 \times 10^{-11}$ erg cm^{-2} s^{-1}. The standard $1/V_{max}$ method (Schmidt 1968, Lilly et al. 1995, Cowie et al. 2003) has been adopted and a detailed description of all the possible biases due to the utilization of this method is reported in Fiore et al. (2003).

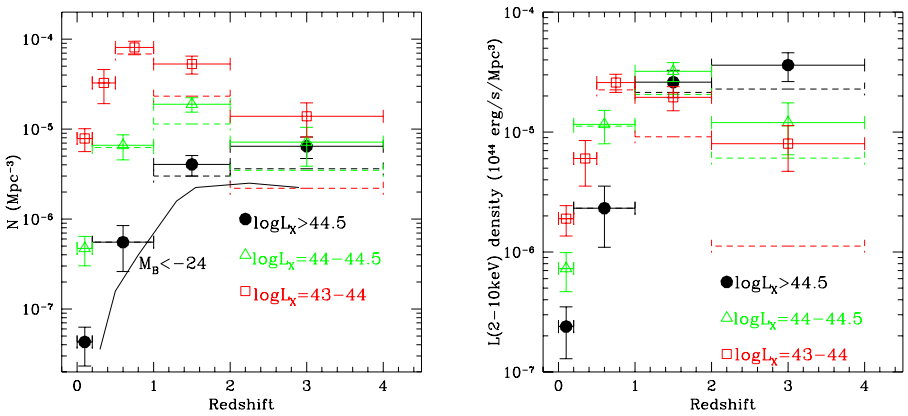

Figure 4.1 (*left panel*) The evolution of the number density of hard X-ray selected sources in three bins of luminosity: $\log L_{2-10keV}$=43-44 erg s^{-1} = empty squares; $\log L_{2-10keV}$=44-44.5 erg s^{-1} = empty triangles; $\log L_{2-10keV} >$ 44.5 erg s^{-1} = filled circles. Note that the z=2–4, logL(2-10)=43–44 bin is a lower limit, see the text for details. Dashed lines represent lower limits obtained using only the sources with measured redshift, see the text. The solid continuous curve represents the evolution of optically selected QSO more luminous than $M_B = -24$. Note as the shape of the solid curve is similar to the evolution of the luminous X-ray selected sources. (*right panel* The luminosity density of hard X-ray selected sources. Symbols are the same of left panel.

The number density of X–ray sources as a function of redshift and for the three luminosity bins is shown in Fig. 4.1 (left panel). The number density of luminous AGN increases by a factor ~ 100 up to z=2 and by a factor ~ 200 up to z$\sim$ 3. This behaviour is similar to that of luminous ($M_B < -24$) optically selected AGN (Hartwick & Shade, 1990, solid thick line in Fig. 4.1). Conversely, the number density of lower luminosity AGN increases between z=0 and z=1 by a factor ~ 13 and then it seems to decrease at high redshifts. However, it is important to note that for the z=2-4 bin the value inferred is actually a *lower limit*, because at the flux limit of the combined sample the objects with logL(2-10)<43.5 are not accessible at z>2 (see Fig. 3.5).
Right panel in Fig. 4.1 plots the evolution of the hard X-ray luminosity density. The luminosity density of lower luminosity AGN increases from z=0 to z$\sim$ 1.5 by a factor of ~ 18, and then stays about constant, while that of high luminosity AGN rises monotonically from z=0 to z$\sim$ 3 (quickly from z=0 to z=1.5 and then more gradually above this redshift) by a factor of more than two orders of magnitudes.

The different number and luminosity evolutions of low and high luminosity sources is confirmed if only the sources with a measured z are considered: in this case, the lower limits are plotted as dashed lines in both panels of Fig. 4.1. The limits are very close to the points up to z=1, indicating that up to this

redshift our determination of the number and luminosity density of both high and low luminosity AGN is highly reliable. For z>1 and logL(2-10)=43-44 erg s^{-1} the limits are much lower than the points, which are mostly determined following the statistical approach described in Sect. 3.3.1).

4.1.1 A Luminosity Dependent Density Evolution

The luminosity density at z<1 is dominated by low luminosity AGN, while (within the large statistical error bars and the uncertainty related to the statistical procedure adopted) at z>1 those of low and high luminosity AGN are comparable, and similar to that of low luminosity AGN at z=0.5-1. This implies an integrated luminosity density for logL(2-10)>43 of 4.6×10^{39} erg s^{-1} Mpc^{-3} at z=0.1–1 and 5.6×10^{39} erg s^{-1} Mpc^{-3} at z=2–4.
These results are qualitatively in agreement with those obtained by Cowie et al. (2003, see their Fig. 4). Quantitatively, though, we note that the integrated luminosity density here derived is higher than the value given by Cowie et al. ($\sim 2 \times 10^{39}$ erg s^{-1} Mpc^{-3} in each redshift bin), although within their uncertainty (a factor of ~ 3). This is probably due to the different prescriptions in computing luminosities (Cowie et al., 2003, do not correct for intrinsic absorption), and to the fact that deep but small area surveys probe mostly the flatter, low luminosity end of the AGN luminosity function at z<1-2, while larger area surveys, like the `HELLAS2XMM 1dF` sample, push the AGN selection to 3-10 times higher luminosities (see Fig. 3.5), up to and above L^*, which identifies the break in the luminosity function, whereabouts most of the contribution to its integral comes from. Moreover, the points and lower limits in each luminosity bin of Fig. 4.1 are, by construction, all *independent*, which make them easier to compare, unlike the upper limits in Fig. 4 of Cowie et al. (2003).

The *different* number and luminosity evolutions observed for different luminosity classes (Luminosity Dependent Density Evolution, LDDE) implies that luminous AGNs (quasars) formed in earlier epochs than less luminous AGNs (such as Seyfert galaxies), consistent with the claims by Hasinger et al. (2003) obtained from luminous, soft X–ray selected sources. Moreover, the space density of low–luminosity (e.g. $L_X < 10^{44.5}$ erg s^{-1}) X–ray sources at $z < 1$ is more than two order of magnitude larger than that of high–luminosity (e.g. $L_X > 10^{44.5}$ erg s^{-1}) ones, suggesting that low–luminosity sources are subject to a very fast evolution of their space density at z<1.
A LDDE model in which the cutoff redshift increases with the luminosity helps to reduce the discrepancy between the observed redshift distributions and that predicted in standard AGN synthesis models (Ueda et al. 2003). The same model provide also a relatively good agreement between the observed and predicted absorption distributions, by assuming that the fraction of absorbed ($N_H > 10^{22}$ cm^{-2}) sources is a decreasing function of the X–ray luminosity (see Fig. 7 in Ueda et al. 2003). A natural consequence is that *low–luminosity, obscured AGN dominate the number and luminosity densities at* $z < 1$.

As a final remark, it has been proposed that the growth and light-up of supermassive black holes (SMBH) in the galaxy nuclei is triggered by galaxy encounters (e.g. Cavaliere & Vittorini 2000). On this basis, and in the framework of the hierarchical bottom-up scenario, Menci et al. (2004) have recently developed a semi–analytic model that recovers a remarkable agreement with the observations, especially for brighter sources, in a wide range of redshifts. In particular, the model reproduce rather naturally the steep evolution which is observed in the highly luminous quasar population. The same model slightly over predicts (a factor ~ 2) the number of faint X–ray sources with log(2-10)=43-44 and logL(2-10keV)=44-44.5 in the redshift bins z=1-2 and z=2-4, respectively. Despite the uncertain origin of this overprediction, it is interesting to note that from both observations and theory the number and luminosity densities of lower luminosity AGN evolve up to z=1 and possibly decrease at z>2 with a behaviour similar to that observed in galaxies in which the star-formation is ongoing (Lilly et al. 1995, Madau et al. 1996, 1998, Fontana et al. 1999). The above picture thus naturally explains the parallel evolution of BH accretion and star formation in spheroidal systems, as originally discussed by Monaco, Salucci & Danese (2000) and Granato et al. (2001), and supported by recent works (see e.g. Haiman, Ciotti & Ostriker 2003)

4.2 Black Holes mass density

As already pointed out in the Introduction, it is possible to directly constrain the formation history of super massive black holes (SMBHs) in galactic centers making use of the Soltan's argument and assuming that the energy density recorded in the XRB is a good indicator of the overall accretion. Here I recall Eq. 1.3:

$$\rho_\bullet = \frac{1}{\eta c^2}\frac{4\pi k_{bol}}{c}(1+\langle z\rangle)I_0 \qquad (4.1)$$

where I_0 is the XRB unabsorbed intensity in the 2–10 keV band, η is the efficiency of turning accretion energy into radiated energy, $\langle z\rangle$ is the mean redshift of the sources responsible for the XRB, and k_{bol} is the bolometric correction which relates the total emissivity to the emissivity in the X–ray band. For the latter it is important to note that recent results on high–redshift quasars have shown that the overall X–ray to optical spectral slope (α_{ox}, generally measured between 2500 Å and 2 keV, e.g. Tananbaum et al. 1979) and the corresponding k_{bol}, is a function of the AGN luminosity, low luminosity objects having a lower k_{bol} (Vignali et al. 2003).
The results on the evolution of hard X–ray sources, described in the previous Sect., affect both the values of $\langle z\rangle$ and k_{bol}: the evidences that obscured accretion has a faster evolution than unobscured accretion and that low–luminosity AGN contribute to the observed luminosity density $at\ least$ as the high–luminosity ones, in each redshift bin, imply that both the $\langle z\rangle$ and the average k_{bol} should be lower than that observed for luminous QSOs. As a consequence, the estimate of the integrated AGN black hole mass density

Table 4.1: Summary of Mass Densities in SMBHs

References	$\rho_\bullet$ (10^5 $M_\odot$ Mpc^{-3})
XRB spectrum – pre Chandra/XMM surveys	
Fabian & Iwasawa 1999	6.0
Elvis, Risaliti & Zamorani 2002	7.5-16.8
XRB spectrum – post Chandra/XMM surveys	
Fabian 2003	~ 4
Cowie et al. 2003	~ 2
HELLAS2XMM(Fiore et al. 2003)	4-6
Hard X-ray LF	
Marconi et al. 2004	~ 3.5
Bright QSOs optical counts	
Yu & Tremaine 2002	2.2
Local BH mass density	
Ferrarese 2002	4-5
Marconi et al. 2004	3.2-6.8

has been significantly reduced with respect to previous estimates (Fabian & Iwasawa 1999; Elvis, Risaliti & Zamorani 2002; see Table 4.2). In particular, Fabian (2003) simply assuming the lower $\langle z \rangle$ observed in the deep surveys ($\langle z \rangle \sim 0.7$, Barger at al. 2003; Hasinger 2003) and a lower k_{bol} for low–luminosity AGN with respect to that assumed for unobscured QSO, reported an updated estimate of $\rho_\bullet \sim 4 \times 10^5$ $M_\odot$ Mpc^{-3}.

A more detailed calculation of the BH mass density due to the accretion could be performed by integrating the AGN luminosity function ($\phi(L)$) over the cosmic time:

$$\rho_\bullet = \frac{k_{bol}}{\eta c^2} \int \frac{dt}{dz} dz \int L \phi(L) dL \qquad (4.2)$$

This approach requires the knowledge of the luminosity function of the entire AGN population; given that current hard X-rays surveys are less sensitive to obscuration than optical and soft X-ray ones, they probe undoubtedly the largest fraction of the whole AGN population and the $\rho_\bullet$ derived by integrating hard X–ray luminosity function can be considered representative of the total mass accreted in the AGN phase. Marconi et al. (2004) have recently discussed in great details all the assumptions in the calculation of the BH mass density, and adopting the so–far best–determined hard X–ray luminosity function (Ueda et al. 2003) they derive $\rho_\bullet \sim 3.5 \times 10^5$ $M_\odot$ Mpc^{-3}. As a comparison, using bright optical quasars only, and $\eta = 0.1$, Yu & Tremaine (2002) obtain $\rho_\bullet = 2.2 \times 10^5$ $M_\odot$ Mpc^{-3}, and a similar value is recovered from soft X–selected AGN samples (see Ferrarese 2002).

Following the same reasoning of Cowie et al. (2003), the results described in Sect. 4.1 on the integrated luminosity imply a present universal supermassive black hole density of $\rho_\bullet = 4 - 5 \times 10^5$ $M_\odot$ Mpc^{-3}, about 2 times higher than

that estimated from optical counts and consistent with that obtained by Fabian (2003) and Marconi et al. (2004).

The value of $\rho_\bullet$ can then be compared with that measured from local galaxies using the $M_\bullet - \sigma$ relation (Ferrarese & Merritt 2000; Gebhardt et al. 2000). A summary of the results of various determination of the black hole mass density has been recently discussed by Fabian (2003) and Comastri (2003) and is reported in Table 4.2. Although the various estimates agree each other within a factor 2–3, it has been pointed out (Fabian 2003) that taking some of the values at the face value could have important astrophysical consequences.
The values obtained following the results of hard X–ray surveys and adopting a "standard" efficiency ($\eta \simeq 0.1$) are consistent with the estimates based on the $M_\bullet$–σ relation (Ferrarese et al. 2002). In particular, hard X–ray surveys have probed that obscured and unobscured AGNs together contribute $\sim 4 - 5 \times 10^5$ $M_\odot$Mpc^{-3}; Type 2 quasars and Compton-thick objects may contribute up to 10^5 $M_\odot$Mpc^{-3} (Fabian 2003), but no more unless direct determinations from the $M_\bullet - \sigma$ relation seriously underestimate the local black hole mass density, or unless most massive black holes are rapidly spinning (Elvis, Risaliti & Zamorani 2002).
These results also provide robust evidences that obscured and unobscured accretion account for a comparable fraction ($\sim$50%) of the total BH mass density. The lower redshift and luminosity of most obscured AGNs, combined with the results that they make about half of the local BH mass density, mean that, although they dominate the number density at all redshifts (Fig. 4.1) and the absorption-corrected intensity of the X-ray background (by a factor of about 3 over unobscured objects, see Fabian & Iwasawa 1999; Fabian 2003), obscured accretion probably dominates the growth of black holes with masses below a few times 10^8 $M_\odot$, whereas optically bright quasars dominate at higher masses.

Finally, the fact that the locally inferred black hole mass density appears to be broadly consistent with the mass accreted during the AGN activity, strongly supports the idea that the nuclear activity, the growth of the black holes and spheroid formation are all closely linked. Interestingly, theoretical models of BH growth and activity in a ΛCDM Universe predict $\rho_\bullet$=$2 - 4 \times 10^5$ $M_\odot$ Mpc^{-3} (Di Matteo et al. 2003), in between the above discussed observations.

4.3 The link between QSO2, high X/O and EROs

As already discussed in the Introduction, a population of high–luminosity highly obscured Quasars (QSO2) are necessary to reproduce the 2–10 keV source counts predicted by standard AGN synthesis models at relatively bright fluxes (Gilli et al. 2001; Comastri et al. 2001). Despite intensive optical searches, these narrow–line high–redshift objects appeared to be elusive, with only a handful of objects reported in literature (e.g., Stern et al. 2002;

Norman et al. 2002; Mainieri et al. 2002), suggesting a space density and evolution different from that expected from unified schemes.
However, a few considerations appear appropriate. As already pointed out, the small area sampled in ultra deep survey leds to a strong bias against high–luminosity objects, and in particular against QSO2. Optical spectroscopy of sources in the HELLAS2XMM 1dF selected on a larger area at bright fluxes have indeed revealed several examples of high–redshift, narrow–line objects (see Table 1.2 and 3.1). Moreover, at the faint fluxes/magnitudes of deep surveys the optical identifications of these objects (for which no continuum emission is expected) is very difficult, unless one of the strong emission lines is present in the optical spectrum. However, the redshift and corresponding intrinsic X–ray column densities and luminosities, derived for the sources with high X/O, through different approaches, indicate that they are at high redshift and that heavy obscuration is almost ubiquitous (see Sect. 3.2 and 3.3). Finally, the existence of of X–ray absorbed BL QSOs show that X–ray Type 2 QSO *are not necessary* the high–luminosity counterparts of Seyfert 2 (see Sect. 2.1). A reliable estimate of the fraction of QSO2 has tehrefore to take into account all the indications outlined above.
Combining all the results presented in the previous Chapters, it has been possible to derive the fraction of highly obscured high luminosity QSO in the HELLAS2XMM 1dF sample. From Table 1.2 the fraction of sources with $N_H > 10^{22}$ cm^{-2} and $L_X > 10^{44}$ among identified objects is 28%, and rises up to about 40% when accounting also for unidentified sources (see Perola et al. 2004). This fraction can be translated, taking into account the sky coverage, into a surface density of highly obscured QSOs of ~ 48 deg^{-2}, at the flux limit of $\sim 10^{-14}$ erg cm^{-2} s^{-1} of the HELLAS2XMM 1dF sample, in relatively good agreement with that predicted by baseline AGN synthesis models (47 deg^{-2} at 2×10^{-14} erg cm^{-2} s^{-1}, Comastri 1999).
The results from Ueda et al. (2003) suggest that the fraction of absorbed sources is dependent from the luminosity; as a consequence it has been pointed out that the fraction of QSO2 can be lower (~ 30%, see Fig. 7 in Ueda et al. 2003) than that originally postulated, but still consistent with the results derived from the HELLAS2XMM 1dF sample.

In the previous Chapters I have also shown that there are compelling evidences that highly obscured QSO generally exhibit red optical to near–infrared colors. In particular, near infrared observations of X–ray sources selected on the basis of their high X–ray to optical flux ratio (see Sect. 3.2) have shown that the hosts of obscured X–ray sources are among the most massive spheroids at these redshifts. If the evolution of luminous AGN as suggested by e.g. Franceschini et al. (1999) and Granato et al. (2001) follow that of spheroids, it is possible that the radiation and the strong winds produced by a powerful AGN present in the massive galaxy may help inhibiting the star-formation in these galaxies, which therefore would have red colors.
The link between high X/O, QSO2 and the population of Extremely Red

Objects (EROs, R-K>5) therefore, can be used to address the issue of elliptical galaxy formation and the expected co-evolution with the black-hole accretion.
Systematic studies of the relationship between EROs and QSO2 are needed for a detailed statistical and comprehensive analyses and to *quantitatively* investigate the link between the formation of massive elliptical galaxies and the onset of AGN activity.

Chapter 5

Hard X–ray observations of Extremely Red Objects

Extremely Red Objects (EROs, R−K>5, Elston et al. 1988) detected in near–infrared ground–based imaging have the colors expected for high-z passive ellipticals and can be used as tracers of distant and old spheroids in order to understand if the present-day massive ellipticals formed at early cosmological epochs ($z > 2 - 3$) through a relatively short episode of intense star formation followed by a passive and pure luminosity evolution (PLE), or if they built up more recently through the hierarchical merging of pre-existing disk galaxies. However, several independent evidences have clearly pointed out that EROs constitute a heterogenous class of extragalactic sources; therefore, the relative fraction of the different subclasses among the ERO population is a key parameter in the study of the galaxy evolution and can constrain models which link the formation of massive elliptical galaxies and the onset of AGN activity (Granato et al. 2001; Roche, Dunlop & Almaini 2003).
Deep VLT spectroscopy of a sample of EROs from the $K20$ survey (Cimatti et al. 2002a) has shown that the ERO population is nearly equally made by old, passively evolving systems and dusty star–forming galaxies over a similar range of redshift ($z_{mean} \simeq 1$ for both the classes). Similar results have been recently obtained also by Yan, Thompson & Soifer (2004). A significant fraction of EROs may also be higher-z starbursts (e.g. HR–10, Cimatti et al. 1998) and AGN strongly reddened by dust extinction (e.g. Pierre et al. 2001).
First results suggested that the AGN population among EROs, although not dominant, shares the same X–ray properties of high luminosity, highly obscured AGN, i.e. they are characterized by X–ray column densities $N_H > 10^{22}$ cm^{-2} (Mainieri et al., 2002; Alexander et al. 2002).

In order to assess what is the fraction of AGN among near–infrared selected EROs, we have started an extensive program of multiwavelength observations

of the largest sample of EROs available to date (∼500 sources), selected in a contiguous area over a ~ 700 arcmin^2 field (the "Daddi field", Daddi et al. 2000) down to a magnitude limit of K=19.2 (@SOFI/NTT). This field is covered by deep optical photometry (R@WHT and B,I,z@Subaru). We have obtained a total of 100 ks observation with XMM–*Newton*; the moderate–deep exposure, high energy throughput of XMM–*Newton* and the large field of view are well–suited to detect AGN among EROs at the bright X–ray fluxes, on a statistically significant sample. In this framework, the same field will be imaged with *Chandra* in July 2004 and spectroscopic VIMOS observations are on–going.
The XMM–*Newton* data and the identification process is described in Sect. 5.1, while the fraction, optical and X–ray properties of X–ray detected EROs are presented in the following Sections and compared with those of hard X–ray sources with similar R-K colors and QSO2. A selection criterion to pick up QSO2 on the basis of the observed optical, near–infrared and X–ray fluxes is proposed (Sect. 5.5).

5.1 Multiwavelength data and X–ray sources identification

5.1.1 Optical and Near–Infrared data

The near infrared sample of EROs was selected by Daddi et al. (2000) over ~ 700 arcmin^2, at moderately deep K levels. To date, this study constitutes the largest survey of EROs performed at the limiting magnitude of $Ks < 19.2$ (complete down to K_s=18.8 on the whole area, and down to K_s=19.2 in a deeper area of ~ 450 arcmin^2) and R<26.2 (complete on the entire area), more than a factor of four larger than other previous surveys at the same limiting magnitudes (e.g. Thompson et al. 1999; Miyazaki et al. 2003).
The Ks observations were made with the ESO NTT 3.5m telescope in La Silla, while the R-band data were taken with the 4.2m William Herschel Telescope on La Palma.
Extremely Red Objects in the "Daddi Field" were selected from a 5σ source catalog in the Ks band and with the selection criterion $R - Ks > 5$. A total of ~ 500 EROs are included in this "reference EROs sample". All the relevant details on optical and near–infrared data reduction, and on the EROs selection, can be found in Daddi et al. (2000).
The same field has been recently observed in the z and B bands at very deep limiting magnitudes ($z_{AB} \sim 26$ and $B_{AB} \sim 26$, respectively) with the Suprime-CAM at SUBARU (Kisato, Arimoto et al. in preparation).

5.1.2 X-rays data

The "Daddi Field" was observed with XMM–*Newton* on August 3, 2001 for a nominal exposure time of 50 ks. A second observation was taken two years later, splitted in two parts (August, 22, 2003 and September 16, 2003), for a total exposure time of ~ 60 ks.

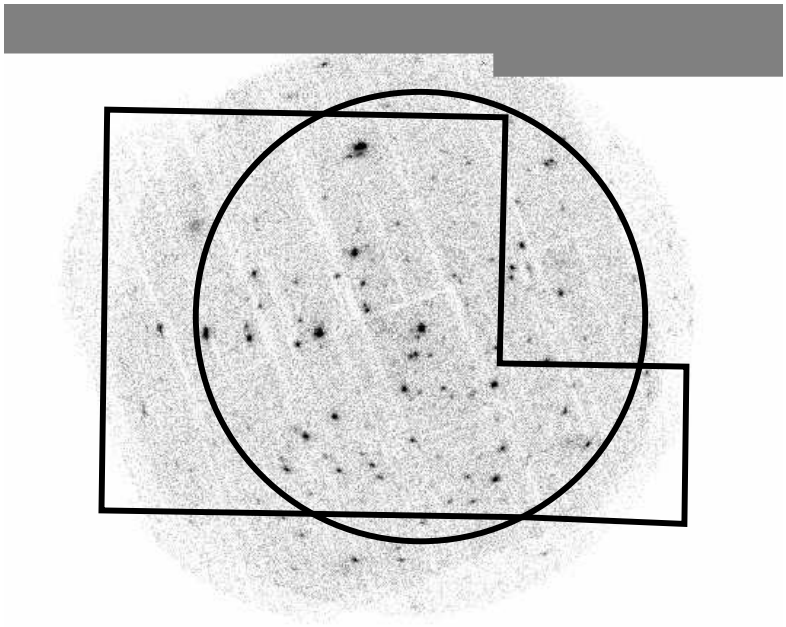

Figure 5.1 X–ray image (grey scale) with superimposed the 11 arcmin radius circle of the X–ray analysis and the deepest region (445 arcmin^2) in the K-band (polygon).

All the EPIC cameras operated in full-frame and were equipped with the "Thin" filter, which is usually employed in the observations of faint sources*. The three XMM–*Newton* datasets were reduced with version 5.4 of the XMM SAS; the latest, relevant calibration products were downloaded from the XMM–*Newton* web-page†. The raw *pn* and *MOS* Observations Data Files (ODF) were processed using the SAS tasks `emproc` and `epproc` to produce calibrated event lists. Only events with pattern 0-4 (single and double) for the *pn* and 0-12 (similar to ASCA event grades 0-4) for the MOS cameras were selected. All the event files were cleaned up from hot pixels and soft proton flares (Brusa et al. 2004, see also Sect. 1.1.1).
The excellent *relative* astrometry between the three cameras in each observation (within 1″, well below their PSF of $\sim 6''$), allowed us to merge the *MOS* and *pn* images in each observation, in order to increase the signal to noise ratio and to reach fainter X–ray fluxes. Moreover, taking into account the *absolute* astrometry between the two observations, the counting statistic has been further improved by summing all the available datasets. The resulting total exposure time for the *pn* is ~ 80 ks, and is only slightly lower for the *MOS* instruments.

I have limited the X–ray analysis in a circular region of eleven arcmin radius from the point of maximum exposure (centered at α=$14^h49^m25^s$ and

*http://xmm.vilspa.esa.es/external/xmm_user_support/documentation/index.shtml
†http://xmm.vilspa.esa.es/external/xmm_sw_cal/calib/index.shtml

δ=09^{o}00$'$13$''$), where the effective exposure is dropped to $\sim 50\%$. The total area analysed in the present work is therefore of ~ 380 arcmin^2 and covers the region with the deepest (and uniform) coverage in the optical bands and in most of the near–infrared. The pattern of the X–ray and optical/near–infrared data is shown in Fig. 5.1: the 11 arcmin radius circle and the deepest K_s band region (polygon) are superimposed on the 0.5-10 keV band X–ray image.
The accurate detection algorithm developed for the HELLAS2XMM survey (Baldi et al. 2002) was run on the 0.5–10 keV cleaned events, in order to create a list of candidate sources. I then computed the probability that the detected counts originate from poissonian background fluctuations: 96 sources were detected above a detection threshold of p=2×10^{-5} (that corresponds to less than 1 spurious X–ray detection). The count rate to flux conversion factor was derived assuming a power law with photon index Γ=1.7, absorbed by the Galactic column density in the direction of the Daddi Field (N_H=5×10^{20} cm^{-2}, Dickey & Lockman 1990), and weighted by the effective exposure times of the different EPIC cameras.The uncertainty in the derived fluxes is $< 15\%$ for $\Delta\Gamma = \pm0.5$ and N_H up to 10^{21}. The corresponding limiting flux is $\sim 2 \times 10^{-15}$ erg cm^{-2} s^{-1}at the aim point, and is a factor of ~ 1.5 higher at the edge of the selected area where the net exposure is ~ 40 ks.
The same detection algorithm was also run in the soft 0.5–2 keV (82 sources detected) and hard 2–10 keV (56 sources) energy bands, in order to characterize the average spectral properties of the sources in our sample using the hardness–ratio (HR) technique.

Table 5.1 lists all the relevant X–ray properties of the detected sources (namely: Xid, X–ray coordinates, 0.5-10 keV flux, hard and soft counts plus associated errors).

5.1.3 X–ray sources identification

Optical and near infrared photometry is available for 90 out of 96 X–ray sources detected in the full band, given that the regions around bright stars or defects in the R, z and/or Ks band images were masked.
The X–ray centroids have been astrometrically calibrated with respect to the optical positions of three bright quasars in the field (Hall et al. 2000): an average shift of $\sim 2''$ (Δ(Ra)=1.47$''$; Δ(dec)=$-$1.29$''$) has been applied.
At first, the X–ray source list has been cross–correlated with the K–band and z–band catalogs. In order to accommodate any residual systematics in the astrometric calibration of the EPIC images and to fully account for the uncertainties in the X–ray source positional accuracy for faint sources (e.g., sources with <100 cts, see Sect. 1.2.1 for further discussion), I have searched for optical counterparts for all the X–ray sources within a conservative matching radius of 5$''$: 167 (80) counterparts in the z (Ks) band were found in 90 X–ray error-circles. The difference in the number of possible counterparts in the two bands clearly reflects the different depth of

the optical and near–infrared images. In particular, using the z catalog, and a fixed searching radius, substantial source confusion may be introduced: on the basis of the integral counts from the z catalog, on average 1 galaxy with z< 25 is expected just by chance in the 5″ error–box (80 arcsec^2).
We therefore decided to use the "likelihood ratio" (LR) technique, defined as the ratio between the probability that the source is the correct identification and the corresponding probability for a background, unrelated object (Sutherland & Saunders 1992), defined as:

$$LR = \frac{q(m)f(r)}{n(m)} \tag{5.1}$$

where $f(r)$ is the probability distribution function of the positional errors, $n(m)$ is the surface density of background objects with magnitude m, and $q(m)$ is the expected probability distribution as a function magnitude of the optical counterparts. The $q(m)$ distribution is normalized as $\int^{m_{faint}} q(m)dm = Q$, where Q is the expected fraction of X–ray sources with an optical counterpart brighter than m_{faint}; m_{faint} can be either the limiting magnitude of the optical data or the magnitude beyond which the surface density of background objects becomes so high that no reliable "statistical" identification is possible.
For the calculation of the LR parameters we have followed the procedure described by Ciliegi et al. (2003); more specifically in order to maximize the statistical significance of the over density due to the presence of the optical counterparts, we have adopted a radius of 3″ for the estimate of the $q(m)$ distribution. A large fraction of the possible counterparts are expected to be included within such radius.
As an example, Fig. 5.2 shows the observed magnitude distribution of the optical objects detected in the z band within a radius if 3″ around each X–ray sources (solid histogram), together with the expected distribution of background objects in the same area (dashed histogram). The difference between these two distributions (dot-dot-dot dashed histogram) is the expected magnitude distribution of the optical counterparts. The smooth curve fitted to this histogram (dot-dot-dot dashed line) has been used as input in the likelihood calculation. Figure 5.2 shows that the observed number of objects is well above the background up to $z \sim 24$. The small number of detected objects at $z > 24$ is probably due to the difficulty of detecting faint objects close to the numerous and much brighter optical counterparts of the X–ray sources. For these reasons we have adopted $z_{faint} \sim 24$ in our likelihood calculation; all sources fainter than this limit will have $q(m)=0$ by definition, and the corresponding LR=0.
Then, the LR value for all the optical (z) and near–infrared (Ks) candidates has been computed. The next step is to choose the best threshold value for LR ($L_{\rm th}$) to discriminate between spurious and real identifications. The choice of $L_{\rm th}$ depends on two factors: first, it should be small enough to avoid missing many real identifications and having a rather incomplete sample. Secondly, $L_{\rm th}$ should be large enough to keep the number of spurious identifications as low as possible and to increase the reliability. A

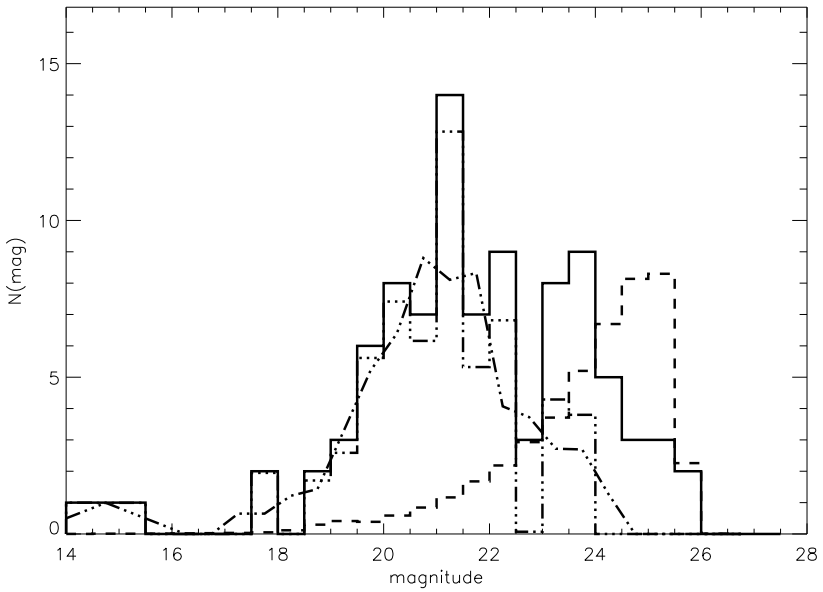

Figure 5.2 Observed magnitude distribution of the optical objects detected in the z band within a radius if 3″ around each X–ray sources (solid histogram), together with the expected distribution of background objects in the same area (dashed histogram). The difference between these two distributions (dot-dot-dot dashed histogram) is the expected magnitude distribution of the optical counterparts. The smooth curve fitted to this histogram (dot-dot-dot dashed line) has been used as input in the likelihood calculation.

LR threshold of $L_{\rm th}$=0.25 in both bands has been adopted, turning out to be the value which maximizes the sum of sample reliability and completeness (see Ciliegi et al. 2003 for further details). This threshold, *a posteriori*, led to an estimated percentage of secure X–ray to optical or near–infrared associations of the order of $\sim 85\%$ (see below).
The information derived in the two bands has been then combined: all the sources (73) with the highest LR$> L_{\rm th}$ in both the z and K bands have been defined *secure* identifications. In addition, four X–ray sources have a unique, very faint (z$\gtrsim 24$) optical counterpart within 1.3″ (xid#362, xid#77, xid#179, and xid#244)[‡]; by construction their associated likelihood ratio is zero. Given that less than one galaxy with $24 \lesssim z \lesssim 25$ is expected just by chance in the seventeen 1.3″ error–boxes without a secure identification, we tentatively consider also these four sources as likely identifications. Seventy–seven out of 90 X–ray sources have been therefore securely associated to an optical and/or near–infrared counterpart and are reported in the first part of Table 5.2; as expected, the majority of them (90%, 71/77) have $\Delta(X-O) < 3''$.
In other 5 cases the LR of the possible counterparts are not such to unambiguously determine which one is the most likely identification (second

[‡]and no other optical counterpart up to 5″

part of Table 5.2). Finally, in the remaining 8 cases the possible counterparts have on average fainter optical magnitude, none of the candidates has LR> $L_{\rm th}$, and they lie on average at $\Delta(X-O) > 3''$ (bottom part of Table 5.2). This can be the case if the source is very faint and undetected in the optical bands (see e.g. Koekemoer et al. 2004), or if the X–ray emission originates from a group of galaxies. A *Chandra* detection (with ten times smaller error–boxes) will definitively discriminate between the possible counterparts.

In Table 5.2 are reported, for each X–ray source, the distance between the X–ray and optical counterparts (or candidates), the total z_{AB} magnitude, the K_{AB} magnitude and the LR in both the optical and near–infrared band. In the following, I will consider only the EROs sources. All the objects with (R-K)$_{AB} > 3.35$ (that corresponds to the "classic" R-K> 5 in the Vega system) and associated with X–ray sources are reported in Table 5.3 and 5.4: from the likelihood analysis 10 X–ray sources are securely associated with EROs in the "reference" (i.e. 5σ) ERO sample: 5 detected in both the hard and soft bands, three only in the hard and 2 only in the soft.

5.2 Fraction of X–ray detected EROs

The fraction of X–ray detected EROs among optically selected EROs samples is strongly dependent on the limiting fluxes reached in both the X–ray and near–infrared bands. 312 objects of the "reference EROs sample" (see Sect. 5.1.1) fall within the XMM–*Newton* area analysed in this work. Ten of them are individually detected in the X–rays. The fraction of X–ray detected (i.e. AGN–powered) EROs at K=19.2 (that corresponds to K=21.0 in the AB system) and F$_{0.5-10keV} \sim 2 \times 10^{-15}$ erg cm^{-2} s^{-1}is therefore $\sim$ 3% (10/312).

Several systematic X–ray studies of optically selected EROs samples have been already reported in the literature. Roche et al. (2003) estimated the fraction of X–ray detected EROs in the CDFS/GOODS area down to Ks=21.5: about 8% of the Ks-selected EROs are X–ray sources at X–ray fluxes of $\sim 4 \times 10^{-16}$ erg cm^{-2} s^{-1} in the 2–10 keV band. This can be considered as a conservative estimate of the AGN fraction among EROs, given that the limiting flux corresponds to an X–ray luminosity L$_X \gtrsim 10^{42}$ erg cm^{-2} s^{-1} for an average redshift z=1. This fraction rises up to 21% (6/29) at K$\lesssim$20.1 and limiting fluxes in the soft band of the CDFN observation (Alexander et al. 2002). It is important to note that starbursts and normal elliptical galaxies start to be detected at the faintest (soft) X–ray fluxes: a conservative estimate of the fraction of AGN powered EROs in the CDFN based on the hard X–ray detection (see also next Sect.) suggests a slightly lower value (e.g. 14% in the CDFN, see Alexander et al. 2002). It is therefore unlikely that the fraction of AGN powered EROs is much higher than the value above (i.e., Vignali et al. 2002; see also Next Chapter).

With XMM–*Newton* and *Chandra* surveys, the fraction of optical

counterparts with extremely red colors has significantly increased when compared to the first examples of EROs found in ROSAT observations (Lehmann et al. 2001). Referring only to the hard X–ray selected sample, our results also imply that $\sim$ 16% (8/50) of the XMM–*Newton* sources exhibit R-K>5 colors; this fraction increases to $\sim$20% (10/50) if we include also sources detected in the Ks image down to the 3σ level (reported in the bottom part of Table 5.3).
Our results are in agreement with those reported by Mainieri et al. (2002) in the Lockman Hole: 12/53 ($\sim$23%) of hard X–ray selected sources are associated with EROs, at comparable limiting near–infrared and X–ray fluxes of the present sample.

5.3 X–ray to optical properties of AGN EROs

In order to investigate the nature of hard X–ray selected EROs and the link between faint hard X–ray sources and the ERO population, I have collected all the literature multiwavelength data available to date for EROs individually detected in the X–rays. More specifically:

- 1) Seventy EROs detected in the 2–8 keV band in the *Chandra* Deep Field North observation, from the Barger et al. (2003) catalog and adopting a R-K$>$5 selection criterion; 9 with spectroscopic redshift and 25 with photometric estimates;
- 2) Twenty two hard X–ray selected EROs in the CDFS, from Szokoly et al. (2004); 8 with spectroscopic redshift;
- 3) Twelve EROs detected in the hard (2–10 keV) band in the XMM–*Newton* Lockman Hole observation (Mainieri et al. 2002), 2 with spectroscopic redshifts and 3 with photometric redshift;
- 4) Five additional hard X-ray selected EROs available in the literature (Cowie et al. 2001, Crawford et al. 2001, Brusa et al. 2003, Willott et al. 2003) 4 with spectroscopic and 1 with photometric redshifts.

This comparison sample consists of 111 EROs, including the 10 EROs discussed in the present work and detected in the 2–10 keV band; for 52/111 photometric or spectroscopic redshifts are available. This sample is by no means homogeneous (e.g. the selection criteria for EROs are slightly different, R-K>5 or I-K>4 depending on the authors; or the K–coverage is not complete), but could be considered representative of EROs individually detected in the X–rays.
The R–band magnitudes plotted versus the hard X–ray fluxes are reported in Fig. 5.3 (left panel). The present EROs sample spans a wide range of optical and X–ray fluxes, and the observed X–ray to optical properties clearly confirm that these objects show an average ratio between the X–ray and optical fluxes around X/O$\simeq$10. About half of the sources therefore belong to the high X/O population described in Chapter 3. In particular, these results are in

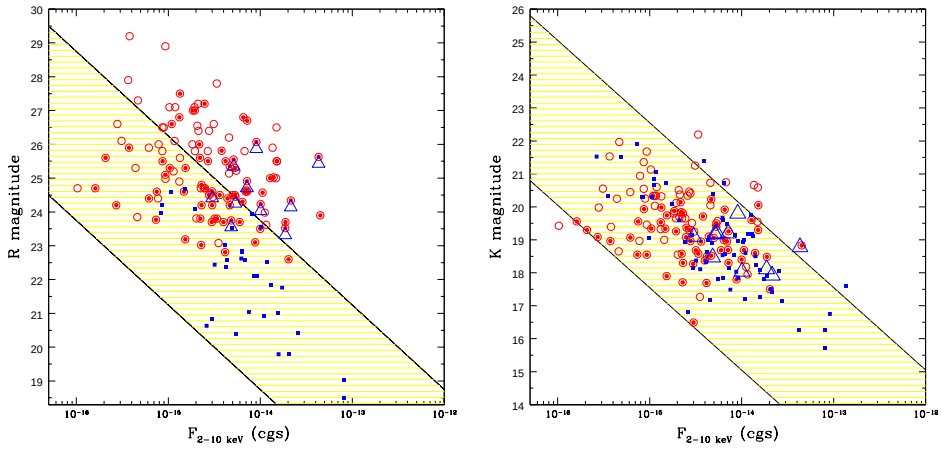

Figure 5.3 *left panel:* R–band magnitude vs. hard X–ray flux for EROs, serendipitously detected in hard X–ray surveys. Large open triangles are the 10 hard X–ray selected EROs in this work. Open circles correspond to the EROs in "comparison sample"; dot–filled circles are objects with redshifts (see text for details). As a comparison, BL AGN detected in the CDFS and CDFN surveys are also reported as small squares. The shaded region is that defined in the Introduction. *right panel:* the same plot but in the K–band.

agreement with the findings described in Sect. 3.2: the sources selected in the HELLAS2XMM survey on the basis of their high X/O have been detected at bright Ks fluxes (Ks <19) and have very red colors ($R-K>5$).
Such a high X–ray–to–optical flux ratio in these objects is mostly due the R-K> 5 selection, that privilege optically faint sources. Indeed, when the K magnitude vs. X–ray flux is considered, the EROs are indistinguishable from the overall QSO population: a linear ($f_X/f_K \sim 1$) correlation, similar to the one observed in the optical band for broad line objects, is recovered for both EROs and QSO, suggesting that the observed infrared emission is well correlated with the X–ray one and, therefore, with the central engine (see Fig. 5.3, right panel).

5.3.1 Optical to near–infrared colors

Thanks to the multiwavelength coverage of the present sample, it is possible to investigate the broad–band properties of X–ray detected EROs and to compare them with those of the overall X–ray and near–infrared populations.

In Fig. 5.4 the $(z-K)_{AB}$ vs. the $(B-z)_{AB}$ colors of both K selected (crosses) and X–ray selected (blue circles) objects are reported. Objects associated with 3σ selected EROs (i.e. all the sources in Tables 5.3 and 5.4) are marked in red. Interestingly, all the X–ray detected EROs are clearly separated from the overall X–ray source population; the same is not true for the near–infrared selected population: many X–ray undetected EROs and objects with R-K< 5 occupy a similar region in this colour–colour plane (see the area at $(z-K)_{AB} \sim 1.5-2.0$ and $(B-z)_{AB} \sim 3.5-5.0$).

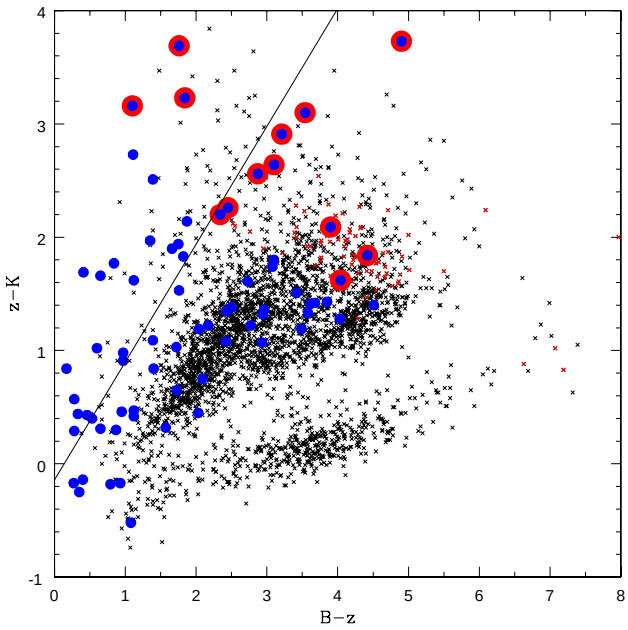

Figure 5.4 Two colors diagram $(B-z)_{AB}$ vs. the $(z-K)_{AB}$. X–ray sources are marked with blue circles, X–ray detected EROs are encircled in big red circles. Black (red) crosses are the K–selected (EROs) field sources. The straight line has $(z-K)_{AB} \sim (B-z)_{AB}$.

This BzK two colors diagram has been originally proposed to select star-forming objects at $z \sim 2$ (Daddi et al. 2004): using the highly complete spectroscopic sample of the K20 survey, objects leftward of the continuous line at $(z-K)_{AB} \gtrsim (B-z)_{AB}$ have been indeed spectroscopically identified as high–z star–forming systems.
A similar, reddening–independent selection criterion turned out to be very efficient to select z=1÷3 QSO (Sharp et al. 2002). It is interesting to note that in this region of the $(z-K)_{AB}$ vs. $(B-z)_{AB}$ plane there is the highest fraction of X–ray detected objects with respect to the overall underlying population ($\sim 30\%$). Most of the X–ray sources leftward of the straight line in Fig. 5.4 are probably high–z QSO and in particular those with R-K> 5 colors could be similar to the reddened QSOs discovered by Gregg et al. (2002), as already discussed in Sect. 3.2.2.
The combination of optical, near–infrared and hard X–ray observations, coupled with deep optical spectroscopy, will be extremely useful to accurately calibrate the BzK selection criterion for high–z star-forming galaxies: as they are only $\approx 5\%$ of the population in a K-limited sample at $K < 20$, it would be very useful to have an alternative method to distinguish them from QSO and lower redshift field galaxies. This will be crucial in order to understand their properties and the role played in the formation history of galaxies and to confirm their nature of possible star forming progenitors of local spheroids (Daddi et al. 2004).

Table 5.1. X-ray properties of the selected sources

ID	RA	DEC	FLUX(cgs)	HARD	SOFT
65	222.40227	9.14214	1.92E-13	823.4 ±38.1	2685.5±65.2
246	222.52936	8.99010	1.12E-13	365.0±27.4	1401.9±48.4
240	222.43657	8.99043	1.08E-13	524.5±31.4	1873.8±55.1
226	222.35190	8.99408	5.31E-14	424.2±28.6	1273.2±46.4
338	222.44665	8.90643	5.26E-14	175.3±20.7	643.5±34.3
258	222.16933	8.97851	5.02E-14	119.7±19.4	514.9±31.4
287	222.29214	8.94793	3.57E-14	45.4±14.4	917.7±40.0
67	222.40224	9.13641	4.43E-14	69.7±14.5	271.7±23.1
148	222.40698	9.05575	4.31E-14	332.3±26.0	848.8± 38.3
247	222.49419	8.98667	4.25E-14	214.5±22.5	585.7±32.7
300	222.29097	8.87070	4.62E-14	361.0±27.2	508.1±30.9
254	222.45354	8.98117	3.13E-14	127.7±18.5	454.5±29.3
177	222.49011	9.03878	3.16E-14	95.3±16.9	393.5±27.4
296	222.36645	8.94444	3.17E-14	328.0±25.7	595.8±33.0
370	222.46312	8.87898	2.78E-14	110.3±18.7	343.7±26.4
130	222.53819	9.07928	2.41E-14	19.6±15.3	270.6±25.0
138	222.26886	9.06119	2.62E-14	157.3±19.7	426.3±28.9
269	222.24805	8.96716	2.26E-14	128.3±19.2	398.3±28.0
350	222.28506	8.89601	1.88E-14	97.3±17.4	296.4±25.1
315	222.23386	8.92656	1.53E-14	29.1±14.5	277.1±24.3
72	222.24774	9.12793	2.84E-14	205.8±22.3	243.7±23.5
321	222.42361	8.92257	3.20E-14	398.7±27.9	349.2±26.7
255	222.35733	8.97293	1.74E-14	105.8±17.6	438.1±29.6
66	222.41078	9.13401	1.76E-14	81.4±16.7	262.5±24.1
209	222.39650	9.00872	1.87E-14	121.3±18.1	408.4±27.8
263	222.36038	8.97151	1.58E-14	65.1±15.8	417.1±29.1
170	222.27690	9.04376	1.84E-14	144.9±19.4	314.7±25.6
369	222.41988	8.87782	2.04E-14	115.2±18.4	218.8±22.3
178	222.27775	9.03575	1.43E-14	60.9±16.0	257.4±23.4
337	222.35953	8.90313	1.80E-14	102.2±17.3	223.4±22.8
195	222.23732	9.02275	2.15E-14	228.2±22.9	225.8±23.1
310	222.38553	8.87228	1.40E-14	68.0±16.4	207.2±22.0
367	222.39232	8.88237	1.53E-14	91.5±17.6	213.2±22.5
169	222.35069	8.83613	1.44E-14	74.8±16.7	143.8±19.5
207	222.48479	9.01196	1.14E-14	22.6±13.2	173.3±20.4
186	222.39986	9.03090	1.33E-14	89.4±16.8	280.5±25.5
219	222.49646	8.99483	1.41E-14	80.7±16.9	181.8±20.9
176	222.42148	9.03696	9.38E-15	48.4±13.4	186.4±21.0
179	222.17671	9.03417	1.18E-14	31.2±14.3	118.9±18.2
249	222.29024	8.97873	8.95E-15	75.3±16.0	210.7±22.3
326	222.31338	8.87259	1.28E-14	90.7±17.7	153.3±20.5
242	222.35529	8.98783	8.63E-15	43.3±14.1	242.5±24.0
344	222.23021	8.90152	9.65E-15	41.6±15.5	120.8±19.1
168	222.26276	9.04336	9.10E-15	61.4±15.1	136.8±18.7
236	222.32805	8.85342	7.72E-15	30.5±14.6	116.4±18.3
118	222.18854	9.08309	8.25E-15	0±10.0	55.2±14.5
68	222.31255	9.12831	6.58E-15	8.2±13.1	123.7±18.8
288	222.33360	8.94492	8.44E-15	95.1±17.3	171.2±20.8
103	222.27246	9.09741	7.92E-15	33.4±14.2	112.3±18.1
330	222.45485	8.91179	1.06E-14	58.1±15.7	111.0±18.2

Table 5.1 (cont'd)

ID	RA	DEC	FLUX(cgs)	HARD	SOFT
94	222.43193	9.10102	1.02E-14	28.3±13.3	106.2±17.6
363	222.46684	8.88736	9.50E-15	38.1±15.2	98.7±17.9
239	222.30952	8.85337	1.01E-14	63.3±16.7	93.0±17.8
157	222.23596	9.04881	6.57E-15	0±12.8	93.6±18.0
289	222.44273	8.85969	5.62E-15	10.0±13.3	83.0±16.9
273	222.18616	8.96340	6.96E-15	27.2±14.4	79.0±17.2
357	222.42848	8.88944	9.49E-15	56.0±15.1	86.2±17.1
301	222.32655	8.93808	3.55E-15	13.6±13.2	127.4±18.3
125	222.37209	9.07913	5.58E-15	30.9±13.7	123.3±19.2
259	222.34486	8.97245	5.78E-15	43.6±14.4	141.7±20.4
181	222.45496	9.03205	8.84E-15	90.8±17.1	108.0±18.3
244	222.26277	8.98473	6.40E-15	63.8±16.1	94.5±17.6
198	222.49593	9.01764	5.79E-15	14.4±12.9	59.0±15.4
77	222.34204	9.11713	4.84E-15	12.5±13.5	92.5±17.6
139	222.39694	9.06015	5.25E-15	28.7±13.8	114.3±18.8
107	222.23556	9.09160	7.76E-15	44.6±15.4	77.3±16.9
28	222.27797	9.16305	5.83E-15	31.2±14.4	65.5±16.5
298	222.30986	8.94036	4.45E-15	41.3±14.9	106.5±18.2
362	222.43152	8.88969	9.07E-15	69.1±15.9	73.9±16.7
319	222.28989	8.92027	3.30E-15	31.9±13.9	71.5±16.1
180	222.31963	9.03277	6.47E-15	36.4±14.0	92.5±17.5
23	222.37944	9.17607	7.16E-15	54.5±16.4	53.9±16.1
203	222.31366	9.01312	3.01E-15	30.7±13.9	103.6±17.3
73	222.26288	9.12213	3.84E-15	1.2±12.8	60.9±15.6
122	222.48840	9.08229	6.62E-15	47.3±15.1	58.4±15.8
158	222.25034	9.04792	2.89E-15	9.7±12.4	56.6±15.2
61	222.33238	9.13775	3.65E-15	21.7±14.1	57.5±15.7
282	222.22633	8.94736	3.63E-15	36.5±14.2	49.5±15.2
303	222.36128	8.93674	3.76E-15	23.3±13.1	79.3±17.7
348	222.21452	8.89961	2.73E-14	350.6±27.0	41.7±15.9
129	222.40427	9.07376	3.66E-15	29.6±14.2	70.3±16.3
146	222.41505	9.05666	5.13E-15	67.2±14.9	65.8±16.1
175	222.32443	9.03742	6.05E-15	98.6±17.5	77.9±16.6
241	222.21692	8.98637	4.77E-15	35.1±15.3	50.5±15.6
237	222.33345	8.98678	1.59E-15	10.4±12.7	65.0±16.3
217	222.45145	8.99983	8.49E-15	156.2±19.6	51.1±15.2
251	222.29764	8.97502	1.61E-15	53.8±14.7	43.8±15.0
154	222.39186	9.05019	3.34E-15	64.7±15.9	39.3±14.6
328	222.49480	8.91316	6.21E-15	57.7±16.3	23.3±14.3
361	222.40076	8.89156	6.76E-15	96.0±17.3	26.2±14.0
189	222.26324	9.02621	3.00E-15	56.8±15.3	29.1±13.9
150	222.29370	9.05019	5.36E-15	110.7±18.3	30.3±14.6
152	222.36378	9.05004	3.86E-15	93.9±17.1	28.7±14.7
250	222.43535	8.97954	4.83E-15	65.0±15.9	20.2±15.0
360	222.33772	8.88899	3.36E-15	73.6±16.5	7.7±13.2
293	222.35341	8.94158	5.38E-15	109.7±17.7	0±16.1
210	222.39818	9.01260	6.67E-15	75.8±16.7	70.2±16.1

Table 5.2. Optical photometry of the selected sources

ID	RA(X)	DEC(X)	Δ(X-O)	z_{AB}	K_{AB}	LR(z)	LR(K)
65	222.40211	9.14214	1.71	19.27	19.80	8.64	9.44
246	222.52922	8.99011	2.01	19.27	19.01	7.30	8.87
240	222.43643	8.99043	1.29	17.96	17.34	11.09	10.32
226	222.35178	8.99408	0.13	21.16	20.25	9.75	11.61
338	222.44649	8.90643	1.51	21.05	20.72	6.94	7.62
258	222.16919	8.97851	0.31	19.93	19.41	16.45	16.03
287*	222.29201	8.94793	2.22	15.46	13.72	50.25	111.02
148	222.40683	9.05575	0.64	24.02	20.58	0.26	10.09
247	222.49403	8.98667	0.98	19.94	19.21	14.45	14.08
300	222.29083	8.87071	0.68	19.10	18.58	12.50	14.54
254	222.45340	8.98117	1.20	20.49	19.49	12.61	13.10
177	222.48997	9.03878	2.26	20.54	19.54	7.00	6.80
296	222.36630	8.94443	0.23	20.31	19.20	15.53	16.13
370	222.46300	8.87898	1.10	21.10	20.73	8.15	8.95
269	222.24790	8.96716	–	–	–	–	–
350	222.28493	8.89601	1.61	19.78	19.40	11.31	11.02
315	222.23370	8.92656	1.68	20.49	20.83	10.25	7.03
72	222.24760	9.12793	2.73	21.04	19.29	3.19	5.31
321	222.42348	8.92257	0.61	20.23	19.23	14.80	15.38
255	222.35733	8.97293	–	–	–	–	–
66	222.41063	9.13401	3.82	21.46	20.96	1.09	1.20
209	222.39636	9.00872	0.53	21.59	19.91	7.06	14.04
263	222.36024	8.97151	2.47	14.49	13.62	105.64	93.10
170	222.27676	9.04376	1.18	20.64	19.38	12.23	13.19
369	222.41972	8.87782	0.28	22.23	20.64	2.63	10.61
178	222.27762	9.03575	1.11	19.98	20.05	13.87	9.67
337	222.35939	8.90313	1.21	21.75	20.24	5.91	9.34
195	222.23720	9.02275	1.49	21.89	19.72	5.27	10.50
310	222.38541	8.87228	1.54	21.13	20.75	6.85	7.52
367	222.39220	8.88237	1.02	21.91	20.87	6.30	9.18
169	222.35056	8.83613	1.26	23.67	23.10	0.61	0.00
207	222.48463	9.01196	0.99	21.30	20.42	8.44	10.04
186	222.39970	9.03090	0.39	22.28	20.56	2.60	10.49
219	222.49631	8.99483	2.05	20.44	20.43	8.33	6.19
176	222.42136	9.03696	2.27	20.54	20.12	6.95	5.37
179	222.17659	9.03417	1.21	25.14	23.10	0.00	0.00
249	222.29008	8.97873	0.80	21.41	23.10	8.88	0.00
326	222.31325	8.87259	0.42	22.74	23.10	1.83	0.00
242	222.35515	8.98782	1.46	20.87	19.75	10.95	10.64
236	222.32793	8.85342	1.08	22.04	23.10	2.24	0.00
118	222.18840	9.08309	1.37	21.07	20.07	7.37	8.78
68	222.31241	9.12831	1.66	21.35	20.90	6.46	7.10
288	222.33347	8.94492	–	–	–	–	–
103	222.27232	9.09741	3.51	19.91	18.98	2.62	2.45
330	222.45471	8.91179	0.59	23.08	23.10	0.97	0.00
94	222.43179	9.10102	2.24	20.80	19.67	7.10	6.90
239	222.30939	8.85337	0.77	21.18	19.84	8.94	13.40
289	222.44258	8.85969	3.16	21.20	20.22	2.18	2.60
273	222.18602	8.96341	1.89	22.25	19.92	1.56	8.57
301	222.32642	8.93809	0.96	20.27	19.44	13.63	14.16

Table 5.2 (cont'd)

ID	RA(X)	DEC(X)	Δ(X-O)	z_{AB}	K_{AB}	LR(z)	LR(K)
125	222.37195	9.07913	1.85	14.65	14.42	142.06	81.20
259	222.34471	8.97245	0.37	21.73	23.10	7.21	0.00
181	222.45480	9.03205	1.10	18.82	17.61	6.42	7.97
244	222.26263	8.98473	0.75	25.73	23.10	0.00	0.00
198	222.49577	9.01765	4.07	21.65	20.35	0.61	0.97
77	222.34190	9.11713	1.07	24.12	23.10	0.24	0.00
139	222.39680	9.06015	0.44	21.69	20.47	7.15	11.30
362	222.43140	8.88969	1.30	24.96	23.10	0.00	0.00
319	222.28973	8.92027	3.28	19.83	18.84	3.32	3.10
180	222.31947	9.03277	1.33	22.19	23.10	2.04	0.00
203	222.31352	9.01312	2.81	20.14	20.33	4.78	3.56
73	222.26274	9.12213	0.55	22.40	23.10	2.55	0.00
122	222.48825	9.08229	1.02	22.20	20.86	2.28	9.18
158	222.25020	9.04792	2.54	18.81	17.42	2.92	5.03
282	222.22620	8.94736	3.40	21.95	20.29	1.30	2.05
303	222.36115	8.93674	2.72	21.12	19.76	3.22	4.82
348	222.21437	8.89961	0.56	20.01	18.79	14.93	14.87
129	222.40411	9.07376	2.12	23.89	23.10	0.39	0.00
146	222.41490	9.05666	2.27	23.79	20.97	0.35	4.95
175	222.32430	9.03741	1.31	23.45	23.10	0.79	0.00
241	222.21679	8.98637	–	–	–	–	–
217	222.45131	8.99983	1.04	23.51	23.10	0.65	0.00
251	222.29749	8.97502	2.69	19.56	18.56	5.63	5.26
154	222.39186	9.05019	–	–	–	–	–
328	222.49464	8.91316	2.65	19.54	19.22	5.82	5.67
361	222.40060	8.89156	1.42	20.84	19.76	11.14	10.82
189	222.26311	9.02621	2.06	23.76	23.10	0.41	0.00
150	222.29356	9.05019	0.50	23.10	23.10	0.98	0.00
152	222.36362	9.05004	–	–	–	–	–
250	222.43523	8.97954	1.35	21.99	20.27	5.60	8.85
360	222.33759	8.88899	0.91	17.97	17.19	12.57	11.70
293	222.35329	8.94158	2.67	22.55	21.00	0.64	3.68
210	222.39806	9.01260	0.43	23.36	23.10	0.99	0.00
67	222.40208	9.13641	1.60	22.41	23.10	1.81	0.00
			3.89	20.89	20.75	1.55	1.11
138	222.26871	9.06119	1.37	21.31	20.47	7.37	8.78
			2.03	20.58	20.10	8.12	6.27
168	222.26260	9.04336	1.94	22.18	20.64	1.51	6.10
			1.73	21.01	23.10	6.24	0.00
157	222.23582	9.04881	3.92	21.88	23.10	0.73	0.00
			4.92	19.20	18.33	0.35	0.18
237	222.33331	8.98678	1.72	23.53	20.97	0.49	6.88
			3.12	21.50	20.80	2.27	2.49
363	222.46669	8.88736	2.81	24.25	23.10	0.09	0.00
			3.26	24.56	23.10	0.00	0.00
357	222.42833	8.88944	4.62	23.51	23.10	0.03	0.00
			3.63	25.64	23.10	0.00	0.00
107	222.23543	9.09159	2.29	24.73	23.10	0.00	0.00
			5.00	24.73	23.10	0.00	0.00
28	222.27785	9.16305	3.83	24.36	23.10	0.03	0.00

Table 5.2 (cont'd)

ID	RA(X)	DEC(X)	Δ(X-O)	z_{AB}	K_{AB}	LR(z)	LR(K)
			4.01	24.48	23.10	0.03	0.00
23	222.37932	9.17607	3.95	23.52	23.10	0.07	0.00
			3.47	23.38	23.10	0.17	0.00
61	222.33224	9.13775	4.19	23.79	23.10	0.06	0.00
			4.71	22.17	23.10	0.10	0.00
298	222.30972	8.94036	4.54	21.87	21.01	0.33	0.46
			3.60	23.88	23.10	0.11	0.00
			3.52	24.50	23.10	0.04	0.00
344	222.23007	8.90152	5.21	19.79	19.29	0.28	0.28
			3.72	23.69	23.10	0.10	0.00
			5.46	21.23	19.58	0.11	0.17

Table 5.3. Hard X–ray detected EROs

ID	RA(X)	DEC(X)	Δ(X-O)	R(2″)	K(2″)	R-K	HR
5σ ERO sample							
148	222.40683	9.05575	0.64	25.63	20.61	5.02	-0.44
209	222.39636	9.00872	0.53	23.52	19.96	3.56	-0.54
195	222.23720	9.02275	1.49	24.34	20.16	4.18	0.00
239	222.30939	8.85337	0.77	24.23	20.23	4.00	-0.19
146	222.41490	9.05666	2.27	25.55	21.09	4.46	0.01
189	222.26311	9.02621	2.06	24.61	20.90	3.71	> 0.32
250	222.43523	8.97954	1.35	23.75	20.31	3.44	> 0.42
293	222.35329	8.94158	2.67	24.45	20.99	3.46	1
3σ ERO sample							
362	222.43140	8.88969	1.30	26.07	21.60	4.47	-0.33
23	222.37932	9.17607	3.95	24.91	21.00	3.91	0.00

Table 5.4. Additional soft X–ray detected EROs

ID	RA(X)	DEC(X)	Δ(X-O)	R(2″)	K(2″)	R-K	HR
5σ ERO sample							
94	222.43179	9.10102	2.24	23.56	20.10	3.46	< -0.58
273	222.18602	8.96341	1.89	24.81	20.68	4.13	< -0.49
3σ ERO sample							
129	222.40411	9.07376	2.12	25.69	21.36	4.33	< -0.41

5.4 X–ray Properties of AGN EROs

Obscured accretion at high redshifts could provide additional evidence for the observed X–ray to optical properties.
As already described in Sect. 3.3, the observed high values of the X/O are, at least qualitatively, consistent with those expected by a population of high redshift, absorbed AGN with X–ray luminosities in the range $\log L_X = 42-45$ erg s^{-1} and column densities in the range N$_H$=10^{22}-10^{24} cm^{-2}

The average X–ray properties of the 10 hard X–ray detected EROs in the "Daddi Field" strongly support the hypothesis of heavily obscuration in the X–ray spectrum. Indeed, the average Hardness Ratio (HR) HR=0.06$\pm$0.45 is inconsistent, despite the large standard deviation, with that measured for the whole X–ray sample (HR=-0.34$\pm$0.41) and that expected for unobscured AGN (HR$\sim$-0.45), and supports the hypotheses of significant X–ray absorption in these objects. However, to derive the intrinsic absorption column density, the redshift of the source is needed and a more detailed analysis is deferred to a future publication, when redshifts from the scheduled VIMOS observations will be available. It is worth noticing, however, that the average HR implies N$_H > 10^{22}$ at z> 1.

In order to check whether X-ray absorption is common among these objects, I have quantitatively estimated the intrinsic X–ray column densities for the 52 EROs with a reliable spectroscopic or photometric identification available in the comparison sample described in Sect. 5.3.
Column densities for the sources detected in the CDFN and CDFS have been obtained by fitting the observed counts with a single power law model plus absorption in the source rest–frame. An example of spectral fitting of a high S/N ERO detected in the CDFN is given in Fig. 3.9. When the quality of the X-ray spectra in terms of S/N ratio was not such to use the standard χ^2 statistic, the C-Statistic was used instead. In this case the power–law spectral index has been fixed at Γ=1.9. For the sources from the Lockman Hole and the "Literature" sample, the best–fit value quoted by the authors have been adopted (see refs. above).
In all the cases, X–ray luminosities were estimated from the observed X–ray fluxes and corrected for absorption.
The results are reported in Fig. 5.5. Almost all of the individually detected EROs are consistent with intrinsic column densities in excess of 10^{22} cm^{-2}, and they actually *are* heavily obscured AGN.
This study statistically confirms previous evidences mainly based on a HR analysis (Alexander et al. 2002) and on few isolated examples (see Gandhi et al. 2003, Crawford et al. 2001, Willott et al. 2003, Stevens et al. 2003), and unambiguously indicates that large columns of cold gas (even $> 10^{23}$ cm^{-2}) are the rule rather than the exception in EROs individually detected in the X–rays.

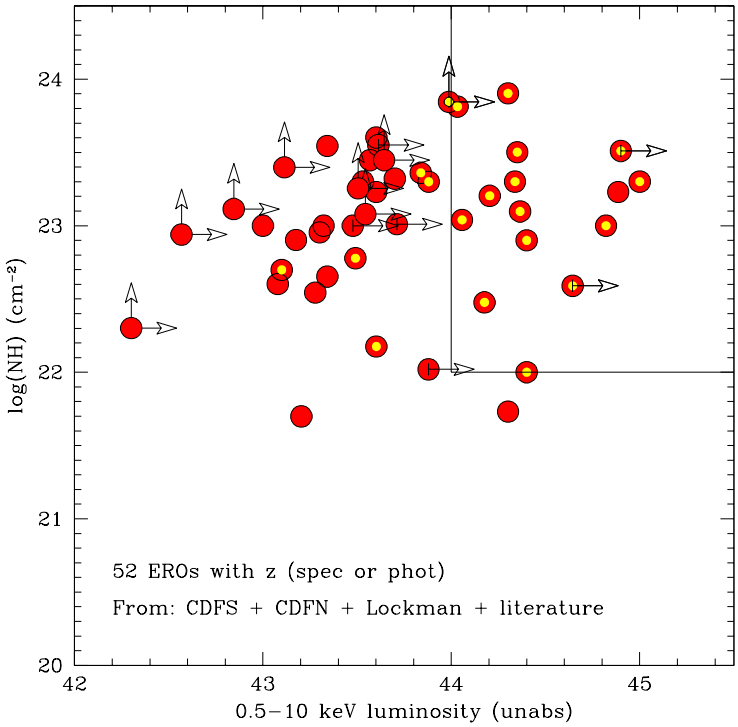

Figure 5.5 Logarithm of the unabsorbed X–ray luminosity in the 0.5-10 keV band versus the logarithm of the absorbing column density (N_H) for all the X–ray detected EROs with spectroscopic or photometric redshifts from the comparison sample. Yellow–dot symbols are those with X/O > 10 (see text). The boxy region indicates the locus of QSO2.

5.5 EROs and QSO2: a selection criterion

Given the high–redshift of these objects (z$\gtrsim 1$) and the average X–ray flux of the comparison sample ($\sim 4 \times 10^{-15}$ erg cm^{-2} s^{-1}), it is not surprising that the majority of X–ray detected EROs have high X–ray luminosities ($L_X > 10^{43}$ erg s^{-1}, see Fig. 5.5). Moreover, according to our analysis, a fraction larger than 30% have X–ray luminosities even larger than $L_X > 10^{44}$ erg s^{-1}, and therefore well within the Quasar regime. The large intrinsic column densities further imply that AGN EROs, selected at the brightest X–ray fluxes, have properties similar to those of Quasars 2, the high–luminosity, high redshift type II AGNs predicted in X–Ray Background synthesis models (e.g. Comastri et al. 2001; Gilli et al. 2001). Similar results have been obtained also by Severgnini et al. (2004) based on XMM–*Newton* observations of a sample of K–selected objects in the framework of the TESIS project.

Among the X–ray detected EROs, the higher is the luminosity, the higher is the X–ray to optical flux ratio: in Fig. 5.5 the sources with X/O greater

than 10 are reported as dot-dot symbols and populate the upper right region of the diagram. This confirms that a selection on the basis of X/O ratio > 10 is a powerful tool to detect high–luminosity, highly obscured sources (see Sect. 3.2 and 3.3), and it is even stronger when coupled with a previous selection on the basis of extremely red colors.

Given that the search for high–luminosities highly obscured quasars on the basis of detection of narrow optical emission lines is very difficult and is already challenging the capabilities of ground based, 10m class optical telescopes, the "alternative" method based on the combination of near–infrared and X–ray observations, could provide a powerful tool to uncover this population of luminous, obscured quasars, that are the key ingredient of XRB synthesis models.
It is important to stress that this selection criterion works only in one direction: EROs with high X/O can be QSO2 but it is not true that all the QSO2 are EROs. As an example, the test–case of high redshift QSO2, CDFS_202 in Norman et al. (2002), has a R-K$\sim$2.5. In this case the observed colour does not reflect the galactic continuum, but rather the chance superposition of emission lines into the broadband filters. When the flux contribution of the lines is subtracted, the R-Ks colour of CDFS_202 is R-K$\sim$4, which is, nevertheless, appreciably red.

Chapter 6

Extremely Red Objects: an X–ray dichotomy

Sensitive hard X–ray observations provide a powerful method to overcome the effect of gas absorption in highly obscured AGN and to uncover hidden AGN activity among the EROs population. It has also been shown, however, that the majority of the ERO population is not related to active phenomena, and, therefore, they will not be individually detected even in the deepest X–ray exposures.
The excellent imaging capabilities of *Chandra* (i.e. the subarcsec positional accuracy and the negligible background) constitute a unique tool to probe the average X–ray properties of sources or classes of objects, even beyond the effective limiting flux of the X–ray observations. The "stacking analysis" technique turned out to be particularly efficient when applied to sources detected in the CDFN and CDFS fields, reaching equivalent total exposures from 10 to 100 times the nominal ones and pushing the X–ray detection more than two order of magnitude deeper (see Brandt et al. 2001b; Hornschemeier et al. 2002; Nandra et al. 2002).

An interesting study of the average X–ray properties of those EROs not individually detected in the CDFN was reported by Alexander et al. (2002): stacking analysis of those objects not individually detected in the X–rays suggested a softer X–ray spectrum than that of AGN–powered EROs and an X–ray to optical flux ratio consistent with that expected from normal elliptical galaxies, star–forming systems or low luminosity ($L_{2-10keV} < 10^{42}$ erg s^{-1}) nuclear activity at $z \simeq 1$. This study, however, despite the faint X–ray and optical flux limits reached, was mainly limited by the lack of spectroscopic data.

High–quality optical spectroscopy for a sample of 21 EROs in the CDFS has been obtained in the framework of the $K20$ survey (Cimatti et al. 2002a); optical classifications have been obtained for all the 21 EROs in the sample:

the spectroscopic data have shown that EROs are nearly equally populated by old, passively evolving systems and dusty star–forming galaxies over a similar range of redshift ($z_{mean} \sim 1$ for both the classes).
In order to investigate whether the X–ray emission properties of EROs are depending on the optical/infrared spectral properties, I have retrieved the public CDFS one Megaseconds *Chandra* observation available in the archive (Giacconi et al. 2002) and I have applied the stacking technique separately for the two classes of EROs.

6.1 The K20 ERO sample

The ESO VLT K20 sample is one of the largest and most complete spectroscopic sample of galaxies with $K_s < 20$ available to date; the main scientific goal of this project is the comparison of the observed redshift distribution of a complete sample of about 500 galaxies (87% complete to $K_s < 20$, 98% if photometric redshifts are included) with the predictions of galaxy formation models in order to obtain stringent clues on the formation and evolution of the present-day massive galaxies (Cimatti et al. 2002b). The K20 sample cover a sub-area (32.2 arcmin^2) of the *Chandra* Deep Field South (CDFS) and a 19.8 arcmin^2 field around the quasar 0055-2659.
Extremely Red Objects in the K20 sample were selected with the criterion of $R - K_s > 5$, and then classified on the basis of their optical spectra into two categories (Cimatti et al. 2002a): objects with an absorption line spectrum, consistent with that of early–type, passively evolving galaxies (hereinafter "old") and objects showing [OII]$\lambda 3727$ emission line with an observed Equivalent Width EW$>$ 20 Å over a red continuum, consistent with that of dusty star–forming systems (hereinafter "dusty"). The K20 EROs sample in the CDFS area includes 48 objects at $K_s < 20$. In the following I will consider only the 21 spectroscopically identified EROs, which have been classified in the two categories described above: 13 "dusty" and 8 "old", distributed on a similar range of redshifts, $z = 0.8 \div 1.6$.

6.2 X–ray data analysis

The *Chandra* Deep Field South (CDFS) survey is a combination of 11 individual *Chandra* ACIS–I pointings observed in two years, from March 1999 to December 2000 (Giacconi et al. 2002). The maximum effective exposure time is 942 ks, but it varies across the detector due to the CCD gaps and the rotation of the field–of–view in the different observations. In order to estimate the effective exposure time for each object, all the events corresponding to the single pointings along with the combined photon event list, have been downloaded from the archive. I calculated the exposure and instrument maps using standard CIAO 2.2.1 tools for each observation separately, and combined them to evaluate point–by–point the effective exposures. As the mirror vignetting is energy dependent, I calculated the exposure maps at two energies (1 keV and 4 keV), representative of the

mean energy of the photons in the soft (0.5–2 keV) and hard (2–8 keV) bands.
At first, I have searched for individual X–ray emission from all the EROs in the spectroscopic redshift catalog of Cimatti et al. (2002a). This was accomplished by searching for nearby (within $2''$) X-ray sources found by WAVDETECT in the K20 region, with a false-positive probability threshold of 10^{-5} (Freeman et al. 2002). Only one source, a dusty ERO at $z = 1.327$, was individually detected; the optical position is almost coincident ($\Delta < 0.3$", within the accuracy of the K–band position) with the *Chandra* source CXO CDFS J033213.9-274526 in the Giacconi et al. (2002) catalog.

6.2.1 CXO CDFS J033213.9-274526: a type 2 AGN

The only ERO individually detected in the 1 Ms exposure is the highest redshift, highest luminous (R=23.81, K_s=18.44) object in the "dusty" sample. It is a very hard X–ray source ($F_{2-8keV}=7.34 \times 10^{-16}$ erg cm^{-2} s^{-1}, $\Gamma = 1.4$ and N_H=Gal; Giacconi et al. 2002) undetected in the soft band ($F_{0.5-2keV} < 5.48 \times 10^{-17}$ erg cm^{-2}) The observed band ratio (H/S> 7.3) implies an intrinsic X–ray column density larger than 4×10^{23} cm^{-2}, for a typical AGN power–law spectrum with $\Gamma = 1.8$. The observed 2–8 keV luminosity is $\sim 7 \times 10^{42}$ erg s^{-1} which corresponds to an unabsorbed, rest–frame hard X-ray luminosity $\sim 4 \times 10^{43}$ erg s^{-1}, typical of Seyfert galaxies. At the high–energy, therefore, CXO CDFS J033213.9-274526 is naturally classified as a Type 2, active object. In the optical domain it shows only a faint, but significant, [OII]$\lambda 3727$ emission feature. Unfortunately, at the expected [NeV]$\lambda 3426$ position a strong cosmic ray has affected the data. The lack of (broad) MgII$\lambda 2798$ emission indicates that obscured activity is taking place also in the optical nucleus.

The low number of individually X–ray detected EROs ($1/21$) is in agreement with the results presented in the previous Chapter: the bulk of the EROs population is not related to active phenomena.
Moreover, this is an additional example of source whose AGN nature has been recovered only by means of X–ray observations.

6.3 X–ray stacking analysis

The use of stacking to determine mean properties of objects has been applied widely in X-ray astronomy (e.g., Green et al. 1995; Della Ceca et al. 1999). By adding together X-ray photons from well-defined classes of object, it is possible to determine their mean X-ray properties; by removing known, bright X-ray sources from the sample it is also possible to investigate the mean properties of sources too weak to be individually detected (Brandt et al. 2001b; Nandra et al. 2002).

In order to constrain average X–ray properties of the remaining individually

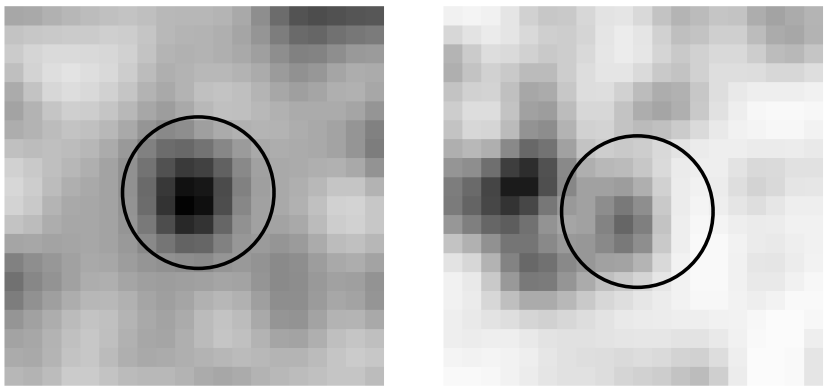

Figure 6.1 Stacked full–band images of the "dusty" (*left panel*) and "old" (*right panel*) EROs. The images are 9x9 arcsec and have been smoothed with a Gaussian of σ=1.5 pixel (approx 0.7″) . The circles are centered on the stacking position and have a radius of 2″. The detection significance of the summed counts is 4.2σ for the "dusty" and $< 2\sigma$ for the "old". The bright spot in the right panel at about 4″ from the stacked position, corresponds to an individually detected object.

undetected EROs, I have applied the stacking technique separately for the two classes of objects. The samples consist of 12 "dusty" (once CXO CDFS J033213.9-274526 has been removed) and 8 "old" EROs, with average redshifts of $z = 1.053$ and $z = 1.145$, respectively.

For the photometry a circular aperture with a radius of 2″ centered at the positions of the selected EROs was adopted. I have also checked different aperture radii ($1 - 4$") and found that the adopted one is an optimal extraction radius for the counts estimate, in agreement with the Nandra et al. (2002) findings. The counts were stacked in the standard soft, hard and full bands (0.5–2 keV, 2–8 keV, and 0.5–8 keV), and in the 1–5 keV band which roughly corresponds to the rest–frame 2–10 keV band at the mean redshift of the objects.

To verify whether the stacked net counts constitute a significant signal the local background has been estimated: in annular regions around each ERO centroid, as the average of eight circular regions (2 arcsec radius) for each ERO position and from a background map produced by the WAVDETECT algorithm. The different choices do not significantly affect the results in none of the adopted energy bands, except the 2–8 keV range where the results are strongly affected by the increased level of the instrumental background.

The results of the stacking analysis reported in Table 1 are referred to the background estimated as the average of the eight circular regions; in Fig. 6.1 the summed images in the full (0.5–8 keV) band for both classes of objects is shown.

Extensive Monte Carlo simulations (up to 10,000 trials) have been

Stacking Results

Class	band (keV)	counts total	counts BKG	c.l.	Exp. (Ms)	Flux†	$L_X^{\dagger}$
Dusty	0.5-8	172	124.2	99.997%	10.2	3.4±1.3	20 ± 8
	0.5-2	67	37.9	99.995%	10.4	1.3±0.45	7.4 ± 2.6
	1-5	83	61.4	99.6%	10.2	1.4±0.5	8.0 ± 2.8
	2-8	105	86.3	97.2%	10.1	< 4.8	< 27
Old‡	0.5-8	102	92.1	$< 90\%$	7.0	< 7.5	< 40
	0.5-2	33	26.0	$< 90\%$	7.0	< 24	< 10

Table 6.1 Stacking results: †: Fluxes (in units of 10^{-17} erg cm^{-2} s^{-1}) and luminosity (in units of 10^{40} erg s^{-1}) are computed assuming a power–law spectrum with $\Gamma = 2.1$ and Galactic absorption for the "dusty" sample, and a thermal emission model with kT=1 keV and solar metallicity for the "old" sample. Errors are at the 90% confidence level. ‡: For the "old" sample only the results in the 0.5–8 keV and 0.5–2 keV bands are reported. In the harder bands the results are always consistent, within 1σ, with the background fluctuations.

carried out shuffling 12(8) random positions for "dusty" and "old" EROs respectively, using the same photometry aperture (2 arcsec). The random positions were chosen to lie in "local background regions" to reproduce the actual background as close as possible. The resulting distributions for the trials in the soft band are shown in Fig. 6.2, for both the old (1,000 simulations) and dusty (10,0000 simulation) samples. The distributions are well approximated by Gaussians; the corresponding detection confidence level is in all the cases in good agreement with that computed from Poisson statistic (see below).

6.4 An X–ray dichotomy

The X–ray emission from "old" EROs remains undetected in all the considered energy bands, for a total effective exposure time of ~ 7.0 Ms. Assuming a thermal emission model with kT=1 keV and solar metallicity, fully consistent with the average X–ray spectrum of nearby elliptical galaxies (e.g., Pellegrini 1999), the 3σ upper limit on the 0.5–2 keV luminosity is $L_X < 10^{41}$ erg s^{-1} (see also Vignali et al. 2002).

An excess of counts above the expected background level is clearly present in the "dusty" sample, for a total effective exposure time of 10 Ms. The signal is stronger in the full band (99.997% confidence level assuming a Poisson distribution, corresponding to about 4.2σ) and it is still present, although at a slightly lower confidence level, in the soft and 1–5 keV band, while it is not statistically significant in the hard band.
Assuming a $\Gamma = 2$ power–law spectrum plus Galactic absorption ($N_H =$

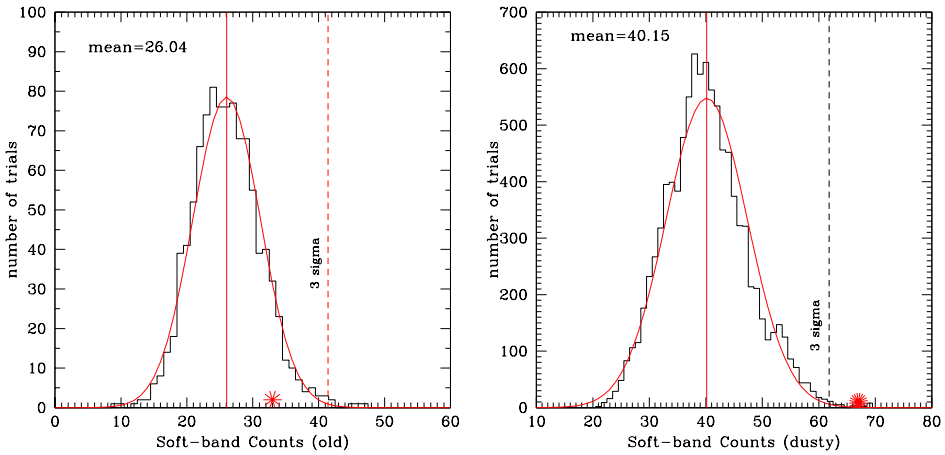

Figure 6.2 Background counts distributions for the old (left) and dusty (right) EROs in the soft (0.5–2 keV) band. The vertical continuous lines show the mean background counts in the source cells derived from the Montecarlo method (1000 and 10000 trials, respectively). The vertical dashed lines show the 3σ fluctuation limit: stacked detection with a number of counts larger than these values are considered as "real" detection at the 99.9% confidence level. The big asterisks represent the counts actually detected from the old and dusty samples, respectively.

8×10^{19} cm^{-2}), the 3σ upper limit on the average band ratio (H/S<0.85, where H and S indicates the hard band and soft band counts, respectively), corresponds to an absorption column density lower than 10^{22} cm^{-2}. With the same assumptions, the stacked count rate in the 1–5 keV band corresponds to an average 2–10 keV rest–frame luminosity of $\sim 8 \times 10^{40}$ erg s^{-1}, at the mean redshift z=1.053.

The X–ray and optical data both suggest that starburst activity, rather than AGN, is powering "dusty" EROs. This is shown in Fig. 6.3, where the observed optical and X–ray properties of the "dusty" sample are compared with that of AGN–powered EROs: the upper limits on both the X/O (*left panel*) and the N_H (*right panel*) are clearly inconsistent with the average value observed in X–ray detected EROs.

The starburst scenario is supported also by the spectroscopic data. Indeed, following Cimatti et al. (2002a), we recomputed the average spectrum of the 12 EROs we used in the X–ray stacking analysis. The average optical spectrum shows a very red and smooth continuum, with a strong [OII]$\lambda 3727$ emission and lacks of the presence of clear AGN indicators such as [NeV]$\lambda 3426$, suggesting that the optical emission is dominated by star–forming systems.

Finally, I have also investigated whether the stacked signal could be due to a few individual sources just below the detection threshold. This is particularly relevant for our sample which may contain a few sub-threshold

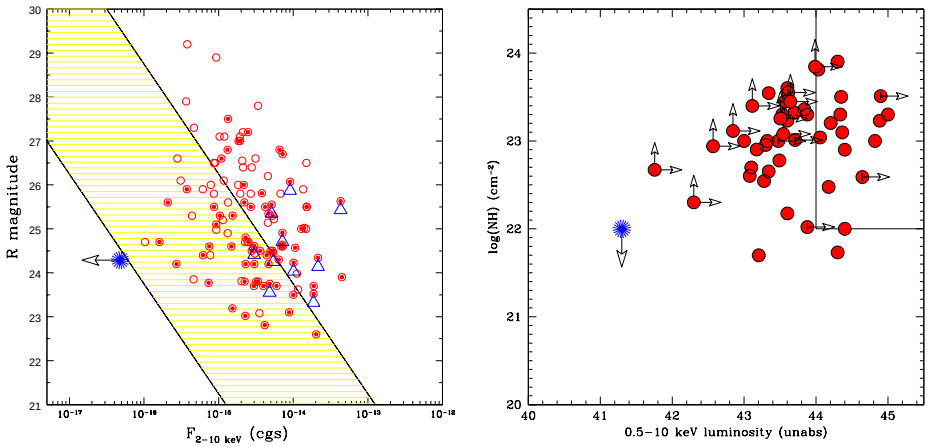

Figure 6.3 (*left panel*) R–band magnitude vs. hard X–ray flux diagram. Symbols as in Fig. 5.3. The result of stacking analysis of the "dusty" sample is also reported (asterisk). (*right panel*) Unabsorbed X–ray luminosity in the 0.5-10 keV band versus the logarithm of the absorbing column density (N_H). Symbols as in Fig. 5.5. The result from the stacking analysis of the "dusty" sample is marked with an asterisk.

AGN responsible for the entire stacked signal. Five out of 12 "dusty" EROs are individually "detected" at the 95–99% confidence level. The X–ray luminosity for these "marginally detected" EROs never exceeds 6×10^{41} erg s^{-1} in the full–band excluding the presence of a bright AGN among the stacked dusty EROs. Although the presence of a low–luminosity AGN (LLAGN) can not be completely ruled out on the basis of the present analysis, in the following it has been assumed that the "dusty" EROs are mainly powered by starburst related processes.

6.4.1 Star Formation Rate: the hard X–rays view

The inferred, average X–ray luminosity of the "dusty" sample is around one order of magnitude larger than that of normal spiral galaxies (Matsumoto et al. 1997) and it is similar to that of the starburst galaxy M82 (e.g., Griffiths et al. 2000; Kaaret et al. 2001); the average X–ray spectrum (see Sect. 3) is consistent with that measured for nearby star–forming galaxies (e.g. Dahlem, Weaver & Heckman 1998; Ptak et al. 1999).
The hard X–ray luminosity of star–forming objects can be used as a star formation rate (SFR) indicator (Ranalli, Comastri, & Setti 2003; Nandra et al. 2002; Bauer et al. 2002).
Using the Ranalli et al. (2003) relation:

$$SFR(X) M_{\odot}/yr = 2.0 \times 10^{-40} L_{2-10keV} erg/s \qquad (6.1)$$

it is possible to derive an average SFR for the EROs in the "dusty" sample of 5–44 $M_{\odot} yr^{-1}$, taking into account the observed dispersion between the

far–infrared and X–ray luminosities quoted by Ranalli et al. (2003), and the uncertainties on the hard X–ray luminosity. The average SFR derived from the the observed [OII] luminosity (Kennicutt 1998) is SFR([OII])$_{obs}$=2.7 M$_\odot$yr^{-1}. The discrepancy between the optical and X–ray SFR estimates confirms that the optical emission lines are severely obscured by dust and the optical value can be addressed as a *lower limit*. In order to provide a dereddened SFR estimate, the average spectrum was compared with template spectra of star forming galaxies and dusty systems (as extensively discussed in Cimatti et al. 2002a); the best–fit estimates for the reddening are in the range $E(B-V) = 0.5 \div 0.8$, which implies an intrinsic average SFR of the order 37–110 M$_\odot$yr^{-1} according to the Kennicutt (1998) relation. Although the two estimates suffer of large uncertainties, mainly related to the scatter of the various SFR indicators, they can be reconciled if the lowest extinction correction (e.g., $E(B-V) \sim 0.5$, or even lower) is applied to correct the [OII] luminosity.

From the derived X–ray SFR it is possible to estimate the average far–infrared (60–100 μm) and radio (1.4 GHz) emission of the objects in our sample: L$_{FIR}$ = $10^{10.4} \div 10^{11.4}$ L$_\odot$; L$_{1.4GHz}$ = $2 \div 17.6 \times 10^{29}$ erg s^{-1} Hz^{-1} (Kennicutt 1998). The relatively low value of L$_{FIR}$ would naturally explain the low detection rate of EROs in submillimeter continuum follow–up observations, typically sensitive to detect Ultra–Luminous Infrared Galaxies (ULIGs, L$> 10^{12}$ L$_\odot$) at $z \gtrsim 1$ (e.g., Mohan et al. 2002). The "dusty" ERO population would then be representative of less luminous dusty star–forming systems, with respect to submillimeter–selected high–z galaxies, as already pointed out in Cimatti et al (2002a).

The inferred radio luminosity corresponds to K–corrected ($S_\nu \propto \nu^{-\alpha}$, $\alpha = 0.7$) radio fluxes in the range 4-38μJy. The lack of deep radio observations in the *Chandra* Deep Field South area prevents to test these predictions; however, it is interesting to note that very deep 1.4 GHz VLA observations of a sample of optically selected EROs (Smail et al. 2002) agree with our estimates (about 85% of the EROs in their sample is not detected in the radio band at fluxes higher than ~ 40 μJy).

Conclusions

The most important results obtained in this PhD Thesis concern the physical and evolutionary properties of obscured AGN detected in hard X–ray surveys, that contributes most to the accretion history in the Universe.

- The HELLAS2XMM survey has provided optical identifications and spectroscopic classifications for 97 out of 122 hard X–ray selected sources detected in $\sim$1 deg^2 (the HELLAS2XMM 1dF sample). The spectroscopic completeness of the sample ($\sim$80%, mainly limited by the faintness of the optical counterparts) is one of the highest for sources detected at flux level $\gtrsim 10^{-14}$ erg cm^{-2} s^{-1} and the results from the HELLAS2XMM survey represent a complementary and necessary probe of the hard X–ray sky with respect to the deep, pencil–beam *Chandra* and XMM–*Newton* surveys.
  A detailed study of one specific field (the PKS 0312–77 field) for which *Chandra*, radio and near–infrared data were also available, has clearly demonstrated the need for high spatial resolution observations to exactly identify the hard X–ray sources counterparts (Chapter 1).

- The overall picture emerging from the optical identifications of the HELLAS2XMM 1dF sample indicate a wide spread in the optical (both in the continuum shape and emission lines) and X–ray properties of the sources responsible for the bulk of XRB energy density, confirming and extending results obtained from both deep and shallow surveys.

  – The combination of X–ray spectral analysis and deep VLT spectroscopy has revealed that $\sim$ 10% of high–redshift, high–luminosity objects optically classified as unobscured BL AGN are absorbed in the X–rays by column densities in excess than 10^{22} cm^{-2}.

  – The elusive properties of those AGN classified as X–ray Bright Optically Normal Galaxies (XBONG) can be due to a combination of the absorption associated with the AGN and the optical faintness of the nuclear emission with respect to the host galaxy. Obscuration of the nuclear source by large columns (possibly Compton thick) of cold gas seems to provide the most plausible explanation of the observed broad–band properties, though such a possibility is not unique.

The optical appearance of hard X–ray selected AGN is different from what expected on the basis of classic Unified Schemes, calling for some revisions to account for the discrepant classifications produced by the properties of the circumnuclear medium, and/or by geometrical or beaming effects (Chapter 2).

- Thanks to the large area covered, we have obtained the first spectroscopic identification of a sizable sample of objects with an extreme X–ray to optical flux ratio (X/O > 10).
  Different approaches, beside the photometric technique, to estimate the redshift of optically faint X–ray sources, have also been developed and tested to derive the redshift distribution of highly obscured, even Compton thick AGN:

  - COLOUR-BASED REDSHIFTS: coupling the morphological information derived from K–band surface brightness profiles for a subsample of X/O> 10 sources in the HELLAS2XMM survey, with the observed R-K colours, it was possible to derive a "minimum" redshift for these objects;
  - A STATISTICAL APPROACH: on the basis of the optical to X–ray properties of identified sources it was possible to statistically assign luminosities — hence the redshifts — to optically faint X–ray sources in a combined sample of hard X–ray selected objects.
  - THE DETECTION OF STRONG FeKα FEATURES: it was possible to derive the redshift of highly obscured objects by detecting a strong FeKα line in a few high S/N X–ray spectra of sources detected in the deepest *Chandra* fields.

  A detailed comparison with X-ray selected sources in various deep and medium–deep surveys indicates that heavy ($N_H > 10^{22}$ cm^{-2}) obscuration is almost ubiquitous among objects with high X/O and that obscured sources (in particular QSO2, the high-luminosity, high-redshift obscured AGNs predicted in XRB synthesis models) can be hosted in the bulge of luminous, massive ellipticals which already formed the bulk of their stars at high redshift (Chapter 3).

- Using the correlation observed between the X/O and the X–ray luminosity for obscured sources, it was possible to build a "virtually complete" sample of identified hard X–ray sources over a wide range of redshifts and luminosities. We have confirmed that a luminosity-dependent density evolution for the sources responsible for the XRB (low luminosity sources peaking at a later cosmic time) is needed to match the observed number and luminosity densities as a function of redshift. With this assumption, and the hypothesis that hard X–ray surveys probe the largest fraction of the whole AGN population, it is possible to explain the observed local BH mass density as entirely due to the growth of AGN (Chapter 4).

- The first comprehensive characterization of the X–ray properties of a large sample of X–ray detected EROs has been presented. Results obtained from a 80 ks XMM–*Newton* observation indicate that, at the relatively bright X–ray and near–infrared fluxes probed by the present observation, AGN contribute only for a negligible fraction ($\sim$3%) to the optically selected EROs population. Although a spectroscopic redshift is not available for all of the sources, the X-ray, optical, and near-infrared properties of X-ray selected EROs nicely fit those expected for QSO2, confirming the results obtained in Chapter 3 from the HELLAS2XMM survey (Chapter 5).

- The results of *Chandra* stacking analysis of a well defined sample of spectroscopically identified, non–AGN EROs suggest that the dichotomy in the spectroscopic classification of the majority of K–selected, non–AGN EROs (e.g. dusty and old systems) appears to be present also in the X–rays: "dusty" objects are relatively bright X–ray sources ($L_X \sim 10^{41}$ erg s^{-1}), while "old" EROs are below the detection threshold. Moreover, using the hard X–ray luminosity as a Star Formation Rate (SFR) indicator, it has been possible to estimate an average SFR for the dusty population in the range 5-44 $M_\odot$ yr^{-1}; this estimate is lower than, although consistent with, the value based on the reddening–dependent [OII] emission and is in agreement with results from recent far–infrared and radio observations (Chapter 6).

Undoubtedly, the somewhat unexpected link between EROs and QSO2, is intriguing: near infrared observations of obscured QSO selected on the basis of their high X/O and, conversely, hard X–ray observations of a complete sample of EROs, constitute one of the strongest evidences that these two populations originally discovered at different wavelengths are intimately connected. **A selection criterion based on the X/O and the R-K colour of hard X–ray selected sources has been proposed, to efficiently pick–up the elusive QSO2 population**, difficult to select at optical wavelengths. Furthermore, X–ray detected EROs can be used as lighthouses to investigate the accretion paradigm at high redshifts to address the issue of elliptical galaxy formation and the expected co-evolution with the accreting black-holes.

Future Directions

The description of the nature of hard X–ray selected sources has already approached a fairly complicate picture. While the general trends are rather robust (several independent arguments converge to the similar qualitative results) the number of X-ray sources with spectroscopic identifications is still far too small to derive accurate quantitative information about the AGN evolution at high redshift (z=2-4). Moreover, in order to obtain robust estimates of the black hole mass density due to growth by accretion, a much better knowledge of the redshift, luminosity and Spectral Energy

Distributions (SEDs, related to k_{bol}) of highly obscured AGN is of paramount importance.
The absorbed radiation emitted by the nucleus is expected to be re-emitted in the far–infrared and sub–mm bands. In this framework, *Spitzer* observations (from 3.6 μm to 170 μm) of a well–selected sample of sources detected in the HELLAS2XMM 1dF sample (including XBONG, high X/O, EROs and QSO2) have been proposed, to complement the multiwavelength database and to probe the physical properties of those AGN for which the presence of SMBH is inferred from the X–ray emission but which remains elusive from observations at optical–UV and near–infrared wavelengths. Moreover, SCUBA (850 μm) observations of an X–ray selected sample of X–ray Type II QSO could be crucial to derive a solid estimate of the bolometric luminosity of accretion powered hard X-ray sources and of the correlations between X–ray luminosity and obscuration with infrared emission.

The results from both deep and shallow surveys have unambiguously unveiled a differential evolution for the low– and high–luminosity AGN population. In this respect, the evolution of the obscured AGN luminosity function remains the key parameter to be determined. A study takling simultaneously the problems of the shape and evolution of the luminosity function, and of the N_H distribution as a function of luminosity and cosmic epoch (with an approach akin to that followed by Ueda et al. 2003), will be the subject of future investigations (La Franca et al., in preparation).
The best strategy to properly address this issue is to increase the area covered in the X–ray band, and the corresponding optical-NIR photometric and spectroscopic follow-up, down to $F_{2-10keV} = 1-5\times10^{-15}$ erg cm^{-2} s^{-1}, where the bulk of the XRB is made, rather than pushing the depth of the survey beyond the present limits of the deepest *Chandra* surveys.
On the one hand, the optical follow-up of the HELLAS2XMM sources will be extended from 1 to 4 deg^2, in order to obtain a sample of 100-150 obscured objects at $F_{2-10keV} > 10^{-14}$ erg cm^{-2} s^{-1}, sufficient to constrain the high–luminosity tail of their X–ray luminosity function and to adequately figure their differential evolution over 2-3 luminosity dex and up to z$\sim$2 (Cocchia, PhD Thesis).
On the other hand, the XMM–*Newton* survey of the ELAIS–S1 field (Puccetti, PhD Thesis) will push the limiting fluxes down to 2×10^{-15} erg cm^{-2} s^{-1} over ~ 0.5 deg^2 allowing to considerably increase the statistic on high redshift, moderate luminosity objects.
Finally, a comprehensive multiwavelength program is underway to observe a contiguous area of ~ 2 deg^2 (the "COSMOS" project) using all the modern (HST/ACS, *Spitzer*, XMM–*Newton*, *Chandra*, VLT/VIMOS, VLA, GALEX) and future (e.g. ALMA) observatories from radio to X–rays. These data will provide the necessary photometry to characterize the SEDs of some thousands of AGNs as a function of redshift and type, and to explore almost all the aspects of galaxy/AGN evolution. The large area covered will allow a detailed comparison between galaxy and AGN clustering, and theoretical

models for the evolution of the large scale structure of the Universe. This will shed new light on the issue of whether AGNs trace higher density peaks or higher mass haloes in the high–redshift universe and how active sources are correlated with the environment.

With the full exploitation of all the multiwavelength data, it will be possible to build up large and homogeneously–selected samples of almost all the classes of objects revealed in the deep imaging surveys (e.g: AGN, EROs, B–dropout, High–z star-forming galaxies, cluster of galaxies etc.).
In particular, the combination of optical, near–infrared and X–ray (both *Chandra* and XMM–*Newton*) data of complete samples of EROs are crucial to definitively assess the fraction of reddened sources among the XRB constituents, the link between EROs, high X/O and QSO2, and the rôle of these objects in the framework of galaxy formation.

Acknowledgements

At the end of this thesis I wish to thank all those people whom in the last three (four, eight..) years helped and supported me in many ways – and more important, they still do it.
My deep thanks go to Andrea Comastri, who interacted with me almost every day since I graduated. Thanks, Andrea, for teaching me most of the things I know, for the continuous stimulating discussions, for your constant encouragement, moral support and real friendship during *all* these years and, above all, for having shown me the right way to do research, and to enjoy it.

I warmly thank Gianni Zamorani, always ready for scientific discussions and advices, despite the so many other things to do: he has been for me a reference of professionality, hard labor and scientific passion.
I really thank Giorgio Palumbo for being for me source of most enthusiasm on the X–ray astronomy field, Renzo Sancisi for all his valuable suggestions and comments, and Bruno Marano, always ready to help me whenever I needed.

A warm thank goes to all the members of the `HELLAS2XMM` collaboration for having guided me, in these years, throughout hard X–ray surveys and multiwavelength astronomy. In particular, I would like to thank Fabrizio Fiore, who is a very good reference of all the collaboration, and supports me since the beginning; and Marco Mignoli for his enormous patience with me in these three years.

Lots of thanks go to Cristian Vignali and Lucia Pozzetti, for answering all my, sometimes boring, questions – and for being good friends, besides colleagues. Thanks to all the other (many!) astronomers that, in all these years, I had the opportunity to meet. In particular, Emanuele Daddi and Andrea Cimatti, my references in the "EROs field", the "Florence" group (Alessandro, Guido, Roberto(s)), with whom I enjoied, above all, the Mexican experience, and Francesca – a really good, new friend.

During the last three years, I had the opportunity to share lot of (almost all...) my lifetime with Francy, Marta, Lorenzo, Luca and Piero (my PhD mates here in Bologna) and several others people spread world–wide (Anna Lia and Luca, in primis). I thank all of them for being my best friends (and my "family") since 8 years.

Finally, I wish to thank all the friends that shared with me good time and fun, holidays and apartments, besides my work. The list is long ... but you know who you are ... so thanks all!
Overall, I thank my (enlarged) family, down to my old aunts, and in particular my $mamma$, to whom this thesis is dedicated: I would like her to know how much her love and support have been important for me.

Related Publications

The Hellas2XMM Survey

REFEREED JOURNALS

- Baldi A., Molendi S., Comastri A., Fiore F., Matt G., & Vignali C.
The HELLAS2XMM survey. I.
The X–ray data and the log(N)–log(S).
2002, ApJ 564, 190

- Comastri A., Mignoli M., Ciliegi P., Severgnini P., Maiolino R., **Brusa M.**, Fiore F., Baldi A., Molendi S., Morganti R., Vignali C., La Franca F., Matt G., Perola G.C.
The HELLAS2XMM survey. II.
Multiwavelength observations of P3: an X–ray bright, optically inactive galaxy
2002, ApJ 571, 771

- **Brusa M.**, Comastri A., Mignoli M., Fiore, F., Ciliegi, P., Vignali, C., Severgnini, P., Cocchia, F., La Franca, F., Matt, G., Perola, G.C., Maiolino, R., Baldi, A., Molendi, S.
The HELLAS2XMM survey. III.
Multiwavelength observations of hard X–ray selected sources in the PKS 0312–77 field
2003, A&A 409, 65

- Fiore F., **Brusa M.**, Cocchia F., Baldi F., Carangelo N., Ciliegi P., Comastri A., La Franca F., Maiolino R., Matt G., Molendi S., Mignoli M., Perola G.C., Severgnini P., Vignali C.
The HELLAS2XMM survey. IV.
Optical identifications and the evolution of the accretion luminosity in the Universe
2003, A&A 409, 79

- Mignoli M., Pozzetti L., Comastri A., **Brusa M.**, Ciliegi P., Cocchia F., Fiore F., La Franca F., Maiolino R., Matt G., Molendi S., Perola G.C., Severgnini P., & Vignali C.
The HELLAS2XMM survey. V.
Near-Infrared observations of X-ray sources with extreme X/O ratios
2004, A&A, in press, astro-ph/0401298

- Perola G.C., Puccetti S., Fiore F., Sacchi N., **Brusa M.**, Cocchia F., Baldi A., Carangelo N., Ciliegi P., Comastri A., La Franca F., Maiolino R., Matt G., Mignoli M., Molendi S., & Vignali C.
The HELLAS2XMM survey. VI.
X–ray absorption in the 1df AGN sample through a spectral analysis.
2004, A&A, submitted

- La Franca F., & the HELLAS2XMM Team
  The HELLAS2XMM survey. VII.
  The hard X–ray luminosity function.
  2004, in preparation

CONFERENCES PROCEEDINGS

- Comastri A. & Fiore F.
  The density and masses of obscured Black Holes
  2004, in "Baryons in Cosmic Structures – A Meeting in Honour of A. Cavaliere", eds. Kluwer, in press

- Vignali C. (on behalf of the HELLAS2XMM collaboration)
  The HELLAS2XMM 1dF Survey: a window on exotic hard X-ray selected sources
  2004, in "Tenth Marcel Grossman Meeting on General Relativity", Ruffini R., Novello M., & Bergliaffa S.P. eds., in press, astro-ph/0403100

- Fiore F., **Brusa M.**, Cocchia F., Baldi F., Carangelo N., Ciliegi P., Comastri A., La Franca F., Maiolino R., Matt G., Molendi S., Mignoli M., Perola G.C., Severgnini P., Vignali C.
  The HELLAS2XMM 1dF survey: on the nature of high X-ray to optical flux ratio sources
  2004, in "Multi-Wavelength Cosmology", eds. Kluwer

- Comastri A., & the Hellas2XMM team
  Hard X–ray surveys and the X–ray background
  2003, in "XLVII Congresso Nazionale della SAIT", Mem.Sait.Suppl., 3, 179

- Comastri A., **Brusa M.**, Mignoli M. & the Hellas2XMM team
  Unconventional AGN in hard X–ray surveys
  2003, in "X02: X–ray surveys", Astr. Nach., 324, 28

- Matt. G., Braito V., **Brusa M.**, Caccianiga A., La Franca F., Marconi A., Marziani P.
  Obscuration and reprocessing in the cosmic history of Active Galactic Nuclei
  2003, "XLVI Congresso Nazionale della SAIT", Mem. Sait., 74, 367

- **Brusa M.** and the HELLAS2XMM collaboration
  The HELLAS2XMM survey. Broad band observations of serendipitous hard X-ray selected sources
  2002, "Inflows, Outflows and Reprocessing around black holes, V Congresso Nazionale AGN", online publication: http://www.unico.it/ilaria/AGN5/proceedings.html

- Comastri A., **Brusa M.**, Ciliegi P., Mignoli M., Fiore F., Maiolino R., Severgnini P., Baldi A., Molendi S., Vignali C., La Franca F., Matt G., Perola G.C.
  On the nature of X-ray Bright Optically Normal galaxies
  2002, "New Visions of the X-ray Universe in the XMM-Newton and Chandra Era", ESA SP–488

- Comastri A., **Brusa M.**, Ciliegi P., Mignoli M., Vignali C., Severgnini P., Maiolino R., Fiore F., La Franca F., Matt G., Perola G.C., Baldi A., Molendi S.
  X–ray bright optically quiet galaxies: the case of P3
  2001, "Issues in unification of AGNs", A.S.P. Conf. Ser., 258, 199

- Fiore F., Matt G., La Franca F., Perola G.C., **Brusa M.**, Comastri A., Mignoli M., Ciliegi P., Severgnini P., Maiolino R., Baldi A., Molendi S., Vignali C.
  Optical identification of sources from the HELLAS2XMM survey
  2001, "Issues in unification of AGNs", A.S.P. Conf. Ser., 258, 205

- Matt G., Baldi A., **Brusa M.,** Ciliegi P., Comastri A., Fiore F., Giommi P., La Franca F., Maiolino R., Mignoli M., Molendi S., Perola G.C., Severgnini P., Vignali C.
  On the nature of X–ray faint, hard sources
  2001, "Where's the Matter? Tracing dark and bright matter with the new generation of large scale surveys", eds. M. Treyer & L. Tresse,

- Comastri A., Vignali C., **Brusa M.** & the HELLAS and HELLAS2XMM consortia
  The AGN content of Hard X–ray surveys
  2001, "AGN Surveys (IAU Colloquium 184)" A.S.P. Conf. Ser., 284, 235

HARD X–RAY OBSERVATIONS OF EXTREMELY RED OBJECTS

REFEREED JOURNALS

- **Brusa M.**, Comastri A., Daddi E., Cimatti A., Mignoli M., Pozzetti L.
  Extremely Red Objects: an X-ray dichotomy
  2002, ApJ 581, L89

- **Brusa M.**, Comastri A., Daddi E., Pozzetti L., Zamorani G., et al.
  Hard X–ray observations of Extremely Red Objects. I: XMM-Newton data and the link with luminous, X–ray obscured Quasars
  2004, A&A, submitted

CONFERENCES PROCEEDINGS

- **Brusa M.**
  Hard X–ray observations of Extremely Red Objects
  2003, in "X02: X–ray surveys", Astr. Nach., 324, 113

- **Brusa M.**, Comastri, A., Daddi, E., Cimatti, A., & Vignali, C.
  An XMM-Newton survey of Extremely Red Objects
  2002, "X-ray Spectroscopy of AGN with Chandra and XMM-Newton", ed. Th. Boller, S. Komossa, S. Kahn, & H. Kunieda, MPE Report 279, 267

OTHER PUBLICATIONS

- Comastri A., **Brusa M.**, & Civano F.
  A broad iron line at z=1.146
  2004, MNRAS, submitted

- Comastri A., Ranalli P., **Brusa M.**
  Beyond the hard X–ray Background with XEUS
  2003, "XEUS: studying the evolution of the hot Universe", MPE Report 281, 19

Bibliography

Bibliography

[] Afonso, J., Mobasher, B., Chan, B., & Cram, L., 2001, *Ap.J.* **559**, L101

[] Akiyama, M., Ohta, K., Yamada, T., et al. 2000, *Ap.J.* **532**, 700

[] Akiyama, M., Ueda, Y., & Ohta, K., 2002, in "AGN Surveys", IAU Colloquium 184, eds R.F. Green, E.Ye. Khachikian, and D.B. Sanders, *ASP Conf. Ser.* **284**, 245

[] Alexander, D.M., Brandt, W.N., Hornschemeier, A.E., et al. 2001, *A.J.* **122**, 2156

[] Alexander, D.M., Vignali, C., Bauer, F.E., et al. 2002, *A.J.* **123**, 1149

[] Alexander, D.M., Bauer, F.E., Brandt, W.N., et al. 2003, *A.J.* **126**, 539

[] Allen, S.W., Di Matteo, T., & Fabian, A.C., 2000, *M.N.R.A.S.* **311**, 493

[] Antonucci, R.R.J., 1993, *A.R.A.&A.* **31**, 473

[] Baldi, A., Molendi, S., Comastri, A., Fiore, F., Matt, G., & Vignali, C., 2002, *Ap.J.* **564**, 190 (Paper I)

[] Barcons, X., Mateos, S., & Ceballos, M.T., 2000, *M.N.R.A.S.* **316**, L13

[] Barcons, X., Carrera, F.J., Watson, M.G., et al. 2002, *A.&A.* **382**, 522

[] Barkhouse, W.A., & Hall, P.B., 2001, *A.J.* **121**, 2843

[] Barger, A., Cowie, L., Mushotzky, R.F., & Richards, E.A., 2001, *A.J.* **121**, 662

[] Barger, A.J., Cowie, L.L., Bautz, M.W., Brandt, W.N., Garmire, G.P., Hornschemeier, A.E., Ivison, R.J., & Owen, F.N., 2001, *A.J.* **122**, 2177

[] Barger, A., Cowie, L., Brandt, W.N., et al. 2002, *A.J.* **124**, 1839

[] Barger, A.J., Cowie, L.L., Capak, P., et al. 2003, *A.J.* **126**, 632

[] Bauer, F.E., Alexander, D.M., Hornschemeier A.E., Vignali, C., Garmire, G.P., & Schneider, D.P. 2002, *A.J.* **124**, 2351

[] Bauer, F.E., Vignali, C., Alexander, D.M., et al. 2003, *Astron. Nachr.* **324**, 175

[] Bershady, M. A., Lowenthal, J. D., & Koo, D. C., 1998, *Ap.J.* **505**, 50

[] Bertin, E., & Arnouts, S., 1996, *A.&A.S.* **117**, 393

[] Boldt, E., 1987, Phy. Reports, 146, 215

[] Brandt, W.N., Alexander, D.M., Hornschemeier, A.E., et al. 2001a, *A.J.* **122**, 2810

[] Brandt, W.N., Hornschemeier, A.E., Schneider, D.P., Alexander, D.M., Bauer, F.E., Garmire, G.P., & Vignali, C., 2001b, *Ap.J.* **558**, L5

[] Brotherton, M. S., Tran, H. D., Becker, R. H., et al. 2001, *Ap.J.* **450**, 559

[] Brusa, M., Comastri, A., Daddi, E., Cimatti, A., Vignali C., 2002, *MPE Report* **279**, 267

[] Brusa, M., Comastri, A., Daddi, E., Cimatti, A., Mignoli M., & Pozzetti, L., 2002, *Ap.J.* **581**, L89

[] Brusa, M., 2003, *Astron. Nachr.* **324**, 116

[] Brusa, M., Comastri, A., Mignoli, M., et al. 2003, *A.&A.* **409**, 65 (Paper III)

[] Bruzual, A.G., & Charlot, S., 1993, *Ap.J.* **405**, 538

[] Caccianiga, A., Severgnini, P., Braito, V., et al. 2004, *A.&A.* , in press, astro-ph/0312344

[] Cagnoni, I., Della Ceca, R., & Maccacaro, T., 1998, *Ap.J.* **493**, 54

[] Cash, W., 1979, *Ap.J.* **228**, 939

[] Cavaliere, A., & Vittorini, V., 2000, *Ap.J.* **543**, 599

[] Ciliegi, P., Zamorani, G., Hasinger, G., Lehmann, I., Szokoly, G., & Wilson, G., 2003, *A.&A.* **398**, 901

[] Cimatti A., Andreani P., Rottgering H., & Tilanus R., 1998, *Nature* **392**, 895

[] Cimatti, A., Daddi, E., Mignoli, M., et al. 2002a, *A.&A.* **381**, L68

[] Cimatti, A., Mignoli, M., Daddi, E., et al. 2002b, *A.&A.* **392**, 395

[] Cole, S., Norberg, P., Baugh, C.M., et al. 2001, *M.N.R.A.S.* **326**, 255

[] Comastri, A., Setti, G., Zamorani, G., & Hasinger, G., 1995, *A.&A.* **296**, 1

[] Comastri, A., Fiore, F., Vignali, C., Matt, G., Perola, G. C., & La Franca, F., 2001, *M.N.R.A.S.* **327**, 781

[] Comastri, A., 2001, in "X–ray Astronomy '999: Stellar Endpoints, AGNs and the Diffuse X–ray Background", eds. N.E. White, G. Malaguti, and G. G.C. Palumbo, *AIP Conf. Proc.* **599**, 73

[] Comastri, A., Brusa, M., Ciliegi, P., et al. 2002a, in "New Visions of the X–ray Universe in the XMM–Newton and Chandra Era", eds. F. Jansen, ESA SP–488, astro–ph/0203114

[] Comastri, A., Mignoli, M., Ciliegi, P., et al. 2002b, *Ap.J.* **571**, 771 (Paper II)

[] Comastri, A., Brusa, M., Mignoli, M., & the HELLAS2XMM Team, 2003, *Astron. Nachr.* **324**, 28

[] Comastri, A., 2004, in "Supermassive Black Holes in the Distant Universe", Ed. A. J. Barger. Kluwer Academic Publishers, Chapter 8, in press

[] Condon, J.J., Cotton, W.D., Greisen, E.W., Yin, Q.F., Perley, R.A., Taylor, G.B., & Broderick, J.J., 1998, *A.J.* **115**, 1693

[] Costamante, L., Ghisellini, G., Giommi, P., et al. 2001, *A.&A.* **271**, 512

[] Cowie L., Barger A., Bautz, M.W., Brandt, W.N., & Garmire, G.P., 2003, *Ap.J.* **584**, L57

[] Crawford, C. S., Fabian, A. C., Gandhi, P., Wilman, R.J., & Johnstone, R.M., 2001, *M.N.R.A.S.* **324**, 427

[] Cutri, R.M., Nelson, B.O., Kirkpatrick, J.D., Huchra, J.P., & Smith, P.S., 2001, in "The New Era of Wide Field Astronomy", *ASP Conf. Ser.* **232**, 78

[] Cutri, R.M., Nelson, B.O., Francis, P.J., & Smith, P.S. 2002, in "Agn Surveys", *ASP Conf. Ser.* **284**, 127

[] Daddi, E., Cimatti, A., Pozzetti, L., et al. 2000, *A.&A.* **361**, 535

[] Daddi, E., Cimatti, A., Broadhurst, T., et al. 2002, *A.&A.* **384**, L1

[] Dahlem, M., Weaver, K.A., & Heckman, T.M., 1998, *Ap.J.S.S.* **118**, 401

[] Della Ceca, R., Castelli, G., Braito, V., Cagnoni, I., & Maccacaro, T., 1999, *Ap.J.* **524**, 674

[] Dickey, J.M., & Lockman, F.J., 1990, *A.R.A.&A.* **28**, 215

[] Di Matteo, T., Quataert, E., Allen, S.W., Narayan, R., & Fabian, A.C., 2000, *M.N.R.A.S.* **311**, 507

[] Di Matteo, T., Croft, R.A.C., Springel, V., Hernquist, L., 2003, *Ap.J.* **593**, 56

[] Elvis, M., Schreier, E.J., Tonry, J., Davis, M., & Huchra, J.P., 1981, *Ap.J.* **246**, 20

[] Elvis M., Wilkes B.J., McDowell J.C., et al. 1994, *Ap.J.S.S.* **95**, 1

[] Elvis, M., Risaliti, G., & Zamorani, G., 2002, *Ap.J.* **565**, L75

[] Elston R., Rieke G.H., & Rieke M.J., 1988, *Ap.J.* **331**, L77

[] Fabbiano, G., Kim, D.W., & Trinchieri, G., 1992, *Ap.J.S.S.* **80**, 531

[] Fabian, A.C., & Iwasawa, K., 1999, *M.N.R.A.S.* **303**, L34

[] Fabian, A.C., Wilman, R.J., & Crawford, C.S., 2002, *M.N.R.A.S.* **329**, L18

[] Fabian, A.C., 2003, in "Coevolution of Black Holes and Galaxies", Carnegie Observatories Astrophysics Series, Vol. 1, ed. L.C. Ho (Cambridge Univ. Press), astro-ph/0304122

[] Ferrarese, L., & Merrit, D., 2000, *Ap.J.* **539**, L9

[] Ferrarese, L., 2002, in "Hubble Science Legacy Workshop", *ASP Conf. Ser.* **291**, 196

[] Field, G.B., & Perrenod, S.C., 1977, *Ap.J.* **215**, 717

[] Fiore, F., La Franca, F., Giommi, P., Elvis, M., Matt, G., Comastri, A., Molendi, S., & Gioia, I., 1999, *M.N.R.A.S.* **306**, L55

[] Fiore, F., La Franca, F., Giommi, P., et al. 2000, *New Astronomy* **5**, 143

[] Fiore, F., Antonelli, L.A., Ciliegi, P., et al. 2001, in "X–ray Astronomy '999: Stellar Endpoints, AGNs and the Diffuse X–ray Background", ed. N.E. White, G. Malaguti, and G. G.C. Palumbo, *AIP Conf. Proc.* **599**, 111

[] Fiore, F., Giommi, P., Vignali, C., et al. 2001, *M.N.R.A.S.* **327**, 771

[] Fiore, F., Brusa, M., Cocchia, F., et al. 2003, *A.&A.* **409**, 79 (Paper IV)

[] The First XMM-Newton Serendipitous Source Catalogue: 1XMM User Guide to the Catalogue, Release 1.2 15 April 2003, Associated with Catalogue version 1.0.1, Prepared by the XMM-Newton Survey Science Centre Consortium (http://xmmssc-www.star.le.ac.uk/)

[] Fontana, A., Menci, N., D'Odorico, S., Giallongo, E., Poli, F., Cristiani, S., Moorwood, A., & Saracco, P. 1999, *M.N.R.A.S.* **310**, L27

[] Fossati, G., Maraschi, L., Celotti, A., Comastri, A., & Ghisellini, G., 1998, *M.N.R.A.S.* **299**, 433

[] Franceschini, A., Hasinger, G., Miyaji, T., & Malguori, D., 1999, *M.N.R.A.S.* **310**, L5

[] Franceschini, A., Bassani, L., Cappi, M., Granato, G.L., Malaguti, G., Palazzi, E., & Persic, M., 2000, *A.&A.* **353**, 910

[] Franceschini, A., Aussel, H., Cesarsky, C.J., Elbaz, D., & Fadda, D., 2001, *A.&A.* **378**, 1

[] Franceschini, A., Braito, V., & Fadda, D., 2002, *M.N.R.A.S.* **335**, L51

[] Francis, P.J., Hewett, P.C., Foltz, C.B., et al. 1991, *Ap.J.* **373**, 465

[] Freeman, P.E., Kashyap, V., Rosner, R., & Lamb, D., 2002, *Ap.J.S.S.* **138**, 185

[] Gandhi, P., Crawford, C.S., & Fabian, A.C., 2002, *M.N.R.A.S.* **337**, 781

[] Gandhi, P., & Fabian, A.C., 2003, *M.N.R.A.S.* **339**, 1095

[] Gandhi, P., Crawford, C.S., Fabian, A.C., & Johnstone, R.M., 2004, *M.N.R.A.S.* **348**, 529

[] Gebhardt, K., Kormendy, J., Ho, L., et al. 2000, *Ap.J.* **543**, L5

[] Georgakakis, A., Georgantopoulos, I., Vallbe, M., et al. 2004, *M.N.R.A.S.* , in press, astro–ph/0311609

[] George, I.M., Turner, T. J., Yaqoob, T., Netzer, H., Laor, A., Mushotzky, R. F., Nandra, K., & Takahashi, T., 2000, *Ap.J.* **531**, 52

[] Ghisellini, G., Celotti, A., Fossati, G., Maraschi, L., & Comastri, A., 1998, *M.N.R.A.S.* **301**, 451

[] Ghizzardi, S., 2001, EPIC-MCT-TN-011

[] Giacconi, R., Gursky, H., Paolini, F., & Rossi B., 1962, *Phys. Rev. Lett* **9**, 439

[] Giacconi, R., & Zamorani, G., 1987, *Ap.J.* **313**, 20

[] Giacconi, R., Rosati, P., Tozzi, P., et al. 2001, *Ap.J.* **551**, 664

[] Giacconi, R., Zirm, A., Wang, J., et al. 2002, *Ap.J.S.S.* **139**, 369

[] Gilli, R., Salvati, M., & Hasinger, G., 2001, *A.&A.* **366**, 407

[] Gilli, R., 2003, in "New X-ray Results from Clusters of Galaxies and Black Holes", eds. C. Done, E.M. Puchnarewicz, M.J. Ward , in press, astro–ph/0303115

[] Granato, G.L., Silva, L., Monaco, P., Panuzzo, P., Salucci, P., De Zotti, G., & Danese, L., 2001, *M.N.R.A.S.* **324**, 757

[] Green, P.J., Schartel, N., Anderson, S.F., et al. 1995, *Ap.J.* **450**, 51

[] Green, P.J., Silverman, J., Cameron, R., et al. 2004, *Ap.J.S.S.* **150**, 43

[] Gregg, M.D., Lacy, M., White, R.L., et al. 2002, *Ap.J.* **564**, 133

[] Griffiths, R.E., Georgantopoulos, I., Boyle, B.J., Stewart, G.C., Shanks, T., & Della Ceca, R., 1995, *M.N.R.A.S.* **275**, 77

[] Griffiths, R.G, Ptak, A., Feigelson, E.D., Garmire, G.., Townsley, L., Brandt, W. N., Sambruna, R., & Bregman, J.N., 2000, *Science* **290**, 1325

[] Grossan, B.A., 1992, Ph.D. thesis, MIT

[] Gunn, K.F., McHardy, I.M., Seymour, N., et al. 2003, *Astron. Nachr.* **324**, 105

[] Haehnelt, M., 2003, in "Coevolution of Black Holes and Galaxies", Carnegie Observatories Astrophysics Series, Vol. 1, ed. L.C. Ho (Cambridge Univ. Press), astro-ph/0307378

[] Haiman, Z., Ciotti, L., & Ostriker, J., 2004, *Ap.J.* , , submitted, astro–ph/0304129

[] Hall, P.B., & Green, R.F., 1998, *Ap.J.* **507**, 558

[] Hall, P.B., Yee, H.K.C., Lin, H., et al. 2000, *A.J.* **120**, 2220

[] Harrison, F.A., Eckart, M.E., Mao, P.H., Helfand, D.J., & Stern, D., 2003, *Ap.J.* **596**, 944

[] Hartwick F.D.A., & Schade, D., 1990, *A.R.A.&A.* **28**, 437

[] Hasinger, G., Burg, R., Giacconi, R., et al. 1998, *A.&A.* **329**, 482

[] Hasinger, G., Altieri, B., Arnaud, M., et al. 2001, *A.&A.* **365**, L45

[] Hasinger, G., 2003, in "The Emergence of Cosmic Structure", Maryland, eds. Stephen S. Holt and Chris Reynolds, in press, astro-ph/0302574

[] Ho, L.C., 1999, *Ap.J.* **516**, 672

[] Ho, L.C., 2004, "Coevolution of Black Holes and Galaxies", Carnegie Observatories Astrophysics Series, Vol. 1, ed. L. C. Ho (Cambridge: Cambridge Univ. Press), astro–ph/0401526

[] Hornschemeier, A.E., Brandt, W.N., Garmire, G.P., et al. 2000, *Ap.J.* **541**, 49

[] Hornschemeier, A., Brandt, W.N., Garmire, G.P., et al. 2001, *Ap.J.* **554**, 742

[] Hornschemeier, A.E., Brandt, W.N., Alexander, D.M., Bauer, F.E., Garmire, G.P., Schneider, D.P., Bautz, M.W., & Chartas, G., 2002, *Ap.J.* **568**, 82

[] Hutchings, J.B., Maddox, N., Cutri, R.M., & Nelson, B.O., 2003, *A.J.* **126**, 63

[] Jansen, F., Lumb, D., Altieri, B., et al. 2001, *A.&A.* **365**, L1

[] Kaaret, P., Prestwich, A.H., Zezas, A., Murray, S.S., Kim, D.W., Kilgard, R.E., Schlegel, E.M., & Ward, M.J., 2001, *M.N.R.A.S.* **321**, L29

[] Kennicutt, R.C., 1998, *A.R.A.&A.* **36**, 189

[] Kim, D. W., & Elvis, M., 1999, *Ap.J.* **516**, 9

[] Koekemoer, A.M., Alexander, D..M., Bauer, F.,E., et al. 2003, *Ap.J.* **600**, L123

[] Koo, D.C., & Kron R.G., 1988, *Ap.J.* **325**, 92

[] Iwasawa, K., Fabian, A.C., Ettori, S., 2001, *M.N.R.A.S.* **321**, L15

[] La Franca, F., Fiore, F., Vignali, C., Antonelli, A., Comastri, A., Giommi, P., Matt, G., Molendi, S., Perola, G. C., & Pompilio, F., 2002, *Ap.J.* **570**, 100

[] Laor, A., Fiore, F., Elvis, M., Wilkes, B.J., & McDowell, J.C. 1997, *Ap.J.* **477**, 93

[] Lawrence, C.R., Elston, R., Januzzu, B.T., & Turner, E.L., 1995, *A.J.* **110**, 2570

[] Lehmann, I., Hasinger, G., Schmidt, M., et al. 2001, *A.&A.* **371**, 833

[] Lehmann, I., Hasinger, G., Murray, S.S., & Schmidt, M., 2001, in "X-rays at Sharp Focus Chandra Science Symposium", astro–ph/0109172

[] Lilly, S.J., Tresse, L., Hammer, F., Crampton, D., & Le Fevre, O., 1995, *Ap.J.* **455**, 108

[] Lumb, D.H., Guainazzi, M., & Gondoin, P., 2001, *A.&A.* **376**, 387 (L01)

[] Maccacaro, T., Gioia, I.M., Wolter, A., Zamorani, G., & Stocke, J.T., 1988, *Ap.J.* **326**, 680

[] Madau, P., Ghisellini, G., & Fabian, A.C., 1994, *M.N.R.A.S.* **270**, 17

[] Madau, P., 1995, *Ap.J.* **441**, 18

[] Madau, P., Ferguson, H.C.L., Dickinson, M., Giavalisco, M., Steidel, C.C., & Fruchter, A., 1996, *M.N.R.A.S.* **283**, 1388

[] Madau, P., Pozzetti, L., & Dickinson, M., 1998, *Ap.J.* **498**, 106

[] Mainieri, V., Bergeron, J., Hasinger, G., et al. 2002, *A.&A.* **393**, 425

[] Mainieri, V., 2004, "A new view on the nature and evolution of Active Galactic Nuclei with Chandra and XMM–Newton", Ph.D. thesis, Università Roma Tre and ESO

[] Maiolino, R., Salvati, M., Antonelli, L.A., et al. 2000, *A.&A.* **335**, L47

[] Maiolino, R., Marconi, A., Salvati, M., et al. 2001, *A.&A.* **365**, 28

[] Maiolino, R., Marconi, A., & Oliva, T., 2001, *A.&A.* **365**, 37

[] Maiolino, R., Comastri, A., Gilli, R., et al. 2003, *M.N.R.A.S.* **344**, L59

[] Manners, J., Johnson, O., Almaini, O., et al. 2003, *M.N.R.A.S.* **343**, 293

[] Marconi, A., Risaliti, G., Gilli, R., Hunt, L.K., Maiolino, R., & Salvati, M., 2004, *M.N.R.A.S.* , , in press, astro–ph/0311619

[] Marshall, F.E., Boldt, E.A., Holt, S.S., et al. 1980, *M.N.R.A.S.* **317**, 265

[] Mather, J.C., Cheng, E.S., Eplee, R.E., et al. 1990, *Ap.J.* **354**, L37

[] Matsumoto, H., Koyama, K., Awaki, H., Tsuru, T., Loewenstein, M., & Matsushita, K., 1997, *Ap.J.* **482**, 133

[] Matt, G., 2001, in "Issues in unification of AGNs", eds. A. Marconi, R. Maiolino, & N. Nagar, *ASP Conf. Ser.* **258**, 3

[] Menci, N., Fiore, F., Perola, G.C., & Cavaliere, 2004, *Ap.J.* , , in press, astro–ph/0401261

[] Mignoli, M., Zamorani, G., & Marano, B., 2002, in "Lighthouses of the Universe", MPA/ESO, p. 590

[] Mignoli, M., Pozzetti, L., Comastri, A., et al. 2003, *A.&A.* **418**, 827

[] Miyaji, T., Hasinger, G., & Schmidt, M., 2000, *A.&A.* **353**, 25

[] Mineo, T., Fiore, F., Laor, A., Costantini, E., Brandt, W. N., Comastri, A., Della Ceca, R., Elvis, M., Maccacaro, T., & Molendi, S., 2000, *A.&A.* **359**, 471

[] Mohan, N.R., Cimatti, A, Röttgering, H.J.A., Andreani, P., Severgnini, P., Tilanus, R.P.J., Carilli, C.L., & Stanford, S.A., 2002, *A.&A.* **383**, 440

[] Monaco, P., Salucci, P., Danese, L., 2000, *M.N.R.A.S.* **311**, 279

[] Monet, D., Bird A., Canzian, B., et al. 1998, The PMM USNO–A2.0 Catalog, (Washington D.C: U.S. Naval Observatory)

[] Moorwood, A.F.M., Cuby, J.G., Ballester, P., et al. 1999, *The Messenger* **95**, 1

[] Moran, E.C., Filippenko, A. V., & Chornock, R., 2002, *Ap.J.* **579**, L71

[] Moretti, A., Campana, S., Lazzati, D., & Tagliaferri, G., 2003, *Ap.J.* **588**, 696

[] Mushotzky, R.F., 1984, *Adv. Sp. Res.* **3**, 157

[] Mushotzky, R.F., Cowie, L.L., Barger, A.J., & Arnaud, K.A., 2000, *Nature* **404**, 459

[] Nandra, K., George, I.M., Mushotzky, R.F., Turner, T.J., & Yaqoob, T., 1997, *Ap.J.* **476**, 70

[] Nandra, K., Mushotzky, R.F., Arnaud, K., Steidel, C.C., Adelberger, K.L., Gardner, J.P., Teplitz, H.I., & Windhorst, R.A., 2002, *Ap.J.* **576**, 625

[] Nandra, K., Georgantopoulos, I., Brotherton, M., & Papadakis, I.E., 2004, *M.N.R.A.S.* **3471**, L41

[] Norman, C., Hasinger, G., Giacconi, R., et al. 2002, *Ap.J.* **571**, 218

[] Ogasaka, Y., Inoue, H., Brandt, W.N., Fabian, A.C., Kii, T., Nakagawa, T., Fujimoto, R., & Otani, C., 1997, *P.A.S.J.* **49**, 179

[] Oke, J.B., 1990, *A.J.* **99**, 1621

[] Page, M.J., McHardy, I.M., Gunn, K.F., et al. 2003, *Astron. Nachr.* **324**, 101

[] Panessa, F., & Bassani, L., 2002, *A.&A.* **394**, 435

[] Pappa, A., Georgantopoulos, I., Stewart, G.C., & Zezas, A.L., 2001, *M.N.R.A.S.* **326**, 995

[] Patat, F., 1999, Efosc2 Users' Manual, LSO–MAN–ESO–36100–0004

[] Pellegrini, S., 1999, *A.&A.* **351**, 487

[] Perola, G.C., Puccetti, S., Fiore, F., et al. 2004, submitted to *A.&A.* , (Paper VI)

[] Piccinotti, G., Mushotzky, R.F., Boldt, E.A., et al. 1982 *Ap.J.* **253**, 485

[] Piconcelli, E., Cappi, M., Bassani, L., et al. 2002, *A.&A.* **394**, 835

[] Piconcelli, E., Cappi, M., Bassani, L., et al. 2003, *A.&A.* **412**, 689

[] Pierre, M., Lidman, C., Hunstead, R., et al. 2001, *A.&A.* **372**, L45

[] Pozzetti, L., Madau, P., Zamorani, G., Ferguson, H.C., & Bruzual, A.G., 1998, *M.N.R.A.S.* **298**, 1133

[] Pozzetti, L., & Madau, P., 2000, in "The Extragalactic Infrared Background and its Cosmological Implications", IAU Symposium 204, p. 71, eds. M. Harwitt and M. G. Hauser, astro–ph/0011359

[] Pozzetti, L., Cimatti, A., Zamorani, G., et al. 2003, *A.&A.* **402**, 837

[] Ptak, A., Serlemitsos, P., Yaqoob, T., & Mushotzky, R.F., 1999, *Ap.J.S.S.* **120**, 179

[] Quataert, E., & Narayan, R., 1999, *Ap.J.* **520**, 298

[] Ranalli, P., Comastri, A., & Setti, G.C., 2003, *A.&A.* **399**, 39

[] Roche, N.D., Almaini, O., Dunlop, J., et al. 2002, *M.N.R.A.S.* **337**, 1282

[] Roche, N., Dunlop, J., & Almaini, O., 2003, *M.N.R.A.S.* **346**, 803

[] Rosati, P., Tozzi, P., Giacconi, R., et al. 2002, *Ap.J.* **566**, 667

[] Salpeter, E.E., 1955, *Ap.J.* **121**, 161

[] Saracco, P., Giallongo, E., Cristiani, S., et al. 2001, *A.&A.* **375**, 1

[] Schmidt, M., 1968, *Ap.J.* **151**, 393

[] Schmidt, M., & Green, R.F., 1986, *Ap.J.* **305**, 68

[] Schmidt, M., Hasinger, G., Gunn, J., Schneider, D., Burg, R., Giacconi, R., Lehmann, I., MacKenty, J., Trumper, J., & Zamorani, G., 1998, *A.&A.* **329**, 495

[] Setti, G., & Woltjer, L., 1989, *A.&A.* **224**, L21

[] Severgnini, P., Caccianiga, A., Braito, V., et al. 2003, *A.&A.* **406**, 483

[] Severgnini, P., Della Ceca, R., Braito, V., et al. 2003, in "Multiwavelength Mapping of Galaxy Formation and Evolution", astro–ph/0312098

[] Shafer, R.A., & Fabian, A.C., 1983, *IAUS* **104**, 333

[] Smail, I., Owen, F.N., Morrison, G.E., et al. 2002, *Ap.J.* **581**, 844

[] Snowden, S.L., 2002, in "New Visions of the X-ray Universe in the XMM–*Newton* and *Chandra* era", in press, astro–ph/0203311

[] Soltan, A., 1982, *M.N.R.A.S.* **200**, 115

[] Spergel, D.N., Verde, L., Peiris, H.V., et al. 2003, *Ap.J.S.S.* **148**, 175

[] Stern, D., Moran, E.C., Coil, A.L., et al. 2002, *Ap.J.* **568**, 71

[] Stevens, J.A., Page, M.J., Ivison, R.J., et al. 2003, *M.N.R.A.S.* **342**, 249

[] Sutherland, W., & Saunders, W., 1992, *M.N.R.A.S.* **259**, 413

[] Szokoly, G.P., Bergeron, J., Hasinger, G., et al. 2004, *Ap.J.S.S.* , , submitted, astro–ph/0312324

[] Tananbaum, H., Avni, Y., Branduardi, G., et al. 1979, *Ap.J.* **234**, L9

[] Tanaka, Y., Nandra, K., Fabian, A.C., et al. 1995, *Nature* **375**, 659

[] Thompson, D., Beckwith, S.V.W., Fockenbrock, R., et al. 1999, *Ap.J.* **523**, 100

[] Tozzi, P., Rosati, P., Nonino, M., et al. 2001a, *Ap.J.* **562**, 42

[] Tozzi, P., & the CDFS Team, 2001b, in "Where's the Matter?", Marseille, France, 25-29 June 2001, eds. L. Tresse and M. Treyer, astro–ph/0111036

[] Turner, T.J., & Pounds, K.A., 1989, *M.N.R.A.S.* **240**, 833

[] Turner, T.J., Perola, G.C., Fiore, F., et al. 2000, *Ap.J.* **531**, 245

[] Ueda, Y., Takahashi, T., Ishisaki, Y., & Ohashi, T., 1999, *Ap.J.* **524**, L11

[] Ueda, Y., Akiyama, M., Ohta, K., & Miyaji, T., 2003, *Ap.J.* **598**, 886

[] Ulrich, M.H., 2000, *A.&A. Rev.* **10**, 135

[] Vignali, C., Mignoli, M., Comastri, A., Maiolino, R., & Fiore, F., 2000, *M.N.R.A.S.* **314**, L11

[] Vignali, C., Comastri, A., Fiore, F., & La Franca, F., 2001, *A.&A.* **370**, 900

[] Vignali, C., 2001, "The High Energy Large Area Survey (HELLAS): probing the multiwavelength properties of the sources making the hard X–ray Background", Ph.D. thesis, Università di Bologna

[] Vignali, C., Alexander, D.M., Bauer, F.E., Brandt, W.N., Hornschemeier, A.E., Garmire, G.P., & Schneider, D.P., 2002, in "5th Italian AGN Meeting: Inflows, Outflows and Reprocessing around black holes", astro–ph/0209415

[] Vignali, C., Brandt, W.N., & Schneider, D.P., *A.J.* **125**, 433

[] Vignati, P., Molendi, S., Matt, G., et al. 1999, *A.&A.* **349**, L57

[] Yu, Q., & Tremaine, S., 2002, *M.N.R.A.S.* **335**, 965

[] Watanabe, C., Ohta, K., Akiyama, M., & Ueda, Y., 2004, *Ap.J.* , in press, astro–ph/0402520

[] Webster, R.L., Francis, P.J., Peterson, B.A., et al. 1995, *Nature* **375**, 469

[] Weingartner, J., & Murray, N., 2002, *Ap.J.* **580**, 88

[] Wilkes, B.J., Schmidt, G.D., Cutri, R.M., et al. 2002, *Ap.J.* **564**, L65

[] Willott, C., Rawlings, S., Jarvis, M.J., Blundell, K.M., 2003, *M.N.R.A.S.* **339**, 397

[] Wright, E.L., Mather, J.C., Fixsen, D.J., et al. 1994, *Ap.J.* **420**, 450

[] Yan, L., Thompson, D., & Soifer, B.T., 2004, *A.J.* **127**, 1274

[] Zamorani, G., Mignoli, M., Hasinger, G., et al. 1999, *A.&A.* **346**, 731

[] Zombeck, M.V., Handbook of Space Astronomy and Astrophysics, Cambridge University Press, 1990